LUMA-GIS Thesis nr 32

COMBINING HYPERSPECTRAL UAV AND MULTISPECTRAL FORMOSAT-2 IMAGERY FOR PRECISION AGRICULTURE APPLICATIONS

Caroline Gevaert

2014

Department of
Physical Geography and Ecosystem Science
Centre for Geographical Information Systems
Lund University
Sölvegatan 12
S-223 62 Lund

Caroline Gevaert (2014). Combining Hyperspectral UAV and Multispectral Formosat-2 Imagery for Precision Agriculture Applications.
Master degree thesis, 30/ credits in Master in Geographical Information Sciences
Department of Physical Geography and Ecosystems Science, Lund University

Combining Hyperspectral UAV and Multispectral Formosat-2 Imagery for Precision Agriculture Applications

Caroline Gevaert

Master thesis, 30 credits, in Geographical Information

Sciences

Supervisor:

Jing Tang

Department of Physical Geography and Ecosystem Sciences

Lund University

Abstract

In the context of threatened global food security, precision agriculture provides a solution which can maximize yield to meet the increased demands of food while minimizing both economic and environmental costs of food production. Detailed information regarding crop status is crucial for precision agriculture. Remote sensing provides an efficient way to obtain crop biophysical status information, such as canopy nitrogen content, leaf coverage, and plant biomass. However, individual sensors do not normally meet both spatial and temporal requirements for precision agriculture. Therefore, this study investigates different fusion methods which can be used to combine imagery from various sensors to overcome the limitations of each individual sensor. The imagery utilized in the current study consists of multispectral satellite (Formosat-2) and hyperspectral Unmanned Aerial Vehicle (UAV) imagery of a potato field in the Netherlands.

The imagery from both platforms was combined in two ways. Firstly, data fusion methods brought the spatial resolution of the Formosat-2 imagery (8 m) down to the spatial resolution of the UAV imagery (1 m). Two data fusion methods were applied: an unmixing-based algorithm and the Spatial and Temporal Adaptive Reflectance Fusion Model (STARFM). The unmixing-based method produced vegetation indices which were highly correlated to the measured LAI (r_s= 0.866) and canopy chlorophyll values (r_s=0.884), whereas the STARFM showed lower correlations (r_s=0.477 and r_s=0.431, respectively). Secondly, a Spectral-Temporal Reflectance Surface (STRS) was constructed to interpolate daily 101-band reflectance spectra using both sources of imagery. The STRS were interpolated using a new method, which utilizes Bayesian theory to obtain realistic spectra and accounts for sensor uncertainties. The resulting surface obtained a high correlation to LAI (r_s=0.858) and canopy chlorophyll (r_s=0.788) measurements at field level.

The usefulness of these multi-sensor datasets was further analyzed regarding their ability to map crop status variability and predict yield. The results showed the capability of the multi-sensor datasets to characterize significant differences of crop status due to differing nitrogen fertilization regimes from June to August. Meanwhile, the yield prediction models based purely on the vegetation indices extracted from the unmixing-based fusion dataset explained 52.7% of the yield variation, which is lower than that explained by the STRS (72.9%). Around 75.3% of the yield can be explained by a regression model using direct field LAI and chlorophyll measurements.

The results of the current study indicate that the limitations of each individual sensor can be largely surpassed by combining multiple sources of imagery. This can be very beneficial for precision agriculture management decisions, which require require reliable and high-quality information. Further research could focus on the integration of data fusion and STRS techniques, and the inclusion of imagery from additional sensors.

Samenvatting

In een wereld waar toekomstige voedselzekerheid bedreigd wordt, biedt precisielandbouw een oplossing die de oogst kan maximaliseren terwijl de economische en ecologische kosten van voedselproductie beperkt worden. Om dit te kunnen doen is gedetailleerde informatie over de staat van het gewas nodig. Remote sensing is een manier om biofysische informatie, waaronder stikstof gehaltes en biomassa, te verkrijgen. De informatie van een individuele sensor is echter vaak niet genoeg om aan de hoge eisen betreft ruimtelijke en temporele resolutie te voldoen. Deze studie combineert daarom de informatie afkomstig van verschillende sensoren, namelijk multispectrale satelliet beelden (Formosat-2) en hyperspectral Unmanned Aerial Vehicle (UAV) beelden van een aardappel veld, in een poging om aan de hoge informatie eisen van precisielandbouw te voldoen.

Ten eerste werd gebruik gemaakt van datafusie om de acht Formosat-2 beelden met een resolutie van 8 m te combineren met de vier UAV beelden met een resolutie van 1 m. De resulterende dataset bestaat uit acht beelden met een resolutie van 1 m. Twee methodes werden toegepast, de zogenaamde STARFM methode en een unmixing-based methode. De unmixing-based methode produceerde beelden met een hoge correlatie op de Leaf Area Index (LAI) (r_s= 0.866) en chlorofyl gehalte (r_s=0.884) gemeten op veldnieveau. De STARFM methode presteerde slechter, met correlaties van respectievelijk r_s=0.477 en r_s=0.431. Ten tweede werden Spectral-Temporal Reflectance Surfaces (STRSs) ontwikkeld die een dagelijks spectrum weergeven met 101 spectrale banden. Om dit te doen is een nieuwe STRS methode gebaseerd op de Bayesiaanse theorie ontwikkeld. Deze produceert realistische spectra met een overeenkomstige onzekerheid. Deze STRSs vertoonden hoge correlaties met de LAI (r_s=0.858) en het chlorofyl gehalte (r_s=0.788) gemeten op veldnieveau.

De bruikbaarheid van deze twee soorten datasets werd geanalyseerd door middel van de berekening van een aantal vegetatie-indexen. De resultaten tonen dat de multi-sensor datasets capabel zijn om significante verschillen in de groei van gewassen vast te stellen tijdens het groeiseizoen zelf. Bovendien werden regressiemodellen toegepast om de bruikbaarheid van de datasets voor oogst voorspellingen. De unmixing-based datafusie verklaarde 52.7% van de variatie in oogst, terwijl de STRS 72.9% van de variabiliteit verklaarden.

De resultaten van het huidige onderzoek tonen aan dat de beperkingen van een individuele sensor grotendeels overtroffen kunnen worden door het gebruik van meerdere sensoren. Het combineren van verschillende sensoren, of het nu Formosat-2 en UAV beelden zijn of andere ruimtelijke informatiebronnen, kan de hoge informatie eisen van de precisielandbouw tegemoet komen.

Acknowledgements

The current research would not have been possible without the help of many people. Firstly, Dr. Lammert Kooistra from the WU-GRS, who served as an external supervisor for this thesis. Thank you for providing me with the opportunity to work on this subject and for all your helpful comments and guidance. Many thanks also to Dr. Juha Suomalainen from the WU-GRS who developed the UAV system and processed the imagery, and to Dr. Javier García-Haro from the University of Valencia who played a significant role in developing the unmixing-based fusion method used in this paper.

I would also like to thank my supervisor at Lund University, Jing Tang for her help in the development of this thesis. And to all the team behind the LUMA-GIS program, who I have not (yet) been able to thank face-to-face, but who have put together a wonderful Master's program. This provides a unique opportunity for many students throughout the world, and I personally am very happy that I was able to participate.

The help of Dr. Cheng-Chien Liu of National ChengKung University is acknowledged for kindly providing the Formosat-2 spectral response data.

Finally, I would also like to take this opportunity to thank my family. For their patience and support.

Table of Contents

1 Introduction 1
2 Objectives 4
3 Background 5
3.1 Data fusion 5
3.2 Spectral-Temporal Reflectance Surfaces (STRS) 5
3.3 Vegetation indices 6
3.4 Yield prediction 7
4 Data and Methodology 9
4.1 Study area 9
4.2 Data 11
4.2.1 Formosat-2 imagery 11
4.2.2 UAV imagery 12
4.2.3 Field data 12
4.3 Methods 13
4.3.1 Data pre-processing 14
4.3.2 Data Fusion 16
4.3.3 STRS 16
4.3.4 Vegetation indices 20
4.3.5 Statistical analyses 20
5 Results 22
5.1 Data pre-processing 22
5.1.1 Formosat-2 imagery 22
5.1.2 Yield interpolation 22
5.2 Data fusion 23
5.3 STRS 26
5.4 Vegetation indices 28
5.5 Statistical analysis 29
5.5.1 Variation detection during the growing season 29
5.5.2 Yield prediction 31
6 Discussion 35
6.1 Combination of multi-sensor imagery 35
6.2 Vegetation indices 36
6.3 Fused datasets for in-season crop status analysis and yield prediction 36
6.4 Yield prediction 37
7 Conclusions 38
8 References 39
9 Series from Lund University 44
Appendix 1: Atmospheric correction of Formosat-2 imagery 1
Appendix 2: Data fusion parameter optimization 1
Appendix 3: Vegetation indices 1
Appendix 4: WHISPERS 2014 Submission 1

1 Introduction

Global food security is threatened by increased demands from a growing global population, increased competition for land, and the need for sustainable production with lower environmental externalities (Godfray et al. 2010). Precision agriculture is often flagged as a key "sustainable intensification" method, as it aims to maximize the agricultural production in a sustainable manner (The Royal Society 2009). One of the key steps is to quantify both spatial and temporal variations of crop conditions and apply various management strategies within a field according to these differences (Gebbers and Adamchuk 2010). By applying the exact amount of input resources where and when it is needed, the yield can be maximized while reducing the application of fertilizer and pesticides - which is economically beneficial for the farmer and environmentally beneficial for the general population (Gebbers and Adamchuk 2010; Clay and Shanahan 2011).

Remote sensing is capable of identifying variation in biophysical parameters such as canopy nitrogen content and plant biomass (Clevers and Kooistra 2012). It plays a key role in agricultural monitoring (Jones and Vaughan 2010), especially in the identification of nitrogen stress (Mcmurtrey et al. 2003; Goffart et al. 2008; Diacono et al. 2012). It is recognized as one of the key methods to quantify both temporal and spatial variations of crop conditions which are essential for the application of precision agriculture (Gebbers and Adamchuk 2010). Yield-prediction models are often based on the assumption that yield production is influenced by measureable biophysical parameters such as LAI and chlorophyll, variations in which can be identified in remotely-sensed images through the use of vegetation indices (Bala and Islam 2009; Shillito et al. 2009; Gontia and Tiwari 2011; Neale and Sivarajan 2011; Rembold et al. 2013; Ramírez et al. 2014). Yield prediction based on remotely sensed biophysical parameters is more challenging in the current situation, as potato tubers are grown below-ground (Ramírez et al. 2014).

Optical remote sensing imagery can be divided into multispectral satellite imagery and hyperspectral imagery. Multispectral imagery consists of a limited number of broad spectral bands (Christophe et al. 2005), and contains general information regarding vegetation structure and crop greenness (Zarco-Tejada et al. 2005). Hyperspectral imagery contains more than 100 spectral bands, which are also much narrower than multispectral imagery and provide a continuous reflectance spectrum (Christophe et al. 2005). Such imagery is capable of providing more detailed information and specific crop physiological parameters, such as chlorophyll, carotenoids, and water conditions (Zarco-Tejada et al. 2005). Multispectral imagery has been available longer and is more widespread, however the increased precision of hyperspectral imagery for vegetation monitoring is increasingly being recognized in the international community (Haboudane et al. 2004).

Many studies describe the use of multispectral satellite imagery for precision agriculture applications (Plant 2001; Cohen et al. 2010; Lee et al. 2010; Lunetta et al. 2010; Ge et al. 2011; Diacono et al. 2012). However, factors such as inadequate spatial or temporal resolution (Merlin et al. 2010) and cloud cover (Mulla 2013) have limited the effectiveness of utilizing such satellite imagery (Dorigo et al. 2007). Alternatively, Unmanned Aerial Vehicles (UAV) have been proposed for precision agriculture applications (Berni et al. 2009; Kooistra et al. 2012; Zhang and Kovacs 2012; Kooistra et al. 2013) as they can provide imagery with a higher spatial resolution and more flexible acquisition times compared to satellite imagery (Zhang and Kovacs 2012). Furthermore, UAVs fly under the clouds allowing them to obtain imagery on cloudy days, which is a great benefit in areas with frequent cloud cover, such as the Netherlands[1]. However, operational requirements may inhibit monitoring of large areas and the frequency of flights (Zhang and Kovacs 2012). The current research investigates the integration of reflectance information from multispectral satellite imagery and hyperspectral UAV imagery in two ways: (1) *data fusion* to compare sensors of differing spatial resolution and (2) the creation of S*pectral-Temporal Reflectance Surfaces (STRS)* to integrate the spectral and temporal resolutions of multiple sensors.

A potato field near Reusel, the Netherlands was selected for the study area (Kooistra et al. 2013). Four dates of UAV images were obtained over the study area during the growing season of 2013. Formosat-2 satellite imagery is available over the zone at eight dates in the same growing season. Moreover, an experimental set-up divided the field into four zones which were treated with four different nitrogen application rates at the beginning of the growing season. During the entire growing season, weekly field measurements of leaf chlorophyll, Leaf Area Index (LAI), and spectral reflectance were obtained for a number of experimental plots. This creates a unique experimental set-up to analyze synergistic methods to combine UAV and Formosat-2 imagery, and further enable us to evaluate the results using field data.

Data fusion is a possible method to combine imagery from sensors with differing spatial resolutions (Pohl and Van Genderen 1998). Recently, many researchers have investigated the application of data fusion between medium spatial-resolution imagery such as MODIS (Gao et al. 2006) and MERIS (Zurita-Milla et al. 2008; Amorós-López et al. 2013) and high spatial-resolution datasets such as Landsat to obtain a fused image dataset with a daily temporal resolution and a spatial resolution of 30 m. Two prevalent data fusion methods are the Spatial and Temporal Adaptive Reflectance Fusion Model (STARFM) (Gao et al. 2006) and unmixing-based data fusion (Zurita-Milla et al. 2008; Amorós-López et al. 2013).

STARFM is the most widely-used data fusion algorithm for Landsat and MODIS imagery (Emelyanova et al. 2013). It is one of the few data fusion methods which obtains surface reflectance calibrated to the high-resolution image (Singh 2011). The method is particularly useful for detecting gradual changes over large land areas, such as phenology studies (Gao et al. 2006; Hilker et al. 2009). Disadvantages of the STARFM method include the requirement of a base pair of high- and medium-resolution images for reference, dependency on the availability of homogenous medium-resolution pixels (Zhu et al. 2010), and sensitivity to temporal variation of land cover (Gevaert and García-Haro 2014).

On the other hand, unmixing-based data fusion methods do not require corresponding spectral bands. It therefore allows for the downscaling of additional spectral bands of the medium-resolution sensor (Zurita-Milla et al. 2011; Amorós-López et al. 2013) and do not require a base image pair. The unmixing-based method is less sensitive to temporal variations, and provides more stable errors (Gevaert and García-Haro 2014). An important difference with the STARFM method is that the unmixing-based method retains the spectral information of the medium-resolution image, and thus does not provide reflectance calibrated to

[1] During the growing season of 2013, the meteorological station nearest to the study area (Eindhoven) reported 79.1% of the days were at least half-clouded, and 57.8% of the days were heavily clouded (KNMI 2014).

the high-resolution image (Zurita-Milla et al. 2011; Amorós-López et al. 2013). A more detailed analysis comparing various data fusion methods can be found in Gevaert (2013).

The current thesis hypothesizes that these two data fusion methods are also suitable for combining multispectral Formosat-2 satellite imagery with hyperspectral UAV imagery. The fused dataset could benefit from the spatial resolution of the UAV imagery (1 m), and the added temporal frequency of the Formosat-2 imagery.

However the fused datasets obtained through both methods contain only four spectral bands, and do not benefit from the additional spectral information contained in the UAV imagery. STRS are 4-dimensional image datasets (row, line, wavelength, time) which illustrate how the spectrum of a certain pixel changes over time. Previous studies have applied STRS to Landsat-5/TM and Landsat-7/ETM+ imagery to characterize sugarcane harvests in Brazil (Mello et al. 2013), and to MERIS and MODIS imagery to create a cloud-free image time series (Villa et al. 2013). A STRS is formed by interpolating the reflectance of each pixel along the wavelength and temporal dimensions. Mello et al. (2013) utilized the Polynomial Trend Surface (PTS) and Collocation Surface (CS) methods to interpolate the spectral and temporal dimensions directly. Villa et al. (2013) first interpolated MERIS and MODIS spectra along the wavelength dimension using a spline interpolation, and then interpolated along the temporal dimension separately.

However, these STRS implementation methods have a number of limitations. Firstly, they do not account for the physical characteristics of reflectance spectra. Therefore, the interpolated spectra may be unrealistic, such as a missing red-edge for vegetation spectra (Figure 7 in Mello et al. 2013; Figure 1 in Villa et al. 2013). Secondly, all imagery observations are weighted equally – the uncertainty of each image is not taken into account. This thesis utilizes a new methodology to obtain STRS based on Bayesian theory which could these limitations (Mello et al. 2013; Villa et al. 2013).

In sum, the purpose of this study is to investigate methods to combine multiple sources of imagery to obtain a product which provides reliable information regarding crop status for precision agriculture applications. Data fusion methods are applied to combine the spatial and spectral information from satellite and UAV data. STRS methods are applied to combine the spectral and temporal information from the multispectral and hyperspectral imagery. Finally, the ability of these methods to document variations in crop biophysical parameters during the growing season and to explain yield variability are analyzed through statistical methods.

2 Objectives

The objective of the current research is to develop methods to combine the high temporal resolution of multispectral Formosat-2 imagery and the high spatial and spectral resolution of hyperspectral UAV imagery for precision agriculture applications.

This objective was achieved by completing the following steps:

- Exploring a systematic scheme of combining multispectral and hyperspectral imagery for precision agriculture.
- Applying current data fusion methods for MODIS/MERIS and Landsat fusion to UAV and Formosat-2 imagery.
- Exploring the use of STRS to take advantage of the hyperspectral information of the UAV imagery, and to provide daily reflectance data at plot level.
- Analyzing the influence of differing initial fertilization regimes on crop status variability during the growing season, as captured by fused datasets.
- Analyzing the influence of differing initial fertilization regimes on potato yield, and the ability of crop status parameters obtained from fused datasets during the growing season to explain this yield variability.

3 Background

3.1 Data fusion

By applying cross-sensor data fusion, two or more datasets are combined to create a result which exceeds the physical limitations of the individual input datasets (Lunetta et al. 1998). Previous studies have applied cross-sensor data fusion between medium- and high-resolution imagery for applications such as phenology analysis (Hwang et al. 2011; Bhandari et al. 2012; Walker et al. 2012; Feng et al. 2013), forest disturbance mapping (Hilker et al. 2009; Arai et al. 2011; Xin et al. 2013), the estimation of biophysical parameters (Anderson et al. 2011; Singh 2011; Gao et al. 2012), and public health (Liu and Weng 2012). In this study, two data fusion methods are applied. These were chosen because a literature study suggested that these two methods represent two major groups of data fusion methods applied to combine optical satellite imagery (Emelyanova et al. 2012; Villa et al. 2013).

The first method is the Spatial and Temporal Adaptive Reflectance Fusion Model (STARFM), which was designed for fusing Landsat and MODIS imagery (Gao et al. 2006) to create a fused product with a spatial resolution of 30 m obtained from the Landsat dataset and a daily temporal resolution obtained from the MODIS imagery. It is one of the few data fusion methods which result in synthetic calibrated surface reflectance (Singh 2011). This method is particularly useful for detecting gradual changes over large land areas, such as phenology studies (Gao et al. 2006; Hilker et al. 2009). However, the disadvantages of this method are: the quality of the fused product is highly dependent on the availability of input imagery, and both sensors must have corresponding spectral bands (Emelyanova et al. 2013; Gevaert 2013).

A second set of data fusion algorithms are based on unmixing techniques (Zurita-Milla et al. 2008; Amorós-López et al. 2013). These methods rely on the linear spectral mixture model to extract endmembers and abundances on a sub-pixel scale (Bioucas-Dias et al. 2012). In unmixing-based data fusion, the number of endmembers and their relative abundances within a medium-resolution pixel are obtained from the high-resolution dataset, while the spectral signature of the endmembers is unmixed from the medium-resolution dataset. This method has previously been applied to Landsat and MERIS data (Zurita-Milla et al. 2009; Zurita-Milla et al. 2011; Amorós-López et al. 2013). The main advantage of unmixing-based method is that, unlike the STARFM-based methods, it does not require the high-resolution and medium-resolution data to have corresponding spectral bands (Amorós-López et al. 2013) which allows for two additional possibilities. Firstly, unmixing-based data fusion can be used to downscale extra spectral bands and/or biophysical parameters to increase the spectral resolution of the high-resolution data sets. Secondly, the input high-resolution data does not necessarily have to be a satellite image, but auxiliary datasets such land cover can alternatively be used to control the grouping of spectrally similar pixels into clusters (Zurita-Milla et al. 2011). In the current study, both methods are applied to the UAV and Formosat-2 imagery to determine which is more applicable in the study area.

3.2 Spectral-Temporal Reflectance Surfaces (STRS)

The purpose of STRS is to combine imagery obtained from multiple sensors along the spectral and temporal dimensions to obtain images with a spectral and temporal resolution defined by the user. STRS provide predicted daily surface reflectance during a defined period rather than restricting the user to the dates for which images are available. It also allows for the combination of spectral information from different sensors through the use of interpolation techniques.

The STRS methodology presented here is inspired by previous works (Mello et al. 2013; Villa et al. 2013). These previous works are limited because there is no restriction that the resulting spectra be representative of the physical surface reflectance characteristics. For example, the spline interpolation used in Villa et al. (2013) of the Formosat-2 spectra between the red and near infrared (NIR) spectra would create a smooth spectrum, but lose the characteristic red-edge of vegetation (Gilabert et al. 2010). Another limitation of the previously documented methodologies is that all observations are weighted equally which is unrealistic as the surface reflectance obtained from some data sources (such as UAV imagery) are more reliable than others (such as Formosat-2).

Therefore, an improved methodology is strongly needed and in this study, a STRS based on Bayesian theory Bayesian theory is proposed. The inclusion of Bayesian theory allows the user to define sensor uncertainties (Murphy 2012), and puts model uncertainties into a probabilistic framework (Fasbender et al. 2008).

3.3 Vegetation indices

The spectral signature of green vegetation is determined by leaf pigments such as chlorophyll in the visible spectrum, cell structure in the near infrared (NIR) spectrum, and leaf water content in the shortwave infrared (SWIR) region (Gilabert et al. 2010). The reflectance in the visible spectrum can be related to nitrogen concentrations and chlorophyll, whereas the NIR region is related to biophysical parameters such as biomass and LAI (Clevers and Kooistra 2012). The sharp increase in reflectance around 700 nm is characteristic of live green vegetation, and is known as the red-edge (Figure 1). Vegetation indices take advantage of such characteristics, calculating ratios between spectral bands in different regions to obtain an index which can be related to certain biophysical properties (Gilabert et al. 2010).

Vegetation indices are sensitive to variations in plant biophysical parameters while remaining robust to external factors such as atmosphere, solar geometry, and soil background (Gilabert et al. 2010). However, each vegetation index is a simplification of original surface reflectance, and therefore portray only a part of the information contained within the original bands (Govaerts et al. 1999). Furthermore, many vegetation indices relating red and NIR spectral bands display saturation at higher vegetation densities (Myneni et al. 1995) and are dependent on canopy structure and land cover (Gilabert et al. 2010).

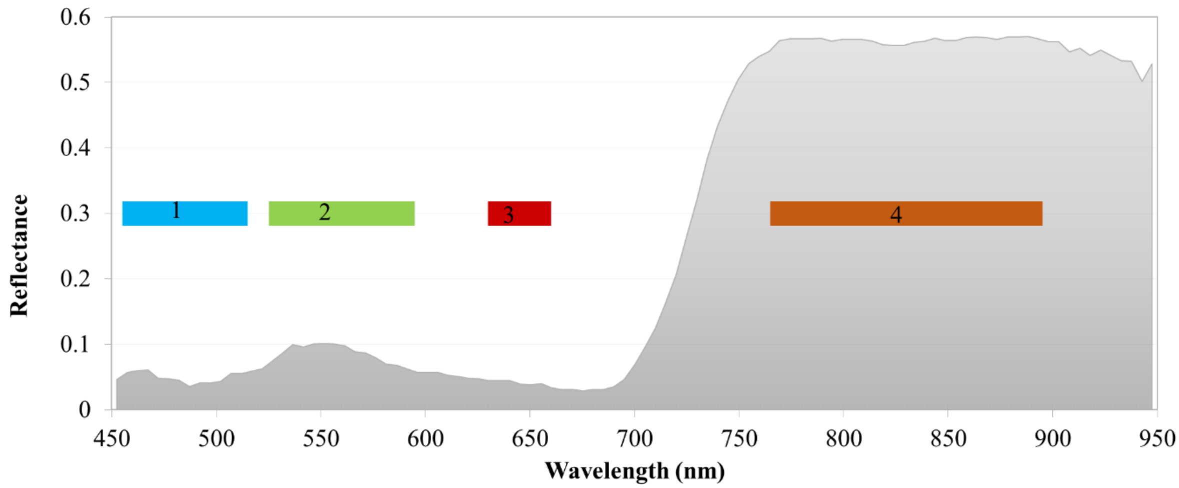

Figure 1: Spectral reflectance of a potato plant obtained from the UAV imagery. The bandwidths of the four Formosat-2 spectral bands are indicated by colored blocks. Many vegetation indices take advantage of the difference between the high reflectance in the NIR region (≈0.55) and the low reflectance in the red region (≈0.05).

NDVI is the most well-known index, but although it clearly separates vegetation from soil in a wide range of illumination conditions, it also tends to be sensitive to soil background effects and saturates at very dense vegetation levels (Broge and Leblanc 2001). The GNDVI uses the same formula, but replacing the red band with the green band, on the basis that the green band is less sensitive to background and atmospheric effects (Gitelson et al. 1996). Similarly, the WDVI attempts to limit the influence of the background soil effect by introducing the parameter *C*, the slope of the so-called soil-line formed by plotting soil reflectance on a scatterplot with the reflectance in the red spectrum on the x-axis and NIR reflectance on the y-axis (Clevers 1989). Other hyperspectral indices, such as MCARI focus on the red-edge spectrum characterized by the significant rise in the reflectance of vegetation from the red to the NIR region to counter the saturation effects of dense vegetation (Daughtry et al. 2000). The MCARI index also limits the influence of atmospheric effects by taking into account the reflectance in the blue spectrum (Haboudane et al. 2004).

3.4 Yield prediction

Previous studies attempt to relate the potato yield factors such as topographical parameters (Persson et al. 2005), soil moisture content and salinity (Dai et al. 2011), and physical and chemical soil properties (Po et al. 2010). However, biophysical parameters such as LAI and chlorophyll concentration represent crop conditions and are also indirectly related to yield (Bala and Islam 2009; Fortin et al. 2011; van Evert et al. 2012; Rahman et al. 2012; Ramírez et al. 2014). Therefore, a number of studies attempt to develop regression models relating the yield of various crops to vegetation indices during the growing season (Zarco-Tejada et al. 2005; Fortin et al. 2011; Rembold et al. 2013). However, these regressions are only applicable to the spatial and temporal extent of the study area due to the complexity of the relations between crop conditions and yield and variability of growth conditions (Rudorff and Batista 1990), and can therefore not be used in a general manner (Baret et al. 1989). This problem is exacerbated when the harvestable yield of the crop in question is below ground (Hayes and Decker 1996), such as potato.

Regression models developed for predicting agricultural yield often focus on using vegetation indices of individual images, the maximum value during the growing season, cumulative values, or integrated values (Rembold et al. 2013). For example, Bala and Islam (2009) related potato yield in India to NDVI, LAI and the fraction of Photosynthetically Active Radiation (fPAR) data obtained from MODIS imagery. They calculated the coefficient of determination (R^2) between the three parameters for 19 MODIS images to the yield, and developed a regression model in which the potato yield was based on the mean NDVI during the growing season. Rahman et al. (2012) compared inter-annual potato yield variation to weekly Vegetation Condition Indices (VCI) obtained from AVHRR imagery. Neale and Sivarajan (2011) compared potato yield to the SAVI at three stages in the growing season, and the integrated SAVI during the entire growing season. Each of these studies obtained linear regression models based on vegetation indices which explained a large part of the yield variability.

4 Data and Methodology

4.1 Study area

A potato field along the border between the Netherlands and Belgium, near the Dutch village of Reusel was selected for the current study (Figure 3). The field is located at 51°10’N, 5°19’W and has an area of approximately 11 ha. The surrounding area is characterized by a temperate climate. The nearest meteorological station is in Eindhoven, at a distance of 24 km from the potato field.

The mean monthly temperature and rainfall over the period 1951-2013 (KNMI 2014) is presented in the boxplots in Figure 2. The mean average temperature ranges from 2.6 °C in January to 17.6 °C in July. The lowest mean precipitation is in March (47.6 mm), and the highest is in July (75.4 mm). The higher temperatures during the summer months often cause a rainfall deficit in this period (Buishand and Velds 2010), which has important consequences for agriculture.

Figure 2 also illustrates that 2013 had a particularly cold spring, but high summer temperatures. In 2013, the potato growing season of this particular field was from April 22nd to October 6th. The rainfall during the growing season was particularly low, except for April and August which were much higher precipitation than average. The land use in the area is mainly intended for agricultural production and interspaced with forests (CBS 2011).

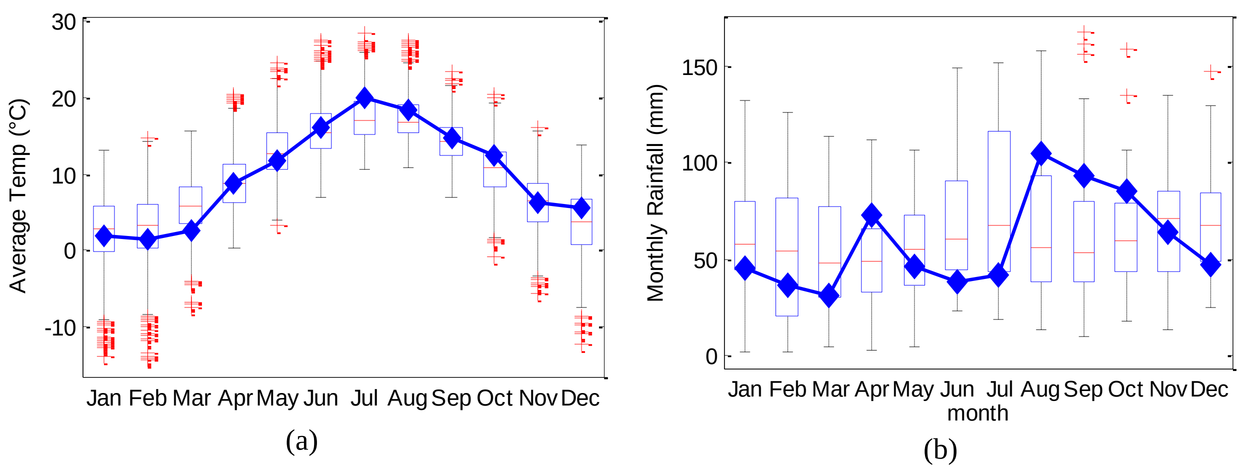

Figure 2: Average monthly temperature (a) and monthly rainfall (b) recorded between 1951 and 2013 at the Eindhoven meteorological station. The horizontal red line of the boxplot represents the median value, surrounded by a blue box presenting the 25th and 75th percentiles. The ends of the whiskers are the minimum and maximum values not considered outliers, which are marked with a red cross (+). The dark blue line with the diamond markers indicate the average monthly temperature and total monthly rainfall for 2013.

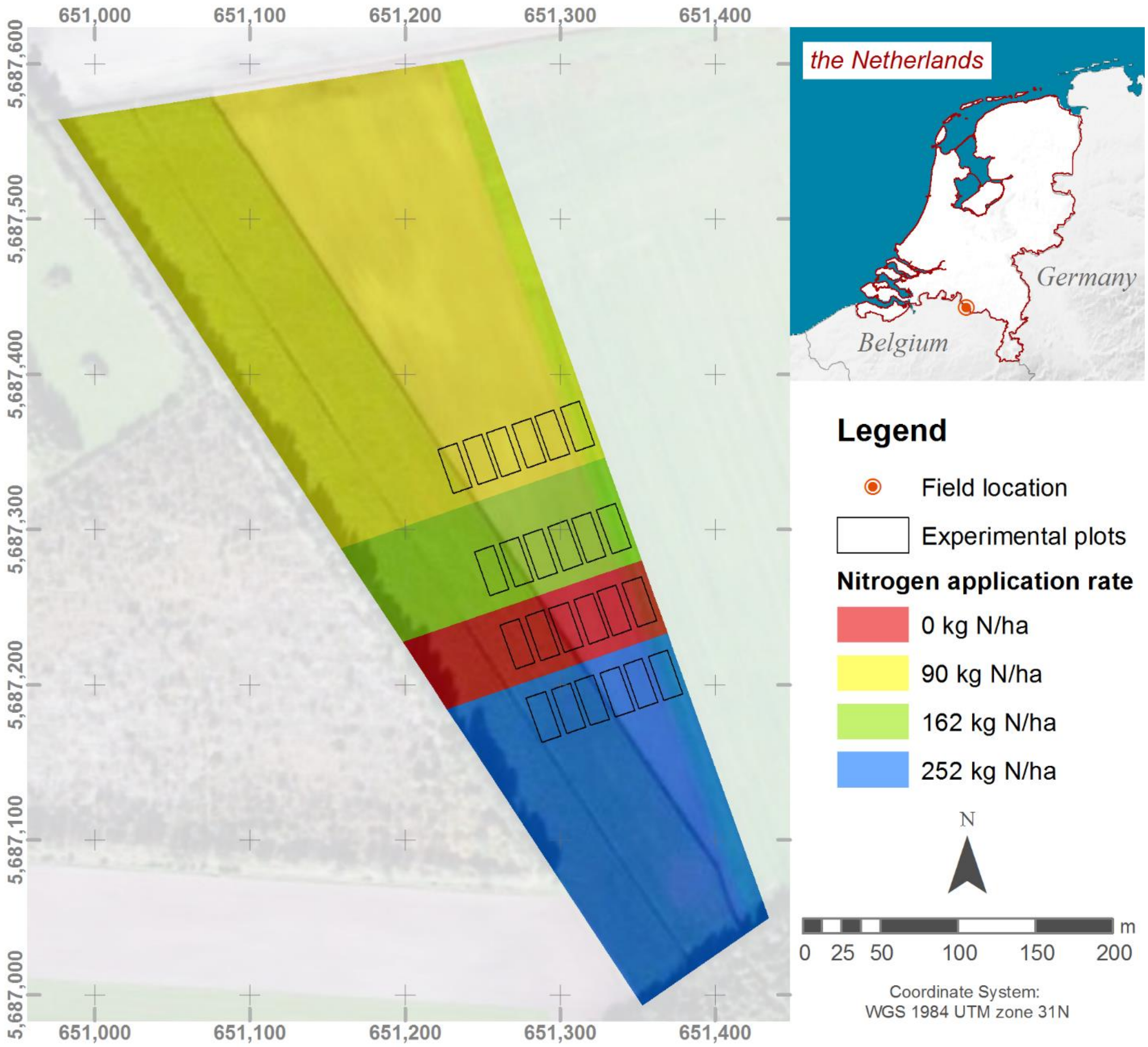

Figure 3: Location of the study area and setup of the nitrogen application rates and experimental plots on the potato field.

This study site was selected for the current research due to a large amount of field data, as well as the application of variable nitrogen fertilization rates at the beginning of the season. This field was subject of a research project executed by the Wageningen University (WU) Laboratory of Geo-information Science and Remote Sensing (GRS) under the Smart Inspectors project (www.smartinspectors.net). At the beginning of the 2013 growing season, four distinct nitrogen fertilization rates (0, 90, 162 and 252 kg N/ha) were applied to the field. Twelve 30 m x 30 m experimental plots (six per fertilization regime) were defined within the field (Figure 3).

Between June 6th and August 23rd 2013, weekly measurements of chlorophyll, LAI and the spectral profile of the potato crop using the 16 band Cropscan multispectral radiometer were taken of the third and tenth rows on both sides of the driving path. Furthermore, a hyperspectral UAV system developed by GRS-WU was flown above the field at four dates (Kooistra et al. 2013). In the current study, each experimental plot was divided in half to analyze the parts to the left and right of the driving plot separately. This created a larger number of plots with a smaller spatial scale to improve the statistical analysis between the satellite imagery and field data. It also removed the tractor driving path from the experimental plots, as the lack of vegetation on the driving path would affect the plot surface reflectance obtained from imagery. Therefore, the current study makes use of 24 13 m x 30 m experimental plots.

4.2 Data

4.2.1 Formosat-2 imagery

There were 42 Formosat-2 images available between March 1st and September 25th, 2013. However, only eight scenes (Figure 4 and Table 1) were cloud-free over the study area. The images display the temporal dynamics of the potato growth. From April 24th to June 8th, the field shows no vegetation as the potato crop is growing. By July 2nd, the canopy has almost closed and the field is much greener, the field is green in all images from July 8th onwards as the potato crop has matured. Slight differences in the colors of the images (i.e. the green between July 18th and July 22nd) are due to atmospheric effects.

Only the multispectral bands with spatial resolution of 8 m were used for this study, as the additional information provided by panchromatic bands does not improve results when quantifying biophysical parameters (Rodrigues et al. 2009). The multispectral images were downloaded from the Netherlands Space Office's (NSO) portal DataDoors (http://nso.datadoors.net/dd3/).

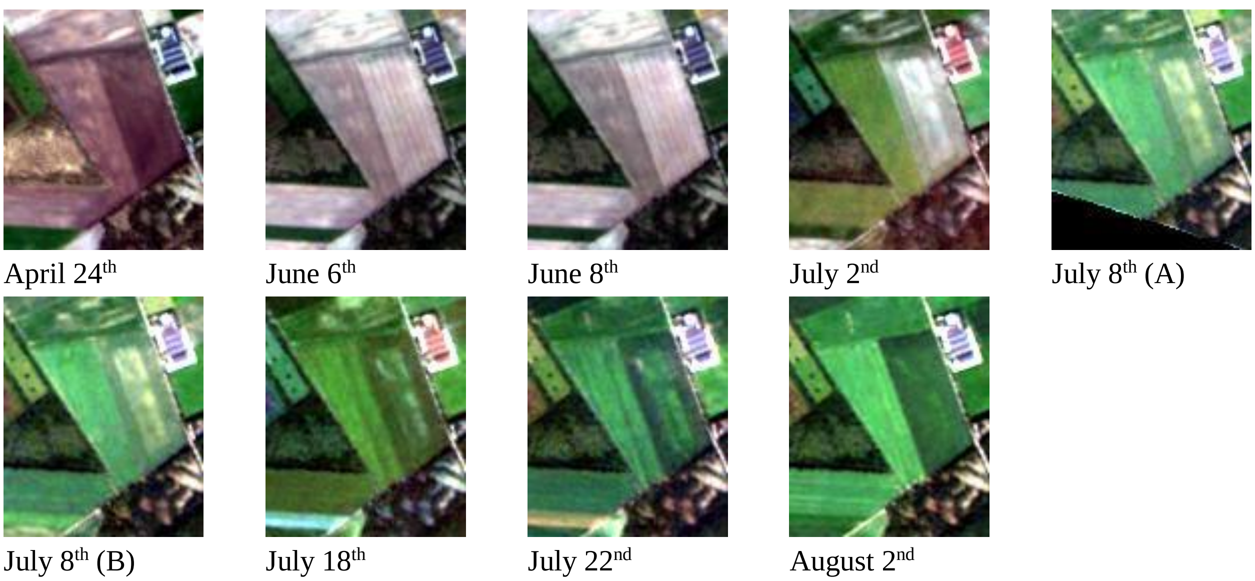

Figure 4: A subset of the Formosat-2 images available during the 2013 growing season, displayed as a true color composite.

Table 1: Dates of the Formosat-2, and UAV imagery utilized in the research.

Formosat-2 imagery	UAV imagery	Field data
24-04-2013		
06-06-2013	06-06-2013	06-06-2013
08-06-2013		
	14-06-2013	14-06-2013
		21-06-2013
		26-06-2013

Formosat-2 imagery	UAV imagery	Field data
02-07-2013		
	05-07-2013	05-07-2013
08-07-2013 (x2)		12-07-2013
18-07-2013	17-07-2013	17-07-2013
22-07-2013		
		26-07-2013
02-08-2013		31-07-2013
		16-08-2013
		23-08-2013

4.2.2 UAV imagery

UAV imagery was available for four dates: June 6th, June 14th, July 5th, and July 17th (Figure 5 and Table 1). The geographical extent of each UAV image in Figure 5 is identical, the differences in image extent are due to the UAV flight path, which was slightly different on each date. As with the Formosat-2 imagery, the UAV image on June 6th displays practically no vegetation. On June 4th, the image already obtains a green color due to increased leaf cover, which is full grown in the images of July 5th and 17th.

The hyperspectral images are obtained with the Specim ImSpector V10 2/3" spectrograph. A GPS inertia navigation system (INS, XSens, MTi-G-700) and a Panasonic GXI +14 mm camera obtained the geographical location and the latter provided data for a Digital Surface Model (DSM) with which the hyperspectral images were orthorectified. Auxiliary instruments included a Digital Signal Processor (DSP) frame grabber, PhotoFocus SM2-D1312 computer, and a LiPo battery. The system was mounted on an Aerialtronics Altura AT8 octocopter. This platform has a maximum payload of 2 kg and a flight-time of 5-8 minutes (Kooistra et al. 2013).

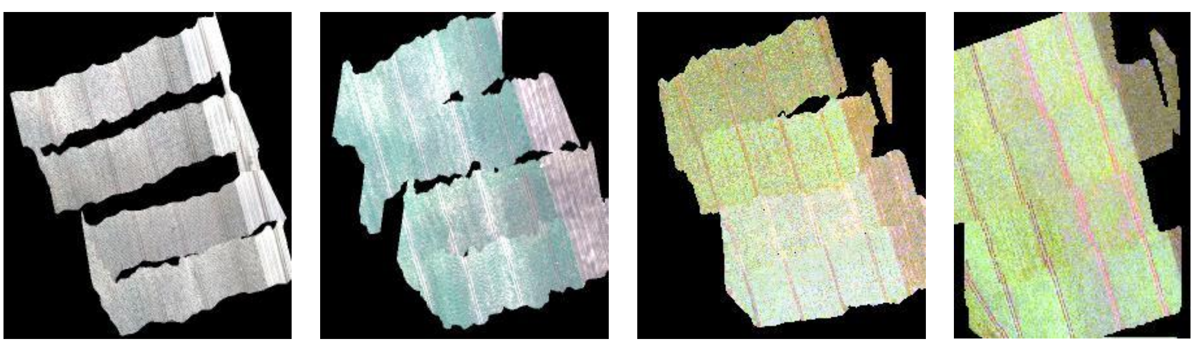

June 6th June 4th July 5th July 17th

Figure 5: UAV imagery available over the study area, portrayed as a true color composite.

4.2.3 Field data

The field data consisted of chlorophyll, LAI and spectral reflectance data at weekly intervals (Table 1). The yield data was measured by the harvesting tractor on October 6th, 2013 using the Yieldmaster PRO

(Figure 6). There were a total of 27,081 sample points providing the potato yield (ton/ha), each experimental plot containing between 76 and 112 (an average of 94) yield sample points. The yield histogram is left-skewed, possibly due to the large amount of low-yield sample points located on the tractor driving paths.

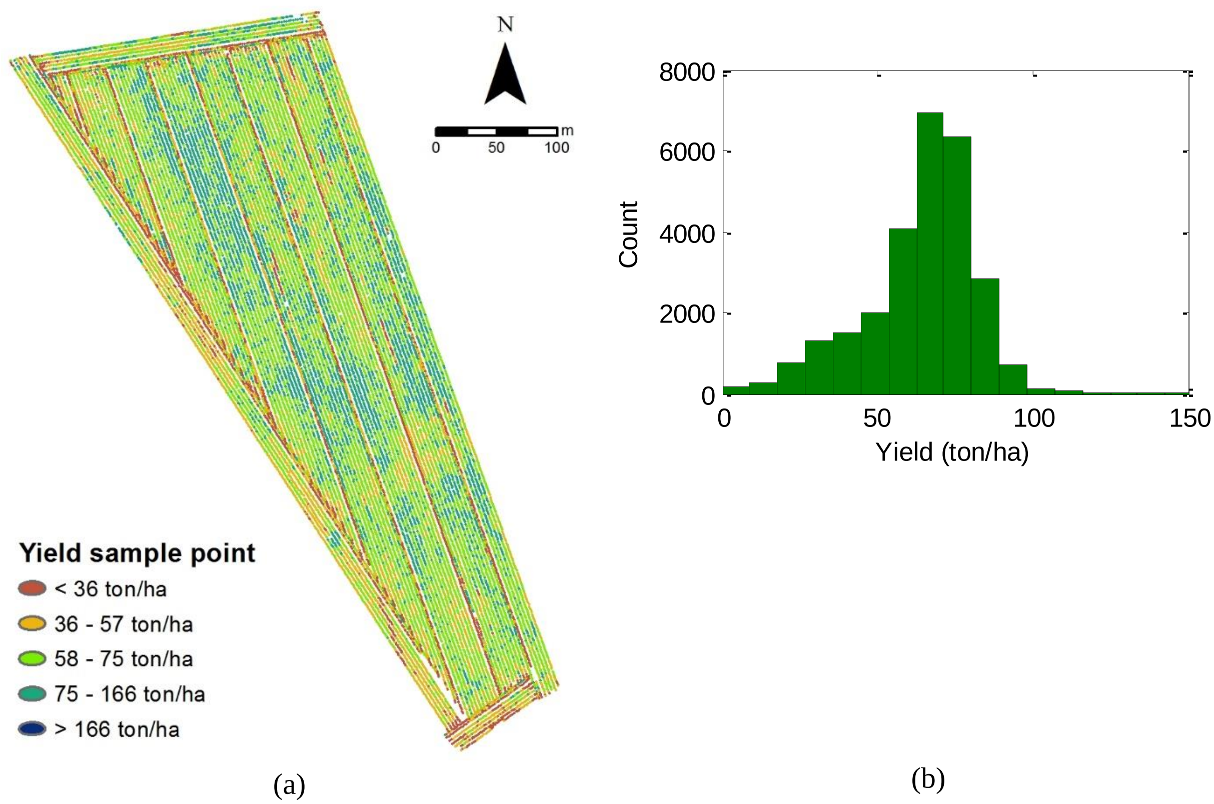

Figure 6: The yield sample points obtained from the harvesting tractor (a), and a histogram displaying the yield measured at the sample points (b).

4.3 Methods

The methodology of the current research can be divided into four phases (Figure 7). The first phase consisted of pre-processing the available data. The Formosat-2 imagery was geometrically and atmospherically corrected. Both Formosat-2 and UAV imagery were clipped to the study extent and prepared for the data fusion. The yield data was interpolated using Empirical Bayesian Kriging. The second phase examines methods to combine the Formosat-2 and UAV imagery. The unmixing-based and STARFM data fusion methods to obtain a dataset with the temporal and spectral resolution of the Formosat-2 imagery and the spatial resolution of the UAV imagery. The results were validated through conventional data fusion indicators (Gao et al. 2006; Zurita-Milla et al. 2011) and a comparison to biophysical parameters measured at plot level. STRS were used to combine the spectral and temporal attributes of reflectance data – creating a reflectance surface displaying the hyperspectral reflectance spectrum on a daily basis. The third phase consisted of the calculation of various vegetation indices. The vegetation index which most accurately represented the spatial and temporal variations of the measured field data was identified and used for further statistical analyses. Finally, the fourth phase consisted of the statistical analysis to validate the results and analyze crop status and yield variability (Section 4.3.5). This phase focused on the evaluation of the fused dataset to represent (i) the crop nitrogen status during the growing season and (ii) the yield variability distribution.

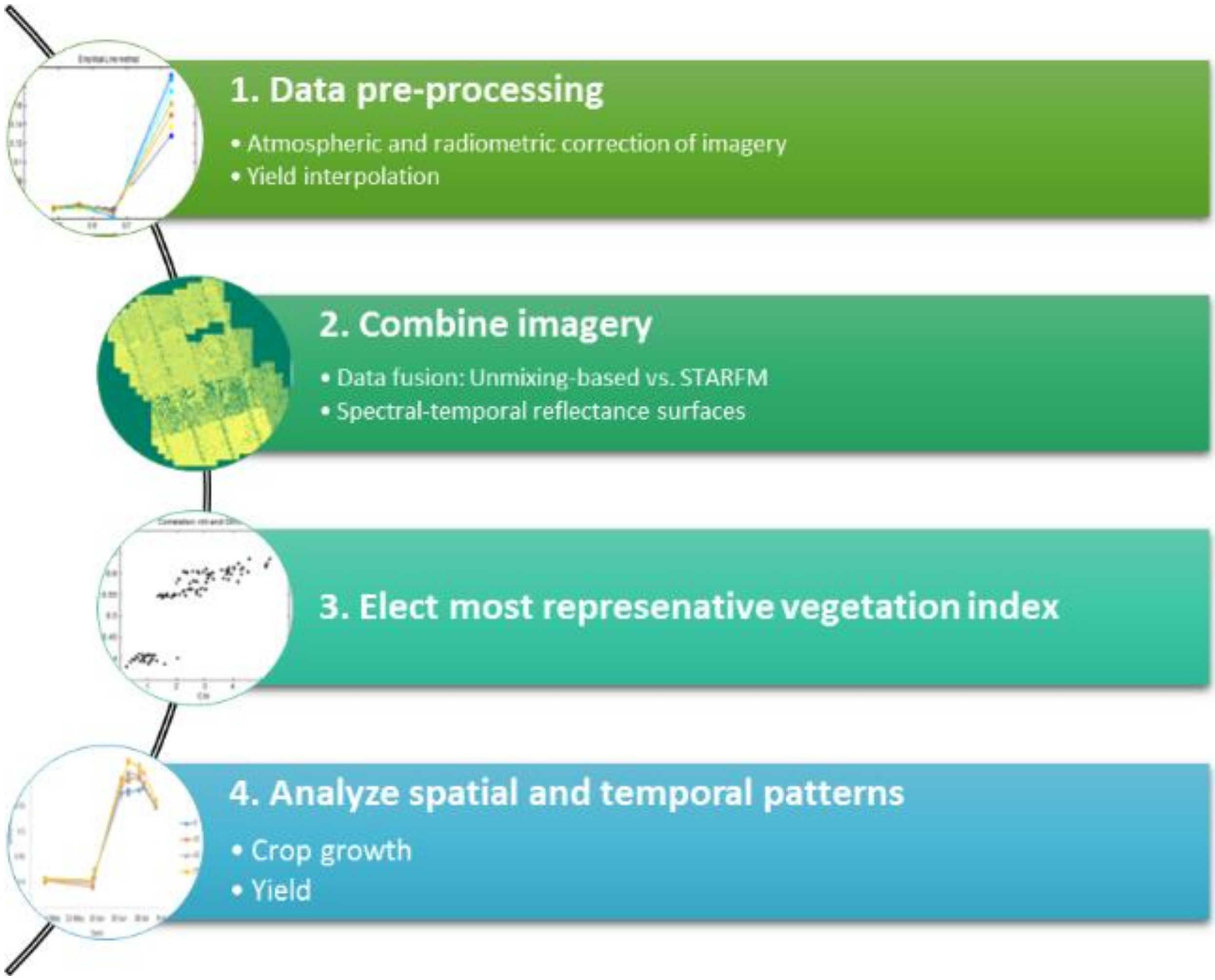

Figure 7: Flowchart of the methodology employed in the current research.

Each step was coupled to a validation process based on the *in-situ* LAI and chlorophyll measurements. The acquired field data was used to identify the most adequate atmospheric correction method (Step 1), validate the quality of the data fusion methods (Step 2), identify the vegetation index which best represents crop status (Step 3), and to verify crop growth variability during the growing season (Step 4).

4.3.1 Data pre-processing

4.3.1.1 Formosat-2 imagery

The images were provided at a level 1A – raw data which had been corrected radiometrically for sensor distortions (Liu 2006). Firstly, the images were geometrically corrected. All images were georeferenced using the Ground Control Points (GCPs) and coregistered to the Formosat-2 image on June 6th. Then, the images were reprojected to the UTM 31N projection system and resampled to the Formosat-2 spatial resolution of 8 m x 8 m using the bilinear interpolation method in ArcGIS 10.2.

The images were then converted from satellite Digital Number (DN) values to Top of Atmosphere (TOA) radiances by using the physical gain parameters obtained from the metadata (Liu 2006). The images were atmospherically corrected using DOS, ATCOR, QUAC, FLAASH, empirical line calibration and radiometric normalization (see Appendix 1). The resulting surface reflectance were compared to the UAV data, of which the QUAC method followed by an empirical line calibration and radiometrically normalized to UAV data obtained the highest correlation and lowest root mean square error (RMSE). Further information regarding this process can be found in Appendix 1.

A unique situation was presented as the study area was located in the overlap between two Formosat-2 scenes on July 8th. Thus, we have access to two distinct Formosat-2 images separated by four seconds. By comparing the processed images of the study area, we can gain insight to the errors induced by the Formosat-2 image processing chain. To this end, the RMSE and correlation between both images was calculated. We hypothesize that these RMSE and correlations obtained in between the two Formosat-2 images on July 8th can be generalized to represent the errors of the other Formosat-2 images in the time series.

4.3.1.2 UAV imagery

The radiometrically, atmospherically and geometrically corrected UAV imagery was provided by WU-GRS. Pre-processing steps had included the conversion of raw data to reflectance, an empirical line correction, and orthorectification using a DSM obtained from the camera onboard the octocopter. Further details regarding the processing of UAV imagery can be found in Kooistra et al. (2013).

For each date, two UAV flights were made, each of which covered half the experimental plots. In the current study, both images were mosaicked using ENVI 5.0 for each date. Invalid data at the edges of the UAV imagery were masked, and the images from various dates were subsetted to the same extent.

4.3.1.3 Yield data

Statistical interpolation models such as kriging derive the spatial influence of proximal samples from the characteristics of the dataset (Krivoruchko 2011). Unfortunately, kriging requires the interpolated data to have a normal distribution, which the yield sample points are not as the histogram is bounded to positive values and is left-skewed (Figure 6b). Therefore, the Empirical Bayesian Kriging (EBK) was used to interpolate the yield data.

The EBK method provides accurate interpolations even when using non-stationary and non-Gaussian data (Pilz and Spöck 2008; Krivoruchko and Gribov 2014). Firstly, outliers were identified in the histogram and removed from the dataset. The EBK method was then applied using the Geostatistical Wizard function of ArcGIS 10.2. The prediction quality was analyzed using the mean prediction error, the RMSE, and the root-mean-square standardized error (RMSSE). The RMSSE divides the prediction error by the standard deviation and normalizes it (Eq. 1.). Therefore, an RMSSE value greater than one indicates an underestimation of data variability, and an RMSSE less than one indicates an overestimation of data variability. The yield prediction and model prediction errors were exported to raster format with the same spatial resolution and extent as the UAV imagery.

$$RMSSE = \sqrt{\frac{\sum_{i=1}^{n}[(\hat{y}_i - y_i)/\sigma]^2}{n}} \qquad \textit{Eq. 1.}$$

Where y_i is the yield measured at a sample point, $\hat{y}_i$ is the predicted yield at that point, σ is the standard deviation of the measured yield, and n is the number of points.

4.3.2 Data Fusion

Optimal input parameters were determined for both fusion algorithms (Appendix 2) and utilized to apply data fusion to each Formosat-2 image. Each time, the Formosat-2 image was utilized as the input medium-resolution image for data fusion. The input high-resolution was always the most recent preceding UAV image. By using only preceding UAV imagery we simulate a practical application in which data fusion is applied during the growing season to monitor crop growth.

As mentioned before, the STARFM method requires a base medium- and high-resolution image pair on the same date. In the current study, coincident Formosat-2 imagery was only available for two dates (June 6th and July 18th). Therefore, only the June 6th and July 17th UAV images can be included in the time series through STARFM fusion. However, the unmixing method only requires an input UAV image, no corresponding Formosat-2 image is needed. Therefore, all four UAV images were used as input for the unmixing-based method.

4.3.3 STRS

4.3.3.1 Theoretical basis

4.3.3.1.1 Spectral interpolation: Bayesian imputation

Proximal hyperspectral bands often display a high covariance (Mewes et al. 2009). Therefore, given the *a priori* covariance of hyperspectral UAV spectral bands, the mean reflectance and distribution at the known Formosat-2 wavelengths, a 101-band reflectance spectrum can be inferred using Bayesian imputation. Thus, rather than fitting the four Formosat-2 spectral bands with a smooth spline interpolation, for example, the physical reflectance characteristics of vegetation are mimicked to create a realistic reflectance spectrum.

Suppose $\boldsymbol{x_{v_i}}$ represents the surface reflectance at the Formosat-2 wavelengths and $\boldsymbol{x_{h_i}}$ represents the unknown surface reflectance at the 5 nm intervals between 450 and 950 nm (corresponding to the UAV imagery) at date *i*. The distributions are jointly Gaussian, defined as follows:

$$p(x_h) = \mathcal{N}(x_h|\boldsymbol{\mu_h}, \boldsymbol{\Sigma_{hh}}) \qquad \textit{Eq. 2.}$$

$$p(x_v) = \mathcal{N}(x_v|\boldsymbol{\mu_v}, \boldsymbol{\Sigma_{vv}}) \qquad \textit{Eq. 3.}$$

Given the *a priori* mean and distribution of the Formosat-2 spectral reflectance ($\boldsymbol{\mu_v}, \boldsymbol{\Sigma_{vv}}$), and the covariance matrix $\boldsymbol{\Sigma}$ of the UAV spectra, the posterior conditional distribution can be obtained:

$$p\left(x_{h_i}|x_{v_i}\right) = \mathcal{N}(x_i|\mu_{(h|v)}, \Sigma_{h|v}) \qquad \textit{Eq. 4.}$$

$$\boldsymbol{\mu}_{\left(x_{h_i}|x_{v_i}\right)} = \boldsymbol{\mu_h} + \boldsymbol{\Sigma_{hv}}\boldsymbol{\Sigma_{vv}^{-1}}(x_v - \boldsymbol{\mu_v}) \qquad \textit{Eq. 5.}$$

$$\boldsymbol{\Sigma}_{(x_{h_i}|x_{v_i})} = \boldsymbol{\Sigma_{hh}} - \boldsymbol{\Sigma_{hv}}\boldsymbol{\Sigma_{vv}^{-1}}\boldsymbol{\Sigma_{vh}} \quad \textit{Eq. 6.}$$

From the posterior mean and distribution ($\boldsymbol{\mu}_{(x_{h_i}|x_{v_i})}, \boldsymbol{\Sigma}_{(x_{h_i}|x_{v_i})}$), the missing spectral value is inferred.

$$\hat{x}_{ij} = \mathbb{E}\left[x_j|\boldsymbol{x}_{\boldsymbol{v}_i}, \boldsymbol{\theta}\right] \quad \textit{Eq. 7.}$$

Although hyperspectral bands display a high covariance between wavelengths, the nature of this covariance will vary depending on the surface properties, i.e. soil vs. vegetation. Therefore, it is important to select adequate *a priori* $\boldsymbol{\mu_v}$ and $\boldsymbol{\Sigma_{vv}}$. The study area of the current application consists of a potato field, so the endmembers within the image range from soil to green vegetation in various stages of growth. It is assumed that the surface spectra within the boundaries of the STRS are represented within the available UAV imagery.

4.3.3.1.2 Temporal Interpolation: Bayesian inference

Previous studies regarding STRS apply standard 2D interpolation techniques to combine the spectral information of various sensors (Mello et al. 2013; Villa et al. 2013). However, in practice imagery obtained from differing sensors often present slightly different spectral reflectance values due to differing wavelengths, bandwidths, radiometric precision, solar geometry and processing chains (Song and Woodcock 2003), etc. Such inconsistencies may degrade the quality of the interpolated surface. An alternative methodology is presented here, which interpolates the temporal dynamics of surface reflectance through a Bayesian inference method.

This method infers a vector of true spectral reflectance **x** from a number of noisy observations **y**. The mathematical formulation is set up as a linear Gaussian system, defining the error as having a normal distribution:

$$y = \boldsymbol{A}x + \epsilon \quad \textit{Eq. 8.}$$

$$\epsilon \sim \mathcal{N}\left(0, \Sigma_y\right), \Sigma_{\mathrm{y}} = \sigma^2 I \quad \textit{Eq. 9.}$$

In these equations, **x** represents the vector of true reflectance values, **y** is the vector of UAV and Formosat-2 observations of this vector. $\boldsymbol{A}$ is a logical *NxD* matrix of the *N* number of observations, or available images, and *D* is the length of the date vector which will be interpolated. This matrix **A** is used to select the dates for which images are available. The noise is assumed to have normal Gaussian distribution (Eq. 9.) with a mean 0 and distribution equal to the observation noise σ^2 multiplied by an identity matrix I.

The prior, **x**, is also defined as a Gaussian distribution (Eq. 10). The temporal profile is assumed to be smooth, meaning that the value of **x** at date *j* is the average of its neighbors (Eq. 11) altered by Gaussian noise (Eq. 12).

$$p(y|x) = \mathcal{N}(\mu_{y|x}, \Sigma_x) \quad \textit{Eq. 10.}$$

$$\mu_{y|x} = -\boldsymbol{L}_1^T \boldsymbol{L}_2 \boldsymbol{x} \quad \textit{Eq. 11.}$$

$$\Sigma_x = (\lambda^2 \boldsymbol{L}^T \boldsymbol{L})^{-1} \qquad \textit{Eq. 12.}$$

$$\boldsymbol{L} = \frac{1}{2}\begin{pmatrix} -1 & 2 & -1 & & \\ & & \dots & & \\ & & -1 & 2 & -1 \end{pmatrix} \qquad \textit{Eq. 13.}$$

Where $\boldsymbol{L}$ is a tri-diagonal matrix (Eq. 13) which selects the central observation as well as the previous and following observations. By multiplying this matrix by the prior precision λ, the user can define the strength of the prior distribution. If the user defines a prior precision λ relatively high compared to the uncertainty of the surface reflectance data ($\lambda \geq \sigma^2$), the resulting temporal profile will be relatively smooth. However, if the user defines a prior precision which is lower ($\lambda < \sigma^2$), the weight of the observations will be relatively higher and the temporal profile will adjust more to the imagery reflectance. More information regarding the formulations of Bayesian imputation and inference can be found in Murphy (2012).

In the current application, the uncertainty σ^2 was obtained from the standard deviation of spectral measurements on the experimental plot. The uncertainty of the Formosat-2 spectra contained an additional error: the variance of the posterior distribution in the imputation step (Eq. 14).

$$\sigma_{F2tot} = \sqrt{\sigma_{F2} + \boldsymbol{\Sigma}_{(x_{h_i}|x_{v_i})}} \qquad \textit{Eq. 14.}$$

4.3.3.2 Application

To obtain realistic spectra in the STRS, the Formosat-2 spectral reflectance were first interpolated in the spectral domain before applying the temporal interpolation. Firstly, *a priori* information regarding the spectra of endmembers within the scene was obtained by creating a spectral library listing all the UAV spectral reflectance in the four available images. This spectral library was convolved using the Formosat-2 normalized spectral response curve to obtain four spectral 'bands' comparable to the Formosat-2 reflectance.

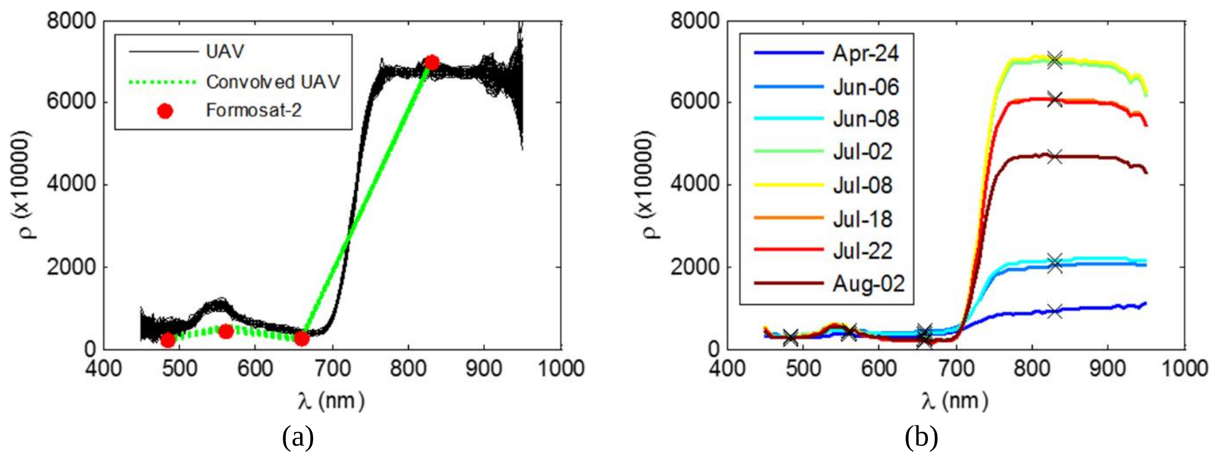

Figure 8: Illustrative figures indicating the spectral imputation method. (a) The Formosat-2 reflectance (red dot), closest samples from the UAV spectral library (black), and UAV reflectance convolved using the Formosat-2 spectral response function (green). (b) The Formosat-2 spectra imputed to 101 bands on various dates. Note how the characteristic vegetation spectrum is preserved.

For each experimental plot for each Formosat-2 image, 100 similar UAV spectra were selected from the convolved spectral library Figure 8. The average, standard deviation and covariance was calculated for each of the hyperspectral UAV bands of these 100 samples, and used as the *a priori* input for Bayesian imputation. Selecting the *a priori* information separately for each experimental plot allows the imputed spectra to represent spatial and temporal variation – i.e. it differentiates between plots with low vegetation growth and a close canopy, allowing for a more accurate interpolation. It is important to note that this methodology assumes that the spectral signatures within the spectral library are representative all the spectra in the STRS. In the current situation, there is a large number of sample spectra (n=73,132), and the library adequately represents the variation in crop growth which is expected to be present within the experimental plot STRS.

The temporal interpolation of the UAV and imputed Formosat-2 spectra was done on a band-by-band basis. For each wavelength, the UAV and imputed Formosat-2 observations were selected, along with their corresponding uncertainties. The observations of the neighboring spectral bands were also utilized as input, but with a doubled uncertainty. In this way, although the temporal interpolation was applied separately for each band (Figure 9), the observations of neighboring bands were also included in the interpolation.

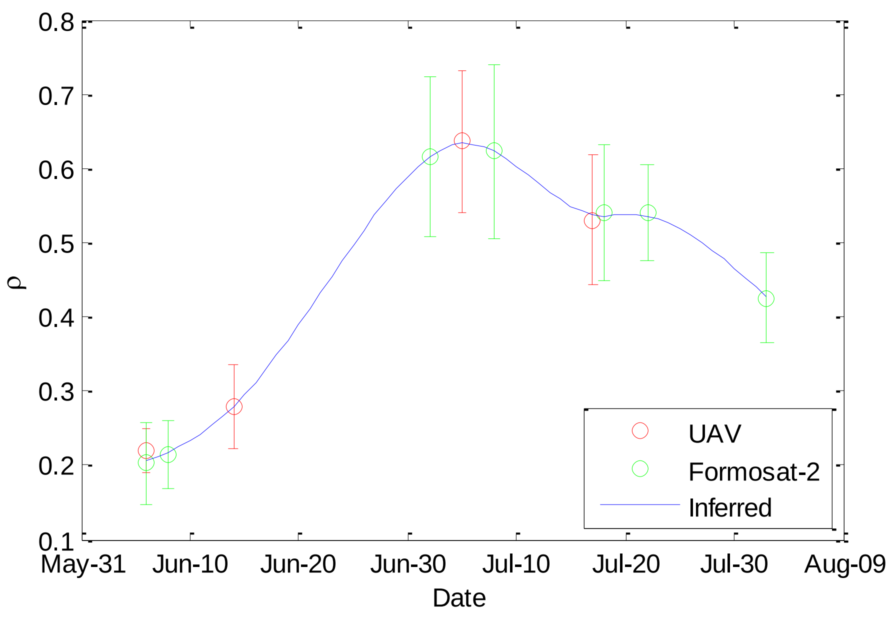

Figure 9: Example of a temporal profile inferred from uncertain UAV and Formosat-2 measurements.

Three STRS were created to illustrate the added value of the described methodology. The first dataset utilized the four Formosat-2 and 101 UAV spectral bands directly as input values, and calculated the STRS using the cubic-spline interpolation method. The second and third methods utilized the imputed Formosat-2 spectra (described above) and the UAV spectra as input. The second method utilized a standard cubic spline interpolation method, whereas the third utilized the Bayesian approach method consisting of spectral imputation followed by temporal inference as described previously.

4.3.4 Vegetation indices

The third phase consisted of the calculation of various vegetation indices to prepare for the statistical comparison of the images to the field and yield data. The current study applies a number of multispectral and hyperspectral vegetation indices (Appendix 3). The vegetation index with the highest correlation to LAI and chlorophyll data measured at the field level was selected for the subsequent analysis steps. A number of multi- and hyperspectral vegetation indices were also calculated from the Bayesian-theory based STRS.

To compare the fused and STRS datasets to the reference field data, the WDVI was also calculated from the Cropscan multispectral radiometer field measurements, henceforth known as *field WDVI*. It should also be noted that the correlations were calculated on four dates for the fused imagery dataset, and nine dates for the STRS – due to the availability of coinciding field data.

4.3.5 Statistical analyses

The statistical analysis of the current study addresses the following four questions: (1) Can the results of data fusion and STRS be validated by field data? (2) Can vegetation indices be used to identify effects of different nitrogen fertilization rates on crop growth during the growing season? And (3) can yield variability be explained by crop growth parameters obtained from the image sets?

The first question requires validating the results of data fusion and STRS using the field data. The WDVI (Appendix 3) was selected because previous studies with this UAV imagery indicated a good correlation to the field LAI data (Kooistra et al. 2013). The WDVI was calculated for the fused datasets on the reference dates: June 6th, July 5th, July 18th, and August 2nd. It was assumed that biophysical parameters did not change significantly within a three day interval (e.g. between the Formosat-2 imagery of July 5th and the field data of July 2nd and August 2nd vs. July 31st). These values were then compared to the corresponding vegetation indices, chlorophyll, and LAI measured at the field level using the RMSE and Spearman's correlation coefficient. Similarly, the validation of the STRS calculated Spearman's correlation coefficient between the WDVI and MCARI (Appendix 3) vegetation indices obtained from the STRS on all nine dates for which field data was available.

Regarding the second question, the vegetation index displaying the highest correlation to the biophysical parameters measured at field level were used to create a temporal profile for each experimental plot. The ability of the fused images to identify crop status variability due to differing initial nitrogen fertilization rates was analyzed using a statistical variance test. A Kruskal-Wallis statistical test (Sheskin 2003) was applied in Matlab R2012b to determine whether the vegetation index variance is significantly different between the nitrogen application rate regimes. This provides insight to whether the nitrogen application rates cause significant differences in crop growth, and at which dates such differences were visible.

The third question attempted to relate the yield variability to biophysical parameters during the growing season. Again, a grouped Kruskal-Wallis test was applied to determine if the four different fertilization regimes caused differences in yield, and which regime obtained the highest mean yield. Then, a stepwise multivariate regression analysis (Fidell and Tabachnik 2012) was applied in IBM SPSS Statistics 22 to determine the relation between the yield and a number of independent parameters at experimental plot level. The entry threshold for a variable was p=0.05, and the exit threshold of the stepwise regression was p=0.10.

Ten regression models were developed, based on differing input parameters. The first two models were based on the measured field data. It was hypothesized that the first model, based on the LAI and chlorophyll measurements, would explain the largest amount of yield variability, as these parameters are direct indicators of crop status. The second model used parameters based on the GNDVI measured at field level. It was hypothesized that this gives an indication of the largest amount of yield variability which can be explained based on vegetation indices rather than biophysical parameters. The other eight models were based on the following parameters obtained from either the unmixing-based, Formosat-2, or UAV images or the STRS:

1. The GNDVI of each available image,
2. The integrated GNDVI up to the date in question to represent crop status variability (Comar et al. 2012). This was obtained using the trapezoidal integration method in Matlab R2012b on the temporal GNDVI profiles (date along the x-axis and GNDVI along the y-axis, see Figure 10 a).
3. The sum of the Euclidean distance between the GNDVI of the experimental plot with the highest yield and the experimental plot in question for each available image. This represents the difference between the GNDVI profile of a plot and the GNDVI profile of the plot with the highest yield (Figure 10 b).

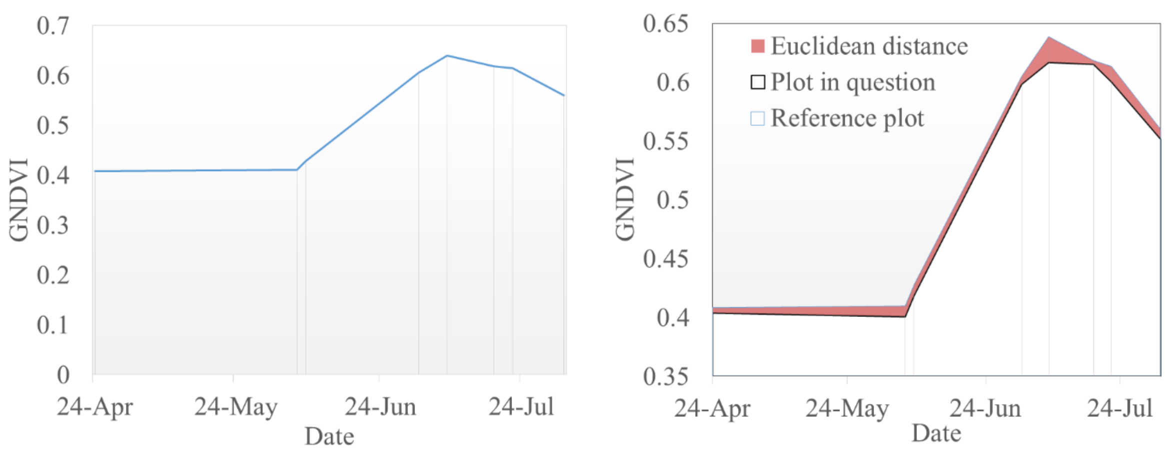

(a) (b)

Figure 10: The integrated GNDVI (a) is calculated by changing the temporal profile into a series of trapezoids under the temporal GNDVI profile, and summing the area of each trapezoid up to the date in question. The Euclidean distance, marked in red, (b) is calculated by summing the difference between the GNDVI profile of the plot in question and the GNDVI of the plot with the highest yield ("reference plot" in the example) at each available image date.

Models 3-6 used all four types of input parameters to predict yield variability (one for each dataset: unmixing-based imagery, Formosat-2 imagery, UAV imagery, or STRS). It was hypothesized that the Euclidean distance parameter has the highest relation to yield, because the more the temporal GNDVI profile of a plot deviates from that of the plot with the highest yield, the more likely it is to have a lower yield. However, this parameter is only available at the end of the season. Therefore, a second group of models (Models 7-10) used only the GNDVI per image and integrated GNDVI as input parameters, simulating an application in which yield variability can be predicted during the growing season.

5 Results

5.1 Data pre-processing

5.1.1 Formosat-2 imagery

A combination of the QUAC and empirical line atmospheric correction methods obtained the most accurate Formosat-2 surface reflectance when compared with UAV data (see details in Appendix 1). Figure 11 presents the reflectance spectra of one pixel for all Formosat-2 images using the QUAC method (a), and after the empirical line calibration (b). The empirical line calibration clearly normalizes the spectra of images at different dates, facilitating temporal analyses.

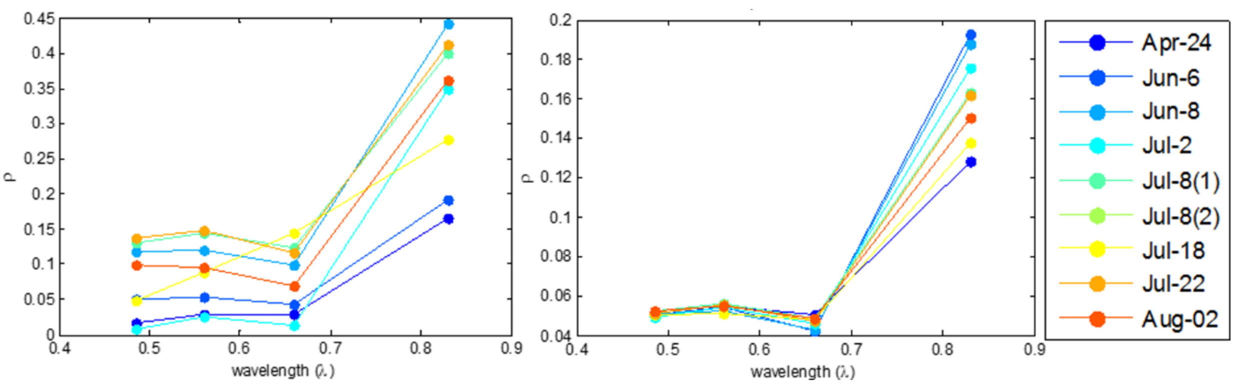

(a) (b)

Figure 11: Comparison between the reflectance values of the same pixel for all Formosat-2 images corrected by the QUAC method (a), and after empirical line calibration (b).

The surface reflectance of two images on July 8th over the study area were also compared. The strong correlation between the spectral reflectance of all bands is significant ($r=0.9991$ at $\alpha<0.001$; RMSE = 0.0047) suggest the errors induced by the processing chain are minimal.

5.1.2 Yield interpolation

The results of the EBK interpolation of yield data points obtained a mean error of -0.03 ton/ha, an RMSE of 8.05 ton/ha and a RMSSE of 0.87. The low mean error indicates a low bias and high accuracy in yield predictions. The satisfactory RMSE indicates a good precision of the model. The RMSSE is slightly less than one, indicating a slight overestimation of the yield variance (Krivoruchko 2011).

Figure 12 displays the interpolated yield map and prediction errors. The tractor driving paths are clearly visible in the interpolated yield map, as well as the influence of the no initial fertilization zone. The prediction error map displays more similarity between measuring points in the North-South direction than in the East-West direction. This is due to the systematic linear sampling pattern of yield data along the tractor driving paths.

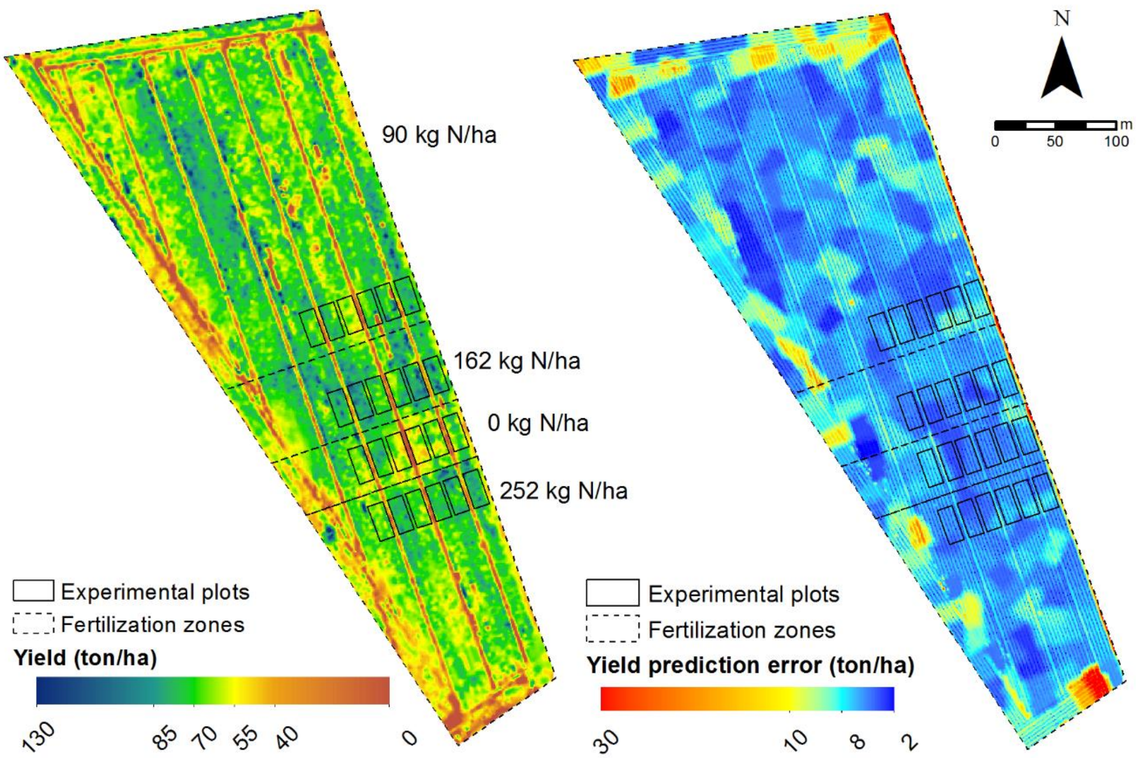

(a) (b)

Figure 12: The interpolated yield map (a) and prediction errors (b) in ton/ha.

5.2 Data fusion

Using the parameters defined in Appendix 2, both fusion methods were applied to create fused images for each date with available Formosat-2 imagery. For example, Figure 13 displays a time series of the GNDVI calculated from the results of the unmixing method and Figure 14 displays the GNDVI from the results of the STARFM method.

Figure 13 indicates that differences in crop status due to differing fertilization rates can be identified starting from July 2nd. The STARFM method (Figure 14) only displayed clear differences between the differing nitrogen fertilization rate zones after July 18th. This difference is likely due to the algorithm requirements, which allows the unmixing method to utilize input UAV images with no corresponding Formosat-2 imagery. Therefore, the fused dataset of July 2nd is based on the UAV image on June 14th in the unmixing-method, but on the UAV image of June 6th in the STARFM method.

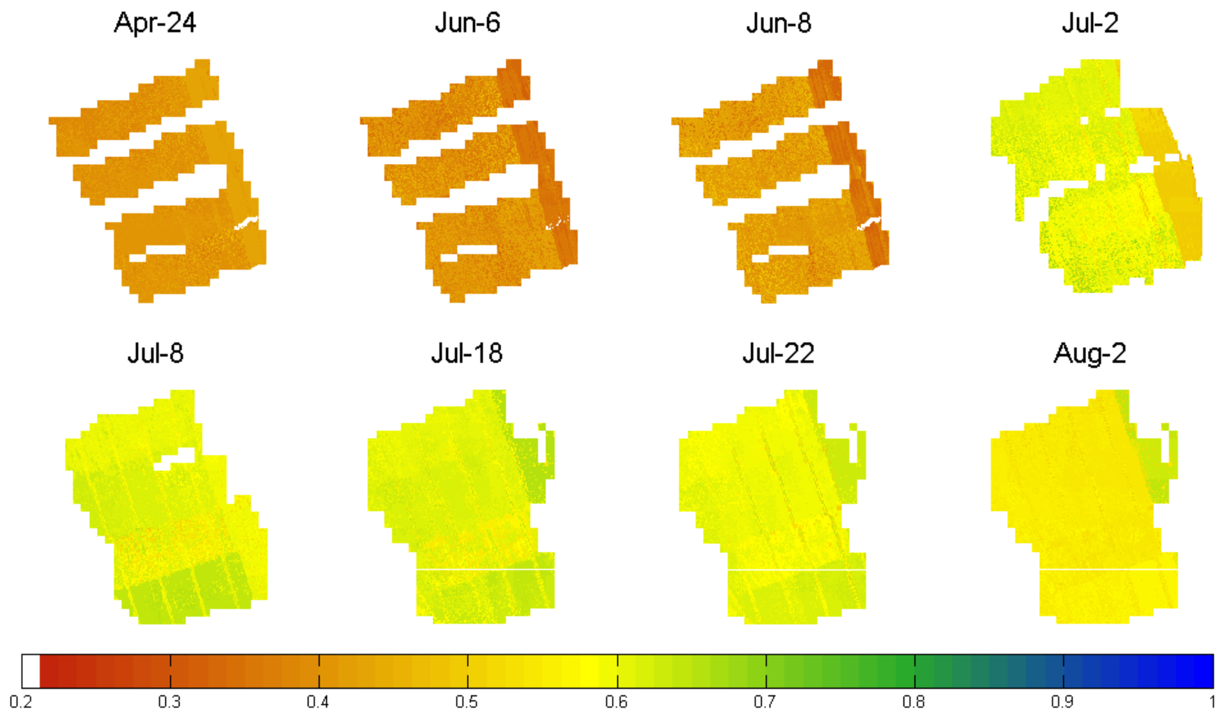

Figure 13: The GNDVI calculated from images fused by the unmixing-based method.

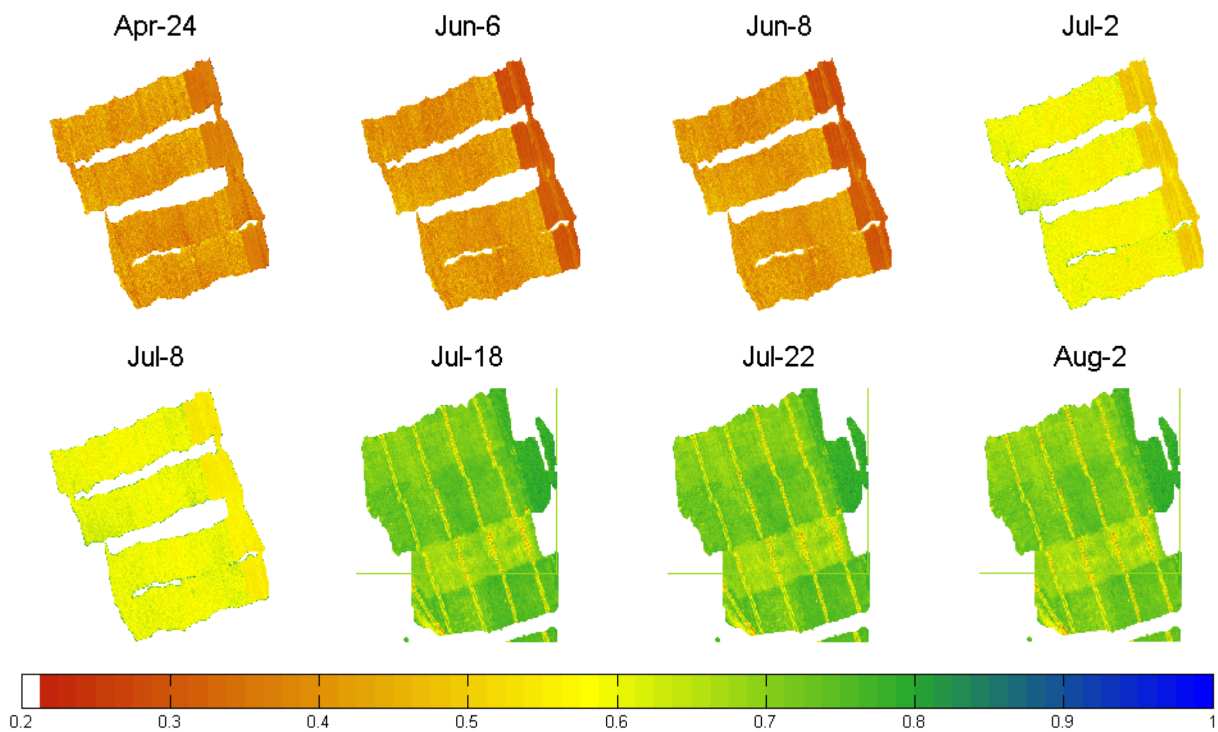

Figure 14: The GNDVI calculated from images fused by the STARFM method.

The Spearman's correlation coefficients (r_s) between the WDVI calculated from the fused images and the measured LAI and chlorophyll concentration (Chl) on June 6th, July 5th, July 18th, and August 2nd are given in Table 2. All correlations are significant (at α<0.001).The table indicates that the STARFM

WDVI has the lowest correlation to all field data. The correlation coefficient of the unmixing-based WDVI (r_s=0.802) to the field data is comparable to the correlations obtained from the original UAV (r_s=0.847) and Formosat-2 (r_s=0.808) data. The RMSE of the unmixing-based method is equal to that of the Formosat-2 WDVI (0.310) whereas the STARFM method the same RMSE as UAV WDVI (0.214). This is logical as the unmixing-based method obtains spectral reflectance from the Formosat-2 imagery, whereas the STARFM method obtains spectral reflectance from the UAV imagery.

Table 2: Correlation coefficients (r_s), RMSE and probability of the Wilcoxon rank sum test between field data and WDVI calculated from the UAV imagery, Formosat-2 imagery (F2), results of unmixing-based fusion (UM) and STARFM-based fusion (SM). All correlations are at significant at α<0.01.

Method	Field data	WDVI			
		UM	SM	UAV	F2
Spearman's r	Field WDVI	0.802	0.463	0.847	0.808
	LAI	0.866	0.477	0.872	0.861
	Chl (g/m^2)	0.884	0.431	0.882	0.869
RMSE	Field WDVI	0.310	0.214	0.214	0.310

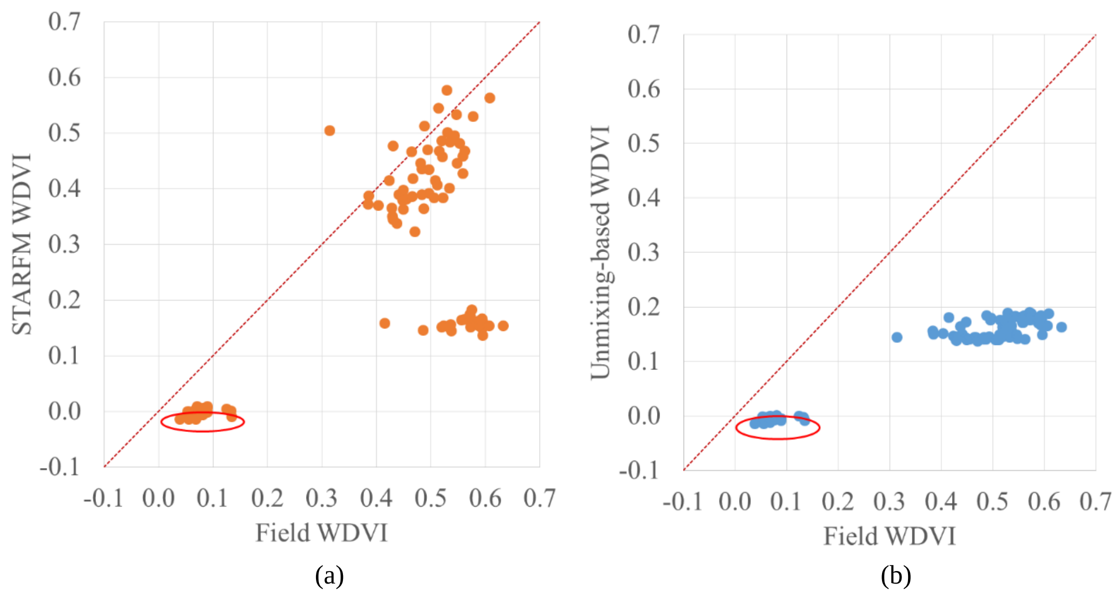

Figure 15: Scatterplot between WDVI measured at field level and WDVI calculated from the STARFM (a) and unmixing-based fusion (b). The red circles indicate negative WDVI values.

A scatterplot of the field WDVI against the WDVI obtained from the fused images is given in Figure 15. The WDVI obtained from the fused imagery displays slightly negative values (marked by red circles), this is possible due to the soil background in the imagery. The field WDVI does not contain negative values as the hand multispectral radiometer was pointed directly at vegetation when obtaining measurements, significantly reducing soil background effects. Although the STARFM method is often closer to the 1:1 line, it is highly sensitive to variations between input images on different dates. For example, for the same range of field WDVI values from 0.4 - 0.6, there is one group of STARFM WDVI concentrated between 0.1 and 0.2, and another group between 0.3 and 0.6 (Figure 15). This illustrates the instability of the STARFM errors, and explains the low correlation between the STARFM WDVI and field parameters in Table 2.

From each dataset, temporal profiles can be constructed to analyze the crop status during the growing season. Figure 16 presents the normalized temporal GNDVI profiles of two of the experimental plots receiving maximal initial fertilization (a) and no initial fertilization (b). These two plots are representative for the temporal profiles of all the other plots, which are not displayed here.

Figure 16 illustrates that the UAV GDNVI closely follows the field observations, but no UAV imagery is available after July 17th (day 87 of the growing season). Unmixing-based data fusion contains the spectral information of the Formosat-2 imagery, which is why the Unmixing-based and Formosat-2 temporal profiles are so similar. The STARFM method clearly shows the influence of the input base image pair, and does not provide consistent results compared to the field data. However, the temporal variation of the Formosat-2 and unmixing-based imagery follows the temporal pattern of the field data, although the absolute GNDVI is systematically lower. Furthermore, the GNDVI profile of the fused imagery extends to after the last collection of the UAV imagery, displaying the temporal resolution advantages of data fusion in the current application.

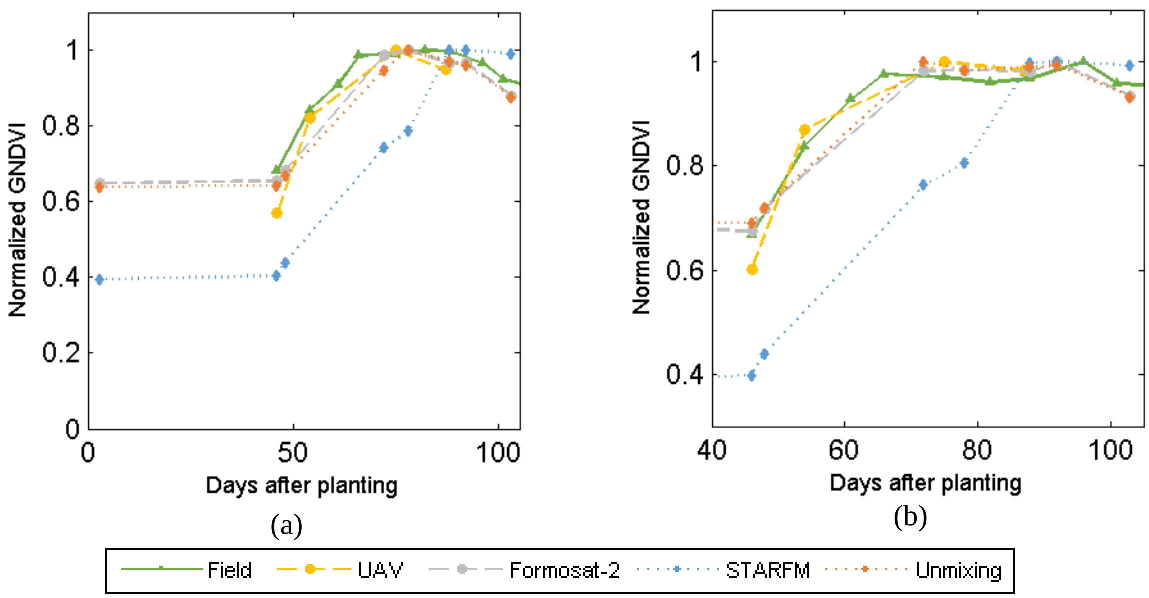

Figure 16: Temporal WDVI profiles of experimental plot A_L under the maximal fertilization regime (a), and field B_L with no initial fertilization (b).

5.3 STRS

The STRS of an experimental plot using each of the three methods are presented in Figure 17 and Figure 18. The other 23 experimental plots with similar results will not be presented here. All figures display low reflectance values at the beginning of the season, as there is little vegetation and a large influence of the soil background. The reflectance increase and reach a maximum at the beginning of July, where the high reflectance in the green and NIR regions are characteristic for green vegetation. At the end of the season, the green and NIR reflectance decrease again due to leaf senescence.

By imputing the Formosat-2 spectra first as in Figure 17 (b), the resulting spectra at each date of the STRS retain the traditional spectral characteristics of vegetation. However, if these spectra are interpolated directly without taking into account the uncertainty of the individual sensors, the cubic spline interpolation causes spectra to change rapidly in short time periods. For example, the mean Formosat-2 reflectance on July 8th and July 18th are slightly lower than the UAV reflectance on July 5th and July 17th. This causes the two peaks in green reflectance (≈560 nm) at these dates.

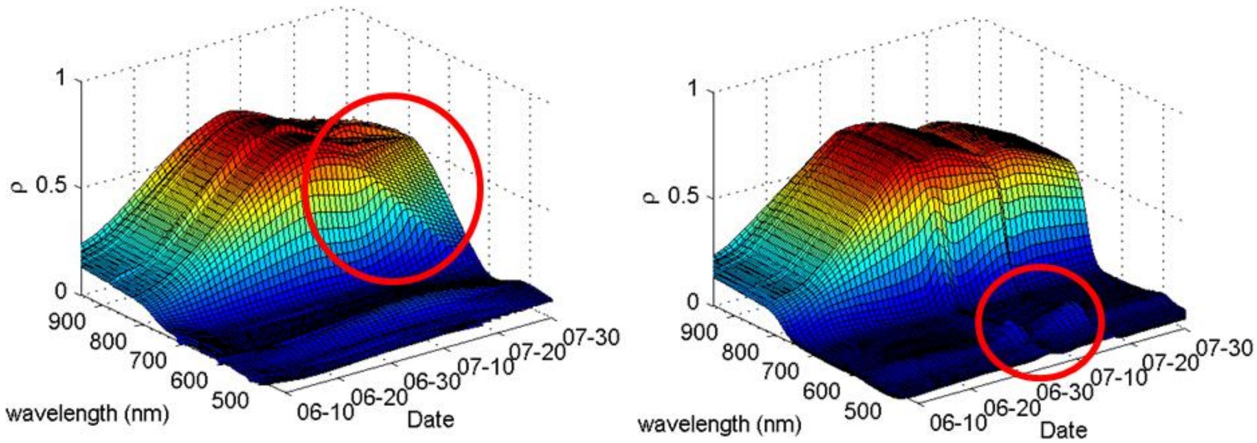

(a) (b)

Figure 17: STRS of experimental plot A_L created by cubic spline interpolation of UAV and original Formosat-2 (a) vs. imputed Formosat-2 (b) spectra. Note the flattening of the red-edge marked by a red circle (a), causing unrealistic vegetation spectra at the end of July. Also note two 'peaks' in the green spectrum marked by a red circle in (b).

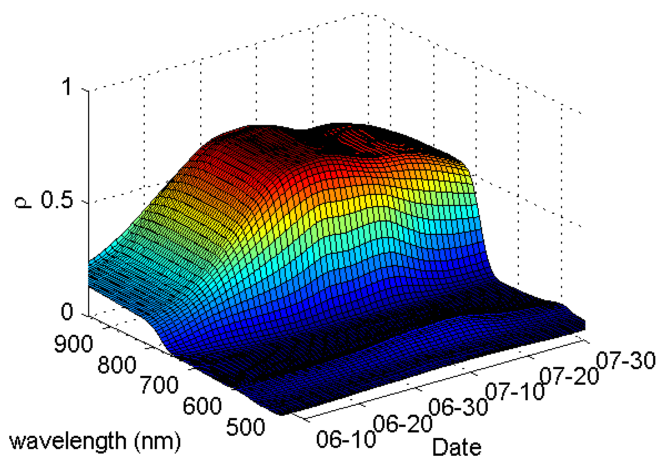

Figure 18: STRS of experimental plot 1 using the new Bayesian approach.

The STRS presented in Figure 18 contains realistic spectra with smooth temporal changes – which could be expected from growing vegetation. Moreover, the vegetation indices obtained from this STRS method obtains better correlations to field data than the other two methods (Table 3).

The reflectance spectra of the STRS were validated by calculating vegetation indices (i.e. WDVI and MCARI, see Appendix 3), and comparing these to the indices obtained from the Cropscan measurements in field. The correlation between the WDVI obtained through the STRS and the field data is similar for all three methods. However, the MCARI obtained through the Bayesian approach method has a much higher correlation to field data than the other two methods.

Table 3: Correlation coefficient between vegetation indices obtained from STRS and the same vegetation index obtained in the field as well as the field LAI and canopy chlorophyll measurements.

		Direct spline	Impute + spline	Bayesian approach
WDVI	Field OSAVI	0.987	0.956	0.980
	LAI	0.857	0.863	0.857
	Canopy Chl	0.821	0.788	0.788
MCARI		Direct spline	Impute + spline	Bayesian approach
	Field MCARI	0.384	0.584	0.934
	LAI	0.333	0.646	0.856
	Canopy Chl	0.094	0.623	0.781

5.4 Vegetation indices

The vegetation indices with the highest correlations to field LAI and canopy chlorophyll measurements were selected for both the fused imagery and the STRS. Section 5.2 indicated that the unmixing-based method provided fused images with more stable prediction errors, whereas the STARFM method had highly variable prediction errors, as indicated in previous studies (Gevaert and García-Haro 2014). Therefore, the unmixing-based method was used for further analyses regarding optimal vegetation indices, temporal analysis and yield applications.

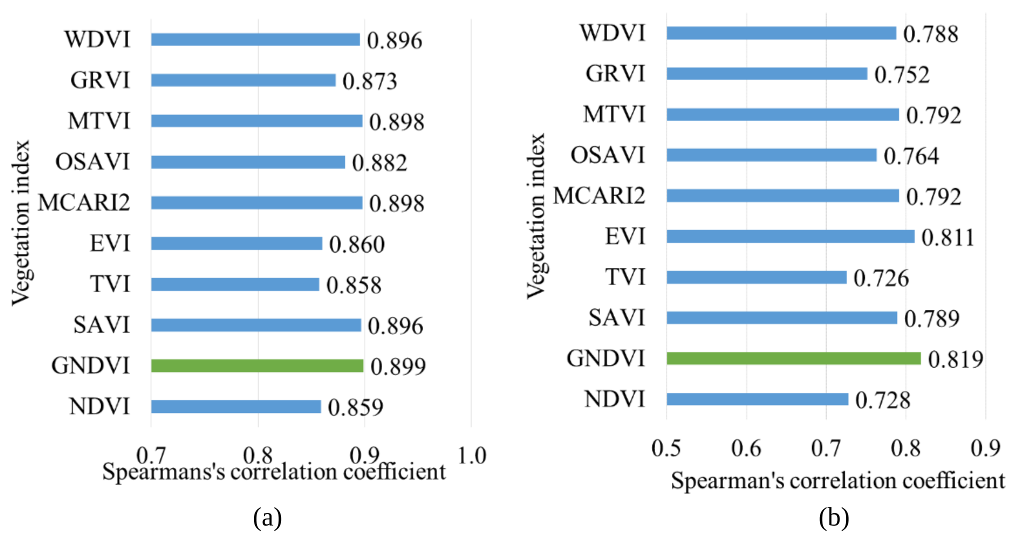

Figure 19: The correlation of vegetation indices calculated from the unmixing-based imagery to the LAI (a) and canopy chlorophyll (b) measured at field level.

Figure 19 gives the correlation between various vegetation indices (calculated from the unmixing-based images) and the LAI (Figure 19 a) and canopy chlorophyll (Figure 19 b) measured at field level for the same four dates used above (see Section 5.2). The index of GNDVI displayed the highest correlation to both LAI (r_s=0.899) and canopy chlorophyll (r_s=0.819). The other vegetation indices displayed correlations above 0.859 to the LAI and above 0.726 to the canopy chlorophyll. It was concluded that the GNDVI obtained from the unmixing-based imagery was most representative of the field data in the current study, and was therefore used in the further analyses.

Correlation coefficients between vegetation indices obtained from the Bayesian STRS and field data is given in Figure 20. The WDVI (r_s=0.857; r_s=0.778) and $WDVI_{green}$ (r_s=0.857; r_s=0.788) obtained the highest correlations to LAI and chlorophyll respectively, followed by the hyperspectral MCARI index (r_s=0.856; r_s=0.781). As was observed from the correlation results of the fused imagery, many vegetation indices obtained similar performances. The WDVI was selected as the vegetation index most representative of the plant biophysical parameters, and utilized in further analyses.

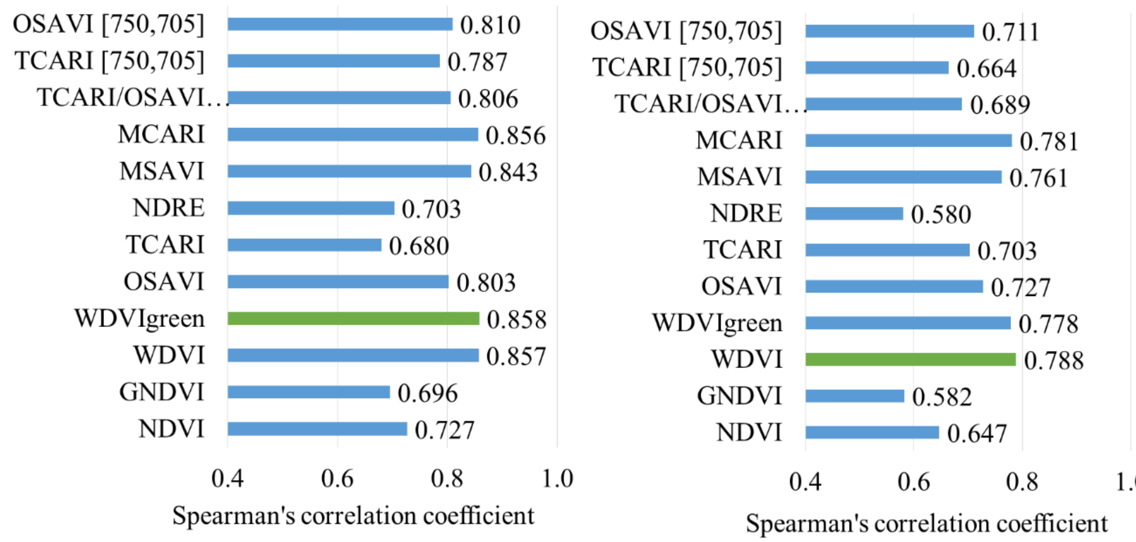

(a) (b)

Figure 20: The correlation of vegetation indices calculated from the STRS to the LAI (a) and canopy chlorophyll (b) measured at field level. The first seven indices (OSAVI [750,705] - TCARI) require narrow hyperspectral bands not present in the Formosat-2 imagery, and the last five vegetation indices (OSAVI – NDVI) only require broader multispectral bands.

5.5 Statistical analysis

5.5.1 Variation detection during the growing season

The objective of in-season crop status variation detection is twofold. The first is to determine whether different plots display significant GNDVI differences during the observed days, and if these differences can be related to the four initial nitrogen application rate regimes. The second objective is to identify where in the growing season the largest differences are visible. This step was applied to the unmixing-based data fusion time series and the STRS separately.

Figure 21 displays the mean GNDVI per fertilization regime for each fused image. In general, the GNDVI displays different stages of crop growth for each regime. The GNDVI increases from April 24th until June 2nd, when it reaches a plateau, representing the mature crop growth stage. Towards the end of the growing season (i.e. August 2nd), the GNDVI decreases due to leaf senescence. After July 8th, the GNDVI of plots from different fertilization groups displayed significant differences (α<0.05), indicating that the initial fertilization regime caused significant differences in crop growth at these dates. Plots with the highest initial fertilization rates had the highest GNDVI values, whereas those receiving no initial fertilization had lower GNDVI values.

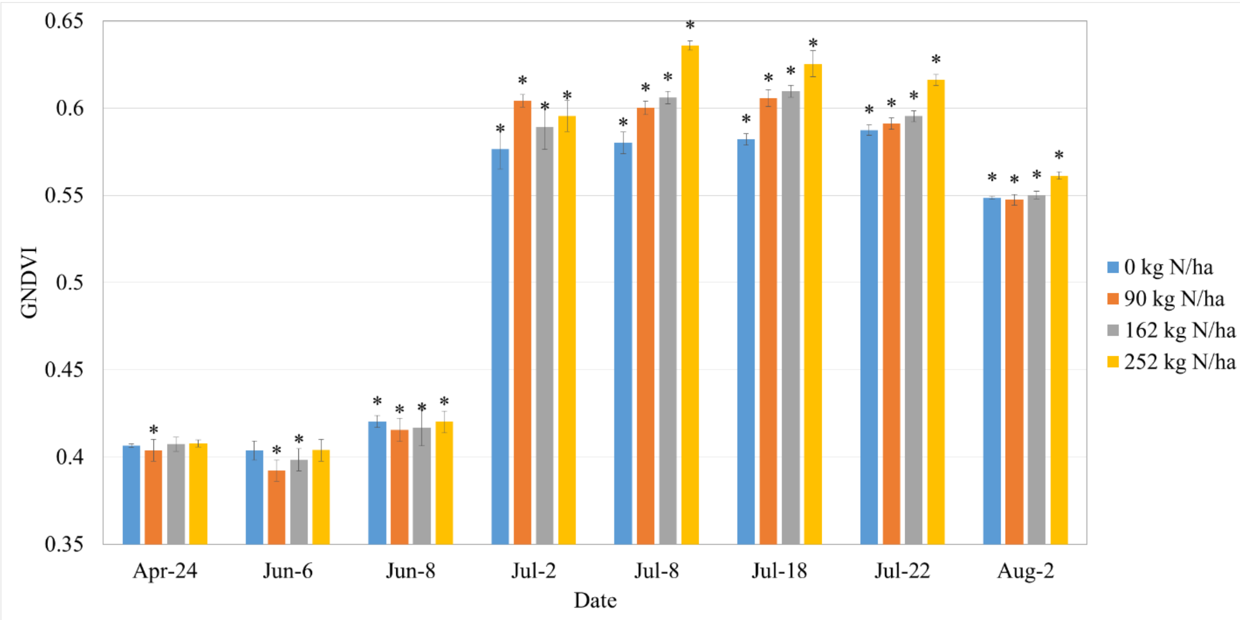

Figure 21: Temporal GNDVI profiles of the fused images grouped by fertilization regime. Asterisks indicate significantly different means from the other fertilization regimes (α<0.05; n=1140) on the same day according to the Kruskal-Wallis test. The error bar of each column represents the standard deviation of the GNDVI within each experimental plot per fertilization regime.

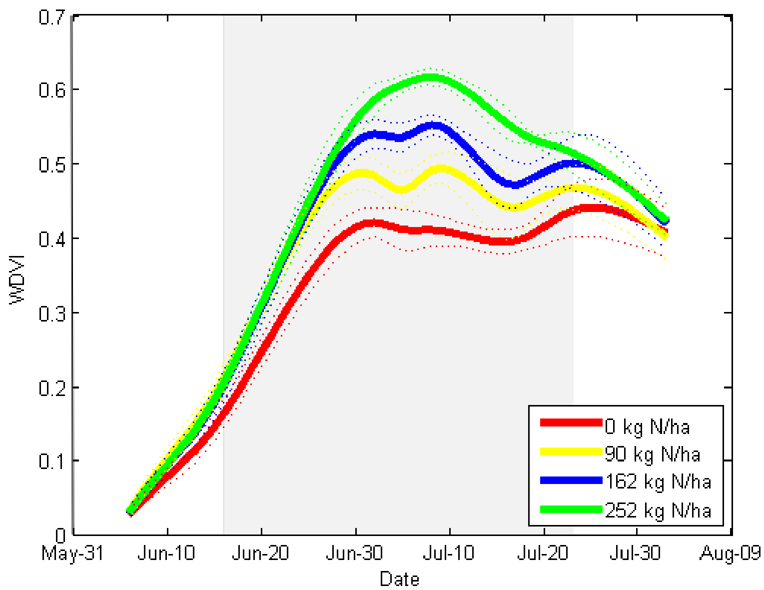

Figure 22: Temporal profiles displaying the average WDVI per fertilization regime. The black outline marks dates where the Kruskal-Wallis test indicates that there are significant differences in the WDVI distributions. The dashed lines represent the standard deviations.

The WDVI profiles obtained from the STRS illustrate similar vegetation patterns as the fused imagery (Figure 22), reaching a maximum at the beginning of July. The regime with no initial fertilization has a WDVI significantly lower than the other plots after June 16th, the 90 kg N/ha regime became significantly different after June 29th, and the fertilization rate regime of 162 kg N/ha only deviated from the 252 kg N/ha on July 3rd. The Kruskal-Wallis test failed to reject the H_0 (α=0.01) after July 21st, indicating that the initial nitrogen fertilization regime no longer caused significantly different WDVI distributions after this time.

5.5.2 Yield prediction

A Kruskal-Wallis test indicated that the yield distributions of plots grouped by the four different fertilization regimes were significantly different from all other groups (n=2311 per group, $\alpha<0.01$). The results show that within the experimental plots, the 162 kg N/ha nitrogen application rate regime obtained the highest mean potato yield (Figure 23), with 77.41±8.56 ton/ha. This was closely followed by the 252 kg N/ha regime (73.48±7.55 ton/ha), and the regime with no initial fertilization received the lowest yield (64.60±9.22 ton/ha). Note that the yield of the experimental plots has excluded the tractor driving paths (i.e. no yield) from the yield averages.

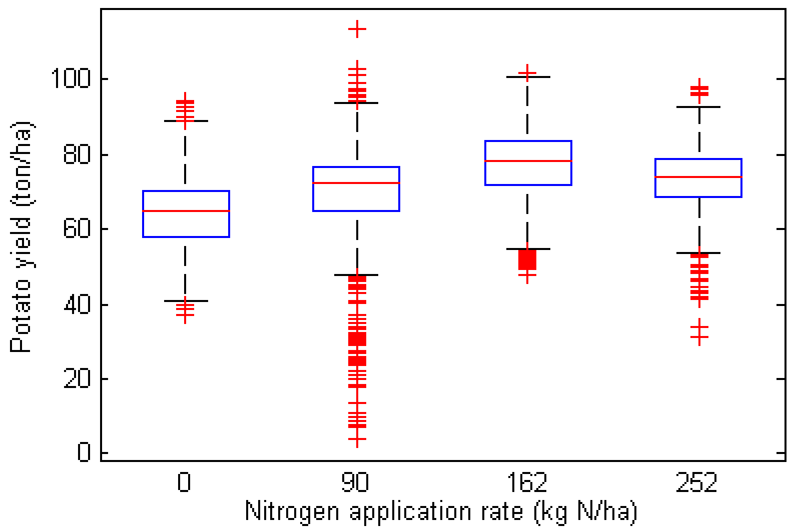

Figure 23: A boxplot depicting potato yield statistics grouped by fertilization regime. The horizontal red line represents the median, surrounded by a blue box presenting the 25th and 75th percentiles. The ends of the whiskers are the minimum and maximum values not considered outliers, which are marked with a red +.

Next, an attempt was made to determine how much of the yield variability can be described by GNDVI fluctuations obtained from the fused imagery during the growing season. Firstly, the correlation between the field data and the yield variability were defined (Table 4). The results indicate that the GNDVI is significantly correlated to the LAI (correlation coefficients of 0.550 to 0.633) between June 26th and July 18th. The canopy chlorophyll content (Chl) obtains the strongest correlations, above 0.72, at the end of the growing season (August 16th and 23rd). The GNDVI at field level obtains significant correlation coefficients between 0.431 and 0.462 between June 26th and July 18th and up to 0.634 on August 23rd.

Table 4: Correlation between parameters measured at field level and yield variability. All correlations significant at $\alpha<0.05$ are marked with * and significance at $\alpha<0.01$ are marked with ** (n=24).

Field data:	GNDVI	LAI	Chl
6-Jun	0.247	0.034	-0.422*
14-Jun	0.198	-0.01	0.394
21-Jun	0.186	0.254	0.081
26-Jun	**0.477***	**0.633****	0.211
5-Jul	**0.431***	**0.550****	0.077

Field data:	GNDVI	LAI	Chl
12-Jul	**0.436***	**0.580****	-0.203
18-Jul	**0.462***	**0.612****	-0.173
26-Jul	0.335	0.182	-0.098
31-Jul	**0.430***	0.194	0.097
16-Aug	**0.575****	0.058	**0.798****
23-Aug	**0.634****	0.399	**0.721****

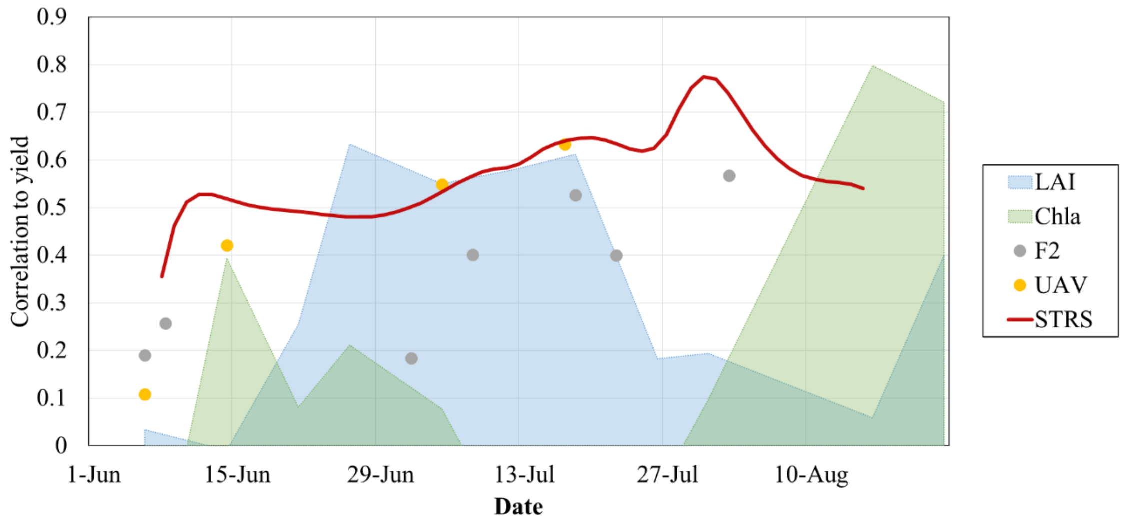

Figure 24: Temporal variation of the correlation between vegetation indices at certain dates and the yield.

The correlation coefficients between the WDVI obtained from the STRS surface and the yield are presented in Figure 24. The STRS obtains a higher correlation to yield than the Formosat-2 imagery, fused imagery, and canopy chlorophyll measurements throughout the growing season. Only the LAI on June 26th obtains a markedly higher correlation to the yield than the STRS data.

Next, a stepwise multivariate regression was applied to the three images series (fused images, Formosat-2 imagery and UAV imagery) and STRS separately. Table 5 displays the correlation between each of the imagery input parameters and yield. The table presents a number of interesting patterns:

1) The single image GNDVI of July 18th (or 17th for the UAV) had a significant correlation to yield for all three image series. Other days showing significant correlations to yield are July 8th (fused image series), August 2nd (Formosat-2 image series), June 14th and July 2nd (UAV image series).
2) The GNDVI obtained from a single image obtains stronger correlations to yield variability than the integrated GNDVI. This pattern is repeated for all three image series.
3) The correlation values between GNDVI and yield obtained from fused imagery and original Formosat-2 imagery are comparable.
4) The total Euclidean distance of the GNDVI per plot to the GNDVI of the plot with the highest yield had the highest correlation with the yield for each image series. However, this parameter can only be determined at the end of the season, as the plot with the highest yield must be known in order to calculate this parameter.

Table 5: Correlations between each input variable of the multivariate analysis and the yield. All correlations significant at α<0.05 are marked with * and significance at α<0.01 are marked with ** (n=24).

Factor		UM	Formosat-2		UAV
Single image GNDVI	24-Apr	0.353	0.253		
	6-Jun	0.022	0.19	6-Jun	0.108
	8-Jun	-0.091	0.257	14-Jun	0.421*
	2-Jul	0.141	0.184	5-Jul	0.549**
	8-Jul	0.534**	0.401		
	18-Jul	0.564**	0.526**	17-Jul	0.633**
	22-Jul	0.381	0.399		
	2-Aug	0.326	0.567**		
Integrated GNDVI	24-Apr	0.353	0.253		
	6-Jun	0.214	0.267	6-Jun	0.108
	8-Jun	0.204	0.269	14-Jun	0.159
	2-Jul	0.231	0.347	5-Jul	0.426*
	8-Jul	0.317	0.364		
	18-Jul	0.442*	0.413*	17-Jul	0.569**
	22-Jul	0.458*	0.427*		
	2-Aug	0.456*	0.459*		
$d_{euclidean}$		-0.590**	-0.708**		-0.651**

Table 6 displays two regression models for each of the three image series. The Models 3-6 utilizes all input parameters listed in Table 5 above for each dataset (unmixing-based, Formosat-2, UAV, and STRS respectively). The UAV imagery obtained the lowest correlation in this case. Models 7-10 exclude the total Euclidean distance parameter from the analysis.

A multivariate regression utilizing the field data of LAI and chlorophyll measurements explained 75.3% of yield variability. The two input parameters were the LAI in the mid-season (July 18th) and the chlorophyll concentration at the end of season (August 16th). A multivariate regression utilizing the GNDVI and total Euclidean distance parameter for the field GNDVI explained 76.3% of the yield variability.

Models 3-5 use all the parameters listed in Table 5 for each dataset (unmixing-based, Formosat-2, and UAV) as input parameters. Model 4, based on Formosat-2 imagery, explained the highest amount of yield variability (62.7%) and the UAV imagery explained the least amount of variability (42.4%). Model 6 used the STRS datasets as input, and explained 72.9% of yield variability, which is very close to the amount of yield variability explained by field measurements (Models 1 & 2).

When excluding the total Euclidean distance from the analysis (Models 7-10), only one explanatory parameter was selected for each of the three image series. When utilizing a single image to explain the yield variability, the UAV GNDVI explains more yield variability (40.1%) than the unmixing-based

(31.8%) and Formosat-2 (32.2%) imagery. The STRS explained even more yield variability (47.3%), using the formula of Model 10.

The regression models without the Euclidean distance (Models 7-10) utilized the STRS WDVI on July 20th as an input parameter (Model 10), similar to the selection of the GNDVI on July 18th by the fused imagery (Model 7), July 17th by the UAV imagery (Model 9), and the LAI on July 18th (Model 1) by the field data regressions.

Table 6: Regression models of potato yield based on input image series. For each series, two models are given, the first including all the input parameters listed in Table 5, the second excluding the total Euclidean distance parameter (d) from the regression. Pearson's correlation coefficient (r), the coefficient of determination (R^2) and the standard error (SE) are given for each model.

Model No.	**Input data**	**Formula**	**r**	R^2	**SE** (ton/ha)
		Stepwise regression models using reference field data			
1	**LAI and Chl**	$yield = 2.5 * LAI_{Jul-18} + 1.7 * MSPAD_{Aug-16} - 9.4$	0.868	0.753	3.66
2	**Field GNDVI**	$yield = 112.6 * GNDVI_{Jul-12} + 198.9 * GNDVI_{Aug-23} - 149.43$	0.874	0.763	3.59
		Stepwise regression models using all input parameters			
3	**UM**	$yield = 696.0 * GNDVI_{Apr-24} - 808.7 * d - 202.5$	0.726	0.527	4.99
4	**Formosat-2**	$yield = 363.7 * GNDVI_{Apr-24} - 102.8 * d - 63.3$	0.812	0.627	4.23
5	**UAV**	$yield = -78.8 * d + 79.1$	0.651	0.424	5.38
6	**STRS**	$yield = -5.88 * WDVI_{July-09\ int} - 6.40 * d + 148.7$	0.854	0.729	3.78
		Stepwise regression models excluding the Euclidean distance parameters			
7	**UM**	$yield = 234.4 * GNDVI_{Jul-18} - 70.5$	0.564	0.318	5.85
8	**Formosat-2**	$yield = 279.8 * GNDVI_{Aug-2} - 82.9$	0.567	0.322	5.84
9	**UAV**	$yield = 155.3 * GNDVI_{Jul-17} - 38.0$	0.633	0.401	5.48
10	**STRS**	$yield = 103.0 * WDVI_{Jul-20} + 23.0$	0.688	0.473	5.14

The results of the Kruskal-Wallis test indicate that plots under an initial fertilization rate of 162 kg N/ha obtained significantly higher yields than those under both 90 and 252 kg N/ha. This suggests that the relation between the biophysical parameters and yield should be quadratic rather than linear. However, when a quadratic stepwise regression (including the squared GNDVI values of each date as input independent parameters) was applied in SPSS, the same models presented in Table 6 above were produced. That is to say that a quadratic regression did not produce better results than the linear regressions.

6 Discussion

6.1 Combination of multi-sensor imagery

The current study made use of two data fusion algorithms: the STARFM method (Gao et al. 2006) and an unmixing-based method (Zurita-Milla 2008; Gevaert 2013). Both fusion algorithms were originally designed to be applied to Landsat and MODIS imagery. In the current scenario, there were three main differences which had to be taken into account, compared with the conventional application of these algorithms: (1) radiometric normalization to calibrate surface reflectance from different sensors, (2) the assumption of homogenous temporal variations within a spectral cluster, and (3) hyperspectral vs. multispectral imagery.

Regarding the first point, the quality of the radiometric normalization in the current application is limited due to: (1) the extent of the UAV imagery which limits the number of homogenous Formosat-2 pixels available, (2) inconsistency of Formosat-2 atmospheric correction methods (Appendix 1), and (3) the restricted availability of UAV and Formosat-2 imagery on corresponding dates (only on June 6th and July 17th/18th. In future applications, it would be useful to fly the UAV over large homogenous spectral surfaces (preferably one light, one dark and both having temporally stable surface reflectance) when the other imagery is being obtained. This would allow for an empirical line correction using these spectra to atmospherically correct the satellite imagery and greatly reduce the spectral differences and WDVI differences between the Formosat-2 and UAV imagery.

A second important issue when applying data fusion to the current application is the assumption of both data fusion algorithms that pixels which are spectrally similar on a base date will also be spectrally similar on the prediction date. This is the main reason for the differing quality of the fused imagery on July 8th (Figures 13 and 14): the STARFM algorithm utilized the UAV image on June 6th to define spectrally similar pixels whereas the unmixing-based method utilized the UAV image on July 5th. In the June 6th image, no differences between nitrogen application regimes was visible, so the STARFM algorithm 'assumes' that there will also be no differences on July 8th. The unmixing-based algorithm obtains better predictions for July 8th by using the UAV image of July 5th to select spectrally similar pixels.

Thirdly, the medium-resolution imagery (MODIS/MERIS) contained more spectral bands than the high-resolution imagery (Landsat) in previous applications of these data fusion algorithms. This was an additional benefit of the unmixing-based algorithm as it served to down-scale the additional spectral information. However, in this study, the high spatial-resolution imagery (UAV) contains more spectral bands than the medium spatial-resolution Formosat-2 imagery.

To make full use of the hyperspectral information in the UAV imagery, STRS can be utilized. The STRS based on a novel Bayesian method more accurately the actual spectral characteristics and temporal variations documented by field data than two more simplistic methods (Figure 18). Correlations between WDVI calculated from STRS and field data was similar for all three STRS methods. However the MCARI obtained from the Bayesian-based STRS had a higher correlation to field data than the other two methods (Table 4). This is likely due to the fact that the WDVI is based on surface reflectance at 670 nm and 800 nm – both of which fall within the Formosat-2 spectral bands. The MCARI, however, also utilizes surface reflectance data at 700 nm, which is not present in Formosat-2 imagery (Table 1).

Although vegetation indices calculated from the STRS showed high correlations to field measurements throughout the growing season, it is important to remember that it is always an interpolation. This is especially important for larger temporal intervals without observations, such as the lack of satellite data between June 8th and July 2nd. Such limitations may be partially alleviated by introducing other satellite imagery into the STRS. The only additional parameters needed would be the satellite images themselves and the spectral response functions of the sensors.

6.2 Vegetation indices

Comar et al. (2012) indicated that vegetation indices are highly correlated. This was also the case in the current study. All vegetation indices (with the notable exception of the EVI) achieved a Spearman's correlation with the fused imagery of between 0.859 and 0.899 with LAI and between 0.726 and 0.819 with canopy chlorophyll (Figure 19); this was r_s=0.680-0.858 and r_s=0.580-0.788 respectively for the STRS surface (Figure 20). As most vegetation indices have similar correlations to reference field data, future applications could select a vegetation index based on *a priori* information (Broge and Leblanc 2001; Haboudane et al. 2004; Zarco-Tejada et al. 2005; Clevers and Kooistra 2012) rather than performing extensive studies to determine the optimal index in that particular application.

Although the vegetation indices obtained from imagery show a high correlation to the field data, there were absolute differences between the indices obtained from different datasets. The UAV GNDVI values were slightly lower field GNDVI, but the Formosat-2 GNDVI was substantially lower than UAV and field GNDVI. An attempt to explain this difference indicated that the difference in NIR surface reflectance of UAV vs. Formosat-2 imagery is larger than the surface reflectance differences in the green region. This may be due to differences in the spectral bands or the atmospheric correction method employed for the Formosat-2 imagery. Improved radiometric normalization (as discussed above) may make spectral reflectance and derivatives thereof (such as vegetation indices) more comparable.

Furthermore, the vegetation index differences between the image datasets and the field measurements are due to how the field measurements were taken. The Cropscan multispectral radiometer was directed at the green vegetation of potato crops. Therefore, there was very little soil background to influence these spectra and no negative WDVI values (Figure 15). UAV and Formosat-2 imagery are influenced by the soil background and can therefore obtain negative WDVI values when the potato plants are still small.

6.3 Fused datasets for in-season crop status analysis and yield prediction

One of the objectives of the current study was to analyze the ability of using fused datasets to identify yield variation during the growing season. The results indicate that as of June 8th, different initial fertilization regimes caused significant differences in the GNDVI, where the higher the initial fertilization, the higher the GNDVI (Figure 24). The STRS first detected significantly different WDVI distributions between July 3rd and July 21st. These difference may be due to the number of samples used for each of the methods: 48 per plot in the fused imagery, and 1 per plot for the STRS.

In the current application, no Formosat-2 imagery was available between June 8th and July 2nd, or after August 2nd. The STRS interpolated the spectra for these dates, but the large lapse between images (24 days) makes the predictions more uncertain. This stage in the potato growth cycle could be important for precision farming management, as field data indicated that biophysical parameters had significant correlations to field variation at the end of June and during the month of August (Table 4). The problem of obtaining satellite imagery in cloudy locations has often been mentioned as a hindrance for precision farming applications (Zhang and Kovacs 2012), and can be partially overcome by utilizing multiple sensory platforms as in the current study. In future scenarios, alternative platforms such as UAVs could replace satellite imagery on cloudy days, or imagery from additional satellites could be incorporated into the STRS.

6.4 Yield prediction

Yield prediction based on remotely sensed biophysical parameters is difficult in the current situation, as potato tubers are grown below-ground. Therefore, the first two regression models were based on field data, to give an indication of the maximum yield model quality in the current application, which was R^2=0.763. The results of the regression analyses indicated that the GNDVI of Formosat-2 imagery (R^2=0.322) had a slightly higher correlation to the yield than the GNDVI of individual images of the fused time series (R^2=0.318). This is logical because the additional data manipulation inferred by the fusion implies the introduction of more uncertainty to the processing chain. As the correlations to yield are measured at experimental plot level, the added value of the enhanced spatial resolution of the fused imagery is not exploited.

Regression models obtained from the UAV imagery, in turn, obtained the highest correlation to yield when using only single-date GNDVI input (R^2=0.424). However, when adding seasonal input parameters to the multivariate regression, such as the total Euclidean distance to the GNDVI of the plot with the highest yield, the UAV obtained lower correlations than the other datasets. This is most likely due to the limited temporal extent of the UAV series (June 6th – July 17th) compared to the Formosat-2 and fused image series (April 24th – August 2nd). The regression model obtained from the STRS (R^2=0.729) explained almost as much of the yield variation as the LAI and canopy chlorophyll measurements at field level (R^2=0.753). The better performance of the STRS regression models than the models based on fused, UAV and Formosat-2 imagery could be due to the increased temporal resolution of the dataset or the differing number of sample points in the regression analysis.

Although the coefficients of the regression models are restricted to the scope of the current study, the parameters included in the stepwise regression are important. For example, the stepwise multivariate regression models utilized few input parameters even though the GNDVI had significant correlations to yield variability on various dates. This suggests that the GNDVI high a covariance between dates. Furthermore, the unmixing-based, UAV, and STRS regression models defined the vegetation indices at July 18th, 17th, and 20th respectively as the date with the highest correlation to yield. This could indicate that crop status around 80-90 days after planting plays an important role in potato yield; information which could be useful for future potato growth studies.

Furthermore, it is important to note that all regression models presented here were able to predict the yield to a RMSE of between 3.59 and 5.85 ton/ha. This is much lower than the RMSE of the yield interpolation through EBK was 8.05 ton/ha. Improved yield data collection methods could improve the quality of the regression models.

7 Conclusions

The aim of the current research was to develop methods to combine imagery from multiple platforms in order to meet the data requirements of precision agriculture applications. Two data fusion methods were analyzed to provide high spatial-resolution information regarding crop status more often during the growing season. The unmixing-based fusion method provided higher correlations to reference LAI and chlorophyll levels measured at field level than the STARFM method. This implies that the unmixing-based fusion method provides more stable predictions of crop status, and is more suited to in-season crop monitoring than the STARFM method.

STRS methods were developed using a novel Bayesian methodology, which provided daily hyperspectral crop spectra for a number of experimental plots. The STRS displayed a high correlation to the reference LAI and chlorophyll measurements. Yield prediction models based on the STRS achieved almost the same accuracy as yield prediction models based on direct LAI and chlorophyll measurements during the growing season. Therefore, the STRS method developed here can accurately describe crop status variability at high spectral and temporal resolutions. This method may also be useful for many other applications which require continuous surface reflectance information.

The methods proposed in this study showed sufficiency in meeting the stringent data requirements of precision agriculture. Integrating various image sources along the spatial-temporal domains (data fusion) and spectral-temporal domains (STRS) is an important step towards surpassing physical limitations of sensors to meet precision agricultural needs. A combination of data fusion and STRS has the potential to provide daily hyperspectral reflectance at a spatial resolution of 1 m.

With the abundance of availability of satellite and UAV sensors, these methods utilizing the spatial and temporal resolutions from multiple sensors can provide more accurate information on crop status.This information on crop status variability could then be used to optimize nitrogen fertilization application rates, thus reducing the economic costs for the farmers at a local level and impacts on the balance of ecosystem at a regional level, and serving as a sustainable agriculture intensification method to safeguard food security at a global level.

8 References

Amorós-López, J., L. Gómez-Chova, L. Alonso, L. Guanter, R. Zurita-Milla, J. Moreno, and G. Camps-Valls. 2013. Multitemporal fusion of Landsat/TM and ENVISAT/MERIS for crop monitoring. *International Journal of Applied Earth Observation and Geoinformation* 23. Elsevier B.V. 132–141. doi:10.1016/j.jag.2012.12.004.

Anderson, M. C., W. P. Kustas, J. M. Norman, C. R. Hain, J. R. Mecikalski, L. Schultz, M. P. González-Dugo, C. Cammalleri, et al. 2011. Mapping daily evapotranspiration at field to continental scales using geostationary and polar orbiting satellite imagery. *Hydrology and Earth System Sciences* 15: 223–239. doi:10.5194/hess-15-223-2011.

Arai, E., Y. E. Shimabukuro, G. Pereira, and N. L. Vijaykumar. 2011. Remote Sensing. *Remote Sensing* 3: 1943–1956. doi:10.3390/rs3091943.

Bala, S. K., and a. S. Islam. 2009. Correlation between potato yield and MODIS-derived vegetation indices. *International Journal of Remote Sensing* 30: 2491–2507. doi:10.1080/01431160802552744.

Baret, F., G. Guyot, and D. J. Major. 1989. Crop biomass evaluation using radiometric measurements. *Photogrammetria* 43: 241–256. doi:10.1016/0031-8663(89)90001-X.

Barnes, E. M., T. R. Clarke, S. E. Richards, P. D. Colaizzi, J. Haberland, M. Kostrezewski, P. Waller, C. Choi, et al. 2000. Coincident detection of crop water stress, nitrogen status and canopy density using ground-based multispectral data. In *Proceedings of the Fifth International Conference on Precision Agriculture*, 15. Bloomington, USA.

Berni, J. A. J., S. Member, P. J. Zarco-tejada, L. Suárez, and E. Fereres. 2009. Thermal and Narrowband Multispectral Remote Sensing for Vegetation Monitoring From an Unmanned Aerial Vehicle. *IEEE Transactions on Geoscience and Remote Sensing* 47: 722–738. doi:10.1109/TGRS.2008.2010457.

Bernstein, L. S., X. Jin, B. Gregor, and S. M. Adler-Golden. 2012. Quick atmospheric correction code: algorithm description and recent upgrades. *SPIE Optical Engineering* 51: 111719. doi:10.1117/1.OE.51.11.111719.

Bhandari, S., S. Phinn, and T. Gill. 2012. Preparing Landsat Image Time Series (LITS) for Monitoring Changes in Vegetation Phenology in Queensland, Australia. *Remote Sensing* 4: 1856–1886. doi:10.3390/rs4061856.

Bioucas-Dias, J. M., A. Plaza, N. Dobigeon, M. Parente, Q. Du, S. Member, P. Gader, and J. Chanussot. 2012. Hyperspectral Unmixing Overview : Geometrical , Statistical , and Sparse Regression-Based Approaches. *IEEE Journal of Selected Topics in Applied Earth Observations and Remote Sensing* 5: 354–379. doi:10.1109/JSTARS.2012.2194696.

Broge, N. ., and E. Leblanc. 2001. Comparing prediction power and stability of broadband and hyperspectral vegetation indices for estimation of green leaf area index and canopy chlorophyll density. *Remote Sensing of Environment* 76: 156–172. doi:10.1016/S0034-4257(00)00197-8.

Buishand, T. A., and C. A. Velds. 2010. Neerslag en Verdamping. In *Klimaat van Nederland*, 203. De Bilt: KNMI.

CBS. 2011. *Bodemgebruik Nederland*. Den Haag.

Chavez, P. S. J. 1988. An improved dark-object subtraction technique for atmospheric scattering correction of multispectral data. *Remote Sensing of Environment* 24: 459–479. doi:10.1016/0034-4257(88)90019-3.

Christophe, E., D. Leger, and C. Mailhes. 2005. Quality criteria benchmark for hyperspectral imagery. *IEEE Transactions on Geoscience and Remote Sensing* 43: 2103–2114. doi:10.1109/TGRS.2005.853931.

Clay, D. E., and J. F. Shanahan. 2011. *GIS Applications in Agriculture. Volume Two: Nutrient Management for Energy Efficiency*. Edited by Francis J. Pierce. Boca Raton: CRC Press.

Clevers, J. G. P. W. 1989. Application of a weighted infrared-red vegetation index for estimating leaf Area Index by Correcting for Soil Moisture. *Remote Sensing of Environment* 29: 25–37. doi:10.1016/0034-4257(89)90076-X.

Clevers, J. G. P. W., and L. Kooistra. 2012. Using Hyperspectral Remote Sensing Data for Retrieving Canopy Chlorophyll and Nitrogen Content. *IEEE Journal of Selected Topics in Applied Earth Observations and Remote Sensing* 5: 574–583. doi:10.1109/JSTARS.2011.2176468.

Clevers, J. G. P. W., and W. Verhoef. 1993. LAI estimation by means of the WDVI: A sensitivity analysis with a combined PROSPECT-SAIL model. *Remote Sensing Reviews* 7: 43–64. doi:10.1080/02757259309532165.

Cohen, Y., V. Alchanatis, Y. Zusman, Z. Dar, D. J. Bonfil, A. Karnieli, A. Zilberman, A. Moulin, et al. 2010. Leaf nitrogen estimation in potato based on spectral data and on simulated bands of the VENµS satellite. *Precision Agriculture* 11: 520–537. doi:10.1007/s11119-009-9147-8.

Comar, A., P. Burger, B. De Solan, F. Baret, F. Daumard, and J.-F. Hanocq. 2012. A semi-automatic system for high throughput phenotyping wheat cultivars in-field conditions : description and first results. *Functional Plant Biology* 39: 914–924. doi:10.1071/FP12065.

Dai, X., Z. Huo, and H. Wang. 2011. Simulation for response of crop yield to soil moisture and salinity with artificial neural network. *Field Crops Research* 121: 441–449. doi:10.1016/j.fcr.2011.01.016.

Daughtry, C., C. L. Walthall, M. S. Kim, E. Brown de Colstoun, and J. E. I. McMurtrey. 2000. Estimating Corn Leaf Chlorophyll Concentration from Leaf and Canopy Reflectance. *Remote Sensing of Environment* 74: 229–239. doi:10.1016/S0034-4257(00)00113-9.

Diacono, M., P. Rubino, and F. Montemurro. 2012. Precision nitrogen management of wheat. A review. *Agronomy for Sustainable Development* 33: 219–241. doi:10.1007/s13593-012-0111-z.

Dorigo, W. A., R. Zurita-Milla, A. J. W. de Wit, J. Brazile, R. Singh, and M. E. Schaepman. 2007. A review on reflective remote sensing and data assimilation techniques for enhanced agroecosystem modeling. *International Journal of Applied Earth Observation and Geoinformation* 9: 165–193. doi:10.1016/j.jag.2006.05.003.

Emelyanova, I. V, T. R. Mcvicar, T. G. Van Niel, L. T. Li, and A. I. J. M. Van Dijk. 2012. *On blending Landsat-MODIS surface reflectances in two landscapes with contrasting spectral , spatial and temporal dynamics*. Flagship, Australia.

Emelyanova, I. V, T. R. McVicar, T. G. Van Niel, L. Tao Li, and A. I. J. M. Van Dijk. 2013. Remote Sensing of Environment Assessing the accuracy of blending Landsat – MODIS surface re fl ectances in two landscapes with contrasting spatial and temporal dynamics : A framework for algorithm selection. *Remote Sensing of Environment* 133: 193–209. doi:10.1016/j.rse.2013.02.007.

Van Evert, F. K., R. Booij, J. N. Jukema, H. F. M. ten Berge, D. Uenk, E. J. J. (Bert) Meurs, W. C. a. van Geel, K. H. Wijnholds, et al. 2012. Using crop reflectance to determine sidedress N rate in potato saves N and maintains yield. *European Journal of Agronomy* 43. Elsevier B.V. 58–67. doi:10.1016/j.eja.2012.05.005.

Fasbender, D., J. Radoux, and P. Bogaert. 2008. Bayesian Data Fusion for Adaptable Image Pansharpening. *IEEE Transactions on Geoscience and Remote Sensing* 46: 1847–1857. doi:10.1109/TGRS.2008.917131.

Felde, G. W., G. P. Anderson, T. W. Cooley, M. W. Matthew, S. M. Adler-Golden, A. Berk, and J. Lee. 2003. Analysis of Hyperion data with the FLAASH atmospheric correction algorithm. In *IGARSS 2003. 2003 IEEE International Geoscience and Remote Sensing Symposium. Proceedings (IEEE Cat. No.03CH37477)*, 1:90–92. IEEE. doi:10.1109/IGARSS.2003.1293688.

Feng, M., J. O. Sexton, C. Huang, J. G. Masek, E. F. Vermote, F. Gao, R. Narasimhan, S. Channan, et al. 2013. Global surface reflectance products from Landsat: Assessment using coincident MODIS observations. *Remote Sensing of Environment* 134. Elsevier Inc. 276–293. doi:10.1016/j.rse.2013.02.031.

Fidell, B., and L. S. Tabachnik. 2012. *Using Multivariate Statistics*. 6th ed. Boston: Pearson.

Fortin, J. G., F. Anctil, L.-É. Parent, and M. a. Bolinder. 2011. Site-specific early season potato yield forecast by neural network in Eastern Canada. *Precision Agriculture* 12: 905–923. doi:10.1007/s11119-011-9233-6.

Gamon, J. A., L. Serrano, and J. S. Surfus. 1997. The photochemical reflectance index: an optical indicator of photosynthetic radiation use efficiency across species, functional types, and nutrient levels. *Oecologia* 112: 492–501. doi:10.1007/s004420050337.

Gao, F., J. Masek, M. Schwaller, and F. Hall. 2006. On the blending of the Landsat and MODIS surface reflectance: predicting daily Landsat surface reflectance. *IEEE Transactions on Geoscience and Remote Sensing* 44: 2207–2218. doi:10.1109/TGRS.2006.872081.

Gao, F., M. C. Anderson, W. P. Kustas, and Y. Wang. 2012. Simple method for retrieving leaf area index from Landsat using MODIS leaf area index products as reference. *Journal of Applied Remote Sensing* 6: 063554. doi:10.1117/1.JRS.6.063554.

García-Haro, F. J., S. Sommer, and T. Kemper. 2005. A new tool for variable multiple endmember spectral mixture analysis (VMESMA). *International Journal of Remote Sensing* 26: 2135–2162. doi:10.1080/01431160512331337817.

Ge, Y., J. A. Thomasson, and R. Sui. 2011. Remote sensing of soil properties in precision agriculture: A review. *Frontiers of Earth Science* 5: 229–238. doi:10.1007/s11707-011-0175-0.

Gebbers, R., and V. I. Adamchuk. 2010. Precision agriculture and food security. *Science (New York, N.Y.)* 327: 828–31. doi:10.1126/science.1183899.

Gevaert, C. 2013. High- and medium-resolution satellite data fusion: an application using Landsat/TM and MODIS/EOS. Universidad de Valencia.

Gevaert, C. M., and F. J. García-Haro. 2014. A Comparison of STARFM and an Unmixing-based Algorithm for Landsat and MODIS Data Fusion.

Gilabert, M. A., J. González-Piqueras, and B. Martinez. 2010. Theory and applications of vegetation indices. In *Remote Sensing Optical Observations of Vegetation Properties*, ed. F. Maselli, M. Menenti, and P. A. Brivo, 1–43. Kerala, India: Research Signpost.

Gitelson, A. A., M. N. Merzlyak, and H. K. Lichtenthaler. 1996. Detection of Red Edge Position and Chlorophyll Content by Reflectance Measurements Near 700 nm. *Journal of Plant Physiology* 148: 501–508. doi:10.1016/S0176-1617(96)80285-9.

Godfray, H. C. J., J. R. Beddington, I. R. Crute, L. Haddad, D. Lawrence, J. F. Muir, J. Pretty, S. Robinson, et al. 2010. Food security: the challenge of feeding 9 billion people. *Science (New York, N.Y.)* 327: 812–8. doi:10.1126/science.1185383.

Goffart, J. P., M. Olivier, and M. Frankinet. 2008. Potato Crop Nitrogen Status Assessment to Improve N Fertilization Management and Efficiency: Past–Present–Future. *Potato Research* 51: 355–383. doi:10.1007/s11540-008-9118-x.

Gontia, N. K., and K. N. Tiwari. 2011. Yield Estimation Model and Water Productivity of Wheat Crop (Triticum aestivum) in an Irrigation Command Using Remote Sensing and GIS. *Journal of the Indian Society of Remote Sensing* 39: 27–37. doi:10.1007/s12524-011-0065-7.

Govaerts, Y. M., M. M. Verstraete, B. Pinty, and N. Gobron. 1999. Designing optimal spectral indices: A feasibility and proof of concept study. *International Journal of Remote Sensing* 20: 1853–1873. doi:10.1080/014311699212524.

Haboudane, D., J. R. Miller, N. Tremblay, P. J. Zarco-Tejada, and L. Dextraze. 2002. Integrated narrow-band vegetation indices for prediction of crop chlorophyll content for application to precision agriculture. *Remote Sensing of Environment* 81: 416–426. doi:10.1016/S0034-4257(02)00018-4.

Haboudane, D., J. R. Miller, E. Pattey, P. J. Zarco-Tejada, and I. B. Strachan. 2004. Hyperspectral vegetation indices and novel algorithms for predicting green LAI of crop canopies: Modeling and validation in the context of precision agriculture. *Remote Sensing of Environment* 90: 337–352. doi:10.1016/j.rse.2003.12.013.

Hayes, M. J., and W. L. Decker. 1996. Using NOAA AVHRR data to estimate maize production in the United States Corn Belt. *International Journal of Remote Sensing* 17: 3189–3200. doi:10.1080/01431169608949138.

Hilker, T., M. a. Wulder, N. C. Coops, J. Linke, G. McDermid, J. G. Masek, F. Gao, and J. C. White. 2009. A new data fusion model for high spatial- and temporal-resolution mapping of forest disturbance based on Landsat and MODIS. *Remote Sensing of Environment* 113. Elsevier Inc. 1613–1627. doi:10.1016/j.rse.2009.03.007.

Huete, A. . 1988. A soil-adjusted vegetation index (SAVI). *Remote Sensing of Environment* 25: 295–309. doi:10.1016/0034-4257(88)90106-X.

Hwang, T., C. Song, P. V. Bolstad, and L. E. Band. 2011. Downscaling real-time vegetation dynamics by fusing multi-temporal MODIS and Landsat NDVI in topographically complex terrain. *Remote Sensing of Environment* 115: 2499–2512. doi:10.1016/j.rse.2011.05.010.

Jones, H. G., and R. A. Vaughan. 2010. *Remote Sensing of Vegetation: Principles, Techniques and Applications*. New York: Oxford University Press.

Karpouzli, E., and T. Malthus. 2003. The empirical line method for the atmospheric correction of IKONOS imagery. *International Journal of Remote Sensing* 24: 1143–1150. doi:10.1080/0143116021000026779.

Kerr, J. T., and M. Ostrovsky. 2003. From space to species: ecological applications for remote sensing. *Trends in Ecology & Evolution* 18: 299–305. doi:10.1016/S0169-5347(03)00071-5.

KNMI. 2014. Dagggevens van het weer in Nederland - Station #307 Eindhoven. De Bilt.

Kooistra, L., E. Beza, J. Verbesselt, J. van den Borne, W. van der Velde, and J. Van Den Borne. 2012. Integrating remote- , close range- and in-situ sensing for high- frequency observation of crop status to support precision agriculture. In *Sensing a Changing World II*, 1–7. Wageningen, the Netherlands.

Kooistra, L., J. Suomalainen, S. Iqbal, J. Franke, P. Wenting, and H. Bartholomeus. 2013. Crop monitoring using a light-weight hyperspectral mapping system for unmanned aerial vehicles : first results for the 2013 season. In *Workshop on UAV-based Remote Sensing Methods for Monitoring Vegetation*, 1–7. Cologne, Germany: University of Cologne.

Krivoruchko, K. 2011. *Spatial Statistical Data Analysis for GIS Users*. 1st ed. London: Esri Press.

Krivoruchko, K., and A. Gribov. 2014. Pragmatic Bayesian Kriging for Non-Stationary and Moderately Non-Gaussian Data. In *Mathematics of Planet Earth*, ed. E. Pardo-Igúzquiza, C. Guardiola-Albert, J. Heredia, L. Moreno-Merino, J. J. Durán, and J. A. Vargas-Guzmán, 61–64. Lecture Notes in Earth System Sciences. Berlin, Heidelberg: Springer Berlin Heidelberg. doi:10.1007/978-3-642-32408-6.

Lee, W. S., V. Alchanatis, C. Yang, M. Hirafuji, D. Moshou, and C. Li. 2010. Sensing technologies for precision specialty crop production. *Computers and Electronics in Agriculture* 74: 2–33. doi:10.1016/j.compag.2010.08.005.

Lillo-Saavedra, M., C. Gonzalo, A. Arquero, and E. Martinez. 2005. Fusion of multispectral and panchromatic satellite sensor imagery based on tailored filtering in the Fourier domain. *International Journal of Remote Sensing* 26: 1263–1268. doi:10.1080/01431160412331330239.

Liu, C. C., A. Kamei, K.-H. Hsu, S. Tsuchida, H.-M. Huang, S. Kato, R. Nakamura, and A.-M. Wu. 2010. Vicarious Calibration of the Formosat-2 Remote Sensing Instrument. *IEEE Transactions on Geoscience and Remote Sensing* 48: 2162–2169. doi:10.1109/TGRS.2009.2033179.

Liu, C.-C. 2006. Processing of FORMOSAT-2 Daily Revisit Imagery for Site Surveillance. *IEEE Transactions on Geoscience and Remote Sensing* 44: 3206–3214. doi:10.1109/TGRS.2006.880625.

Liu, H., and Q. Weng. 2012. Enhancing temporal resolution of satellite imagery for public health studies: A case study of West Nile Virus outbreak in Los Angeles in 2007. *Remote Sensing of Environment* 117. Elsevier B.V. 57–71. doi:10.1016/j.rse.2011.06.023.

Lunetta, R. S., J. G. Lyon, B. Guindon, and C. D. Elvidge. 1998. North American Landscape Characterization Dataset Development and Data Fusion Issues. *Photogrammetric Enginnering & Remote Sensing* 64: 821–829.

Lunetta, R. S., Y. Shao, J. Ediriwickrema, and J. G. Lyon. 2010. Monitoring agricultural cropping patterns across the Laurentian Great Lakes Basin using MODIS-NDVI data. *International Journal of Applied Earth Observation and Geoinformation* 12. Elsevier B.V. 81–88. doi:10.1016/j.jag.2009.11.005.

Manakos, I., and S. Lavender. 2014. Remote Sensing in Support of the Geo-information in Europe. In *Land Use and Land Cover Mapping in Europe*, 3–10. Springer Netherlands. doi:10.1007/978-94-007-7969-3_1.

Manakos, I., K. Manevski, C. Kalaitzidis, and D. Edler. 2011. Comparison Between FLAASH and ATCOR Atmospheric Correction Modules on the Basis of Worldview-2 Imagery and In Situ Spectroradiometric Measurements. In *EARSeL 7th SIG-Imaging Spectroscopy Workshop*, 11. Edinburgh: EARSeL.

Mcmurtrey, J. E., E. M. Middleton, L. A. Corp, P. K. E. Campbell, L. M. Butcher, and C. S. T. Daughtry. 2003. Optical Reflectance and Fluorescence for Detecting Nitrogen Needs in Zea mays L . In *Geoscience and Remote SEensing Symposium (IGARSS)*, 00:7929–7931. Toulouse, France: IEEE International.

Mello, M., C. Vieira, B. Rudorff, P. Aplin, R. Santos, and D. Aguiar. 2013. STARS: A New Method for Multitemporal Remote Sensing. *IEEE Transactions on Geoscience and Remote Sensing* 51: 1897–1913. doi:10.1109/TGRS.2012.2215332.

Merlin, O., B. Duchemin, O. Hagolle, F. Jacob, B. Coudert, G. Chehbouni, G. Dedieu, J. Garatuza, et al. 2010. Disaggregation of MODIS surface temperature over an agricultural area using a time series of Formosat-2 images. *Remote Sensing of Environment* 114: 2500–2512. doi:10.1016/j.rse.2010.05.025.

Mewes, T., J. Franke, and G. Menz. 2009. Data reduction of hyperspectral remote sensing data for crop stress detection using different band selection methods. In *2009 IEEE International Geoscience and Remote Sensing Symposium*, III–463–III–466. Cape Town: IEEE. doi:10.1109/IGARSS.2009.5418292.

Mulla, D. J. 2013. Twenty five years of remote sensing in precision agriculture: Key advances and remaining knowledge gaps. *Biosystems Engineering* 114. IAgrE: 358–371. doi:10.1016/j.biosystemseng.2012.08.009.

Murphy, K. 2012. *Machine learning: a probabilistic perspective*. Cambridge, Massachusetts, USA: MIT Press.

Myneni, R. B., F. G. Hall, P. J. Sellers, and A. L. Marshak. 1995. The interpretation of spectral vegetation indexes. *IEEE Transactions on Geoscience and Remote Sensing* 33: 481–486. doi:10.1109/36.377948.

Neale, C. M. U., and S. Sivarajan. 2011. Yield Estimation and Validation of Potatoes Using Remote Sensing based Crop Yield Model. In *Spring Runoff conference*. Logan, USA: Utah State University.

Osborne, S. L., J. S. Schepers, and M. R. Schlemmer. 2004. Detecting Nitrogen and Phosphorus Stress in Corn Using Multi-spectral Imagery. *Communications in Soil Science and Plant Analysis* 35: 505–516. doi:10.1081/CSS-120029728.

Persson, A., P. Pilesjö, and L. Eklundh. 2005. Spatial Influence of Topographical Factors on Yield of Potato (Solanum tuberosum L.) in Central Sweden. *Precision Agriculture* 6: 341–357. doi:10.1007/s11119-005-2323-6.

Pilz, J., and G. Spöck. 2008. Why do we need and how should we implement Bayesian kriging methods. *Stochastic Environmental Research and Risk Assessment* 22: 621–632. doi:10.1007/s00477-007-0165-7.

Plant, R. E. 2001. Site-specific management: the application of information technology to crop production. *Computers and Electronics in Agriculture* 30: 9–29. doi:10.1016/S0168-1699(00)00152-6.

Po, E. A., S. S. Snapp, and A. Kravchenko. 2010. Potato Yield Variability across the Landscape. *Agronomy Journal* 102: 885. doi:10.2134/agronj2009.0424.

Pohl, C., and J. L. Van Genderen. 1998. *Review article Multisensor image fusion in remote sensing: Concepts, methods and applications*. *International Journal of Remote Sensing*. Vol. 19. doi:10.1080/014311698215748.

Qi, J., A. Chehbouni, A. R. Huete, Y. H. Kerr, and S. Sorooshian. 1994. A modified soil adjusted vegetation index. *Remote Sensing of Environment* 48: 119–126. doi:10.1016/0034-4257(94)90134-1.

Rahman, A., K. Kahn, N. Y. Krakauer, L. Roytman, and F. Kogan. 2012. Using AVHRR-Based Vegetation Health Indices For Estimation Of Potato Yield In Bangladesh. *Journal of Civil & Environmental Engineering* 02. doi:10.4172/2165-784X.1000111.

Ramírez, D. a., W. Yactayo, R. Gutiérrez, V. Mares, F. De Mendiburu, a. Posadas, and R. Quiroz. 2014. Chlorophyll concentration in leaves is an indicator of potato tuber yield in water-shortage conditions. *Scientia Horticulturae* 168. Elsevier B.V. 202–209. doi:10.1016/j.scienta.2014.01.036.

Rembold, F., C. Atzberger, I. Savin, and O. Rojas. 2013. Using Low Resolution Satellite Imagery for Yield Prediction and Yield Anomaly Detection. *Remote Sensing* 5: 1704–1733. doi:10.3390/rs5041704.

Rodrigues, A. S., A. R. S. Marçal, and M. Cunha. 2009. Evaluation of data fusion methods for agricultural monitoring based on synthetic images. In *Remote Sensing for a Changing Europe: Proceedings of the 28th Symposium of the European Association of Remote Sensing Laboratories*, ed. D. Maktav, 125–133. Istanbul, Turkey: IOS Press. doi:10.3233/978-1-58603-986-8-125.

Rudorff, B. F. T., and G. T. Batista. 1990. Spectral response of wheat and its relationship to agronomic variables in the tropical region. *Remote Sensing of Environment* 31: 53–63. doi:10.1016/0034-4257(90)90076-X.

Schroeder, T. a., W. B. Cohen, C. Song, M. J. Canty, and Z. Yang. 2006. Radiometric correction of multi-temporal Landsat data for characterization of early successional forest patterns in western Oregon. *Remote Sensing of Environment* 103: 16–26. doi:10.1016/j.rse.2006.03.008.

Sheskin, D. J. 2003. *Handbook of Parametric and Nonparametric Statistical Procedures*. 3rd Editio. Chapman and Hall/CRC.

Shillito, R. M., D. J. Timlin, D. Fleisher, V. R. Reddy, and B. Quebedeaux. 2009. Yield response of potato to spatially patterned nitrogen application. *Agriculture, Ecosystems & Environment* 129: 107–116. doi:10.1016/j.agee.2008.07.010.

Singh, D. 2011. Generation and evaluation of gross primary productivity using Landsat data through blending with MODIS data. *International Journal of Applied Earth Observation and Geoinformation* 13. Elsevier B.V. 59–69. doi:10.1016/j.jag.2010.06.007.

Song, C., and C. E. Woodcock. 2003. Monitoring forest succession with multitemporal landsat images: factors of uncertainty. *IEEE Transactions on Geoscience and Remote Sensing* 41: 2557–2567. doi:10.1109/TGRS.2003.818367.

Song, C., C. E. Woodcock, K. C. Seto, M. P. Lenney, and S. A. Macomber. 2001. Classification and Change Detection Using Landsat TM Data: When and How to Correct Atmospheric Effects? *Remote Sensing of Environment* 75: 230–244. doi:10.1016/S0034-4257(00)00169-3.

Sripada, R. P., J. P. Schmidt, A. E. Dellinger, and D. B. Beegle. 2008. Evaluating Multiple Indices from a Canopy Reflectance Sensor to Estimate Corn N Requirements. *Agronomy Journal* 100: 1553. doi:10.2134/agronj2008.0017.

The Royal Society. 2009. *Reaping the benefits: Science and the sustainable intensification of global agriculture*. London: The Royal Society.

Tucker, C. J. 1979. Red and photographic infrared linear combinations for monitoring vegetation. *Remote Sensing of Environment* 8: 127–150. doi:10.1016/0034-4257(79)90013-0.

Villa, G., J. Moreno, A. Calera, J. Amorós-López, G. Camps-Valls, E. Domenech, J. Garrido, J. González-Matesanz, et al. 2013. Spectro-temporal reflectance surfaces: a new conceptual framework for the integration of remote-sensing data from multiple different sensors. *International Journal of Remote Sensing* 34: 3699–3715. doi:10.1080/01431161.2012.716910.

Wald, L. 2002. *Data Fusion: Definitions and Architectures : Fusion of Images of Different Spatial Resolutions*. Paris, France: Presses des MINES.

Walker, J. J., K. M. de Beurs, R. H. Wynne, and F. Gao. 2012. Evaluation of Landsat and MODIS data fusion products for analysis of dryland forest phenology. *Remote Sensing of Environment* 117: 381–393. doi:10.1016/j.rse.2011.10.014.

Weng, Q. 2011. *Advances in Environmental Remote Sensing: Sensors, Algorithms and Applications*. Edited by Qihao Weng. Vol. 20112854. Remote Sensing Applications Series. Boca Raton, USA: CRC Press. doi:10.1201/b10599.

Wu, C., Z. Niu, Q. Tang, and W. Huang. 2008. Estimating chlorophyll content from hyperspectral vegetation indices: Modeling and validation. *Agricultural and Forest Meteorology* 148: 1230–1241. doi:10.1016/j.agrformet.2008.03.005.

Xin, Q., P. Olofsson, Z. Zhu, B. Tan, and C. E. Woodcock. 2013. Remote Sensing of Environment Toward near real-time monitoring of forest disturbance by fusion of MODIS and Landsat data. *Remote Sensing of Environment* 135: 234–247. doi:10.1016/j.rse.2013.04.002.

Zarco-Tejada, P. J., S. L. Ustin, and M. L. Whiting. 2005. Temporal and Spatial Relationships between Within-Field Yield Variability in Cotton and High-Spatial Hyperspectral Remote Sensing Imagery. *Agronomy Journal* 97: 641. doi:10.2134/agronj2003.0257.

Zhang, C., and J. Kovacs. 2012. The application of small unmanned aerial systems for precision agriculture: a review. *Precision Agriculture* 13: 693–712. doi:10.1007/s11119-012-9274-5.

Zhu, X., J. Chen, F. Gao, X. Chen, and J. G. Masek. 2010. An enhanced spatial and temporal adaptive reflectance fusion model for complex heterogeneous regions. *Remote Sensing of Environment* 114: 2610–2623. doi:10.1016/j.rse.2010.05.032.

Zurita-Milla, R. 2008. Mapping and monitoring heterogeneous landscapes : spatial , spectral and temporal unmixing of MERIS data. Wageningen University.

Zurita-Milla, R., J. G. P. W. Clevers, and M. E. Schaepman. 2008. Unmixing-Based Landsat TM and MERIS FR Data Fusion. *IEEE Geoscience and Remote Sensing Letters* 5: 453–457. doi:10.1109/LGRS.2008.919685.

Zurita-Milla, R., G. Kaiser, J. G. P. W. Clevers, W. Schneider, and M. E. Schaepman. 2009. Downscaling time series of MERIS full resolution data to monitor vegetation seasonal dynamics. *Remote Sensing of Environment* 113. Elsevier Inc. 1874–1885. doi:10.1016/j.rse.2009.04.011.

Zurita-Milla, R., L. Gómez-Chova, L. Guanter, J. G. P. W. Clevers, and G. Camps-Valls. 2011. Multitemporal Unmixing of Medium-Spatial-Resolution Satellite Images : A Case Study Using MERIS Images for Land-Cover Mapping. *IEEE Transactions on Geoscience and Remote Sensing* 49: 4308–4317. doi:10.1109/TGRS.2011.2158320.

9 Series from Lund University

Department of Physical Geography and Ecosystem Science

Master Thesis in Geographical Information Science (LUMA-GIS)

1. *Anthony Lawther:* The application of GIS-based binary logistic regression for slope failure susceptibility mapping in the Western Grampian Mountains, Scotland. (2008).
2. *Rickard Hansen:* Daily mobility in Grenoble Metropolitan Region, France. Applied GIS methods in time geographical research. (2008).
3. *Emil Bayramov:* Environmental monitoring of bio-restoration activities using GIS and Remote Sensing. (2009).
4. *Rafael Villarreal Pacheco:* Applications of Geographic Information Systems as an analytical and visualization tool for mass real estate valuation: a case study of Fontibon District, Bogota, Columbia. (2009).
5. *Siri Oestreich Waage:* a case study of route solving for oversized transport: The use of GIS functionalities in transport of transformers, as part of maintaining a reliable power infrastructure (2010).
6. *Edgar Pimiento:* Shallow landslide susceptibility – Modelling and validation (2010).
7. *Martina Schäfer:* Near real-time mapping of floodwater mosquito breeding sites using aerial photographs (2010)
8. *August Pieter van Waarden-Nagel:* Land use evaluation to assess the outcome of the programme of rehabilitation measures for the river Rhine in the Netherlands (2010)
9. *Samira Muhammad:* Development and implementation of air quality data mart for Ontario, Canada: A case study of air quality in Ontario using OLAP tool. (2010)
10. *Fredros Oketch Okumu*: Using remotely sensed data to explore spatial and temporal relationships between photosynthetic productivity of vegetation and malaria transmission intensities in selected parts of Africa (2011)
11. *Svajunas Plunge:* Advanced decision support methods for solving diffuse water pollution problems (2011)
12. *Jonathan Higgins:* Monitoring urban growth in greater Lagos: A case study using GIS to monitor the urban growth of Lagos 1990 - 2008 and produce future growth prospects for the city (2011).
13. *Mårten Karlberg:* Mobile Map Client API: Design and Implementation for Android (2011).
14. *Jeanette McBride:* Mapping Chicago area urban tree canopy using color infrared imagery (2011)
15. *Andrew Farina:* Exploring the relationship between land surface temperature and vegetation abundance for urban heat island mitigation in Seville, Spain

(2011)

16. *David Kanyari*: Nairobi City Journey Planner An online and a Mobile Application (2011)

17 *Laura V. Drews:* Multi-criteria GIS analysis for siting of small wind power plants - A case study from Berlin (2012)

18 *Qaisar Nadeem:* Best living neighborhood in the city - A GIS based multi criteria evaluation of ArRiyadh City (2012)

19 *Ahmed Mohamed El Saeid Mustafa:* Development of a photo voltaic building rooftop integration analysis tool for GIS for Dokki District, Cairo, Egypt (2012)

20 *Daniel Patrick Taylor*: Eastern Oyster Aquaculture: Estuarine Remediation via Site Suitability and Spatially Explicit Carrying Capacity Modeling in Virginia's Chesapeake Bay (2013)

21 *Angeleta Oveta Wilson:* A Participatory GIS approach to *unearthing* Manchester's Cultural Heritage '*gold mine'* (2013)

22 *Ola Svensson:* Visibility and Tholos Tombs in the Messenian Landscape: A Comparative Case Study of the Pylian Hinterlands and the Soulima Valley (2013)

23 *Monika Ogden:* Land use impact on water quality in two river systems in South Africa (2013)

24 *Stefan Rova:* A GIS based approach assessing phosphorus load impact on Lake Flaten in Salem, Sweden (2013)

25 *Yann Buhot:* Analysis of the history of landscape changes over a period of 200 years. How can we predict past landscape pattern scenario and the impact on habitat diversity? (2013)

26 *Christina Fotiou:* Evaluating habitat suitability and spectral heterogeneity models to predict weed species presence (2014)

27 *Inese Linuza:* Accuracy Assessment in Glacier Change Analysis (2014)

28 *Agnieszka Griffin:* Domestic energy consumption and social living standards: a GIS analysis within the Greater London Authority area (2014)

29 *Brynja Guðmundsdóttir* Detection of potential arable land with remote sensing and GIS - A Case Study for Kjósarhreppur (2014)

30 *Oleksandr Nekrasov* Processing of MODIS Vegetation Indices for analysis of agricultural droughts in the southern Ukraine between the years 2000-2012 (2014)

31 *Sarah Tressel* Recommendations for a polar Earth science portal in the context of Arctic Spatial Data Infrastructure (2014)

Appendix 1: Atmospheric correction of Formosat-2 imagery

Methodology

A number of different atmospheric correction methods were applied to the Formosat-2 imagery, and compared to the UAV reflectance to ascertain which is most applicable in the current situation. Firstly, Formosat-2 images were subsetted to an area of approximately 76 km^2 bounded by the UTM coordinates (647300, 5694000) and (654140, 5682800). Although this extent is much larger than the field which is analyzed in the current application, it was presumed that a larger study area increased the amount of endmembers in the image and the possibility of locating dark vegetation pixels and pseudo-invariant features (PIFs). It was hypothesized that this allowed for a more accurate atmospheric correction. After the atmospheric correction, the Formosat-2 images were subsetted to the extent of the potato field under study.

The following atmospheric correction methods were selected based on software availability (ERDAS Imagine 2013, ENVI 5.0.3 and Matlab R2012b):

- ***Dark object Subtraction (DOS)* –** This method is one of the most elementary atmospheric correction methods, though it is widely-used (Song *et al.* 2001). It assumes the existence of pixels within the scene which have negligible reflectance – such as dense dark vegetation or shadows. Therefore, the minimal reflectance value per band is due to atmospheric scattering effects. The algorithm assumes that the atmospheric effects are constant throughout the scene, and can be corrected by subtracting this minimal reflectance from each pixel in the scene (Chavez 1988).
- ***ATCOR* –** is based on the MODTRAN 4 radiative transfer code, integrated into ERDAS Imagine software. Apart from the required input atmospheric and ancillary data, it allows for the selection of input reference spectra (Manakos *et al.* 2011). In the current application, a rural mid-latitude summer atmosphere was assumed. As the images had no clouds and Formosat-2 imagery contains no water vapor bands, these ATCOR functions were not utilized.
- ***FLAASH* –**is also based on MODTRAN 4 (Felde *et al.* 2003), and is integrated into ENVI software (version 5.0). It includes a number of high-level atmospheric correction functions such as adjacency correction, water vapor retrieval and spectral polishing (Weng 2011). FLAASH was run using the same input parameters as ATCOR.
- ***QUAC* –** assumes there is a linear relationship between the actual spectral reflectance of a surface, and the reflectance observed by the satellite. The bias of this relationship is obtained by the minimal pixel value per spectral band. The gain is calculated by comparing the average spectrum of endmembers within the scene to the average spectrum of reference spectra from a library. Benefits of this method include: fast computation, no ancillary information requirements, and it can be applied to spectrally uncalibrated data (Bernstein *et al.* 2012). This method is also integrated in ENVI.
- ***Empirical line correction* –** requires two or more known reflectance in the image, preferably one bright and one dark. A linear regression is formed between the image spectra and the reference spectra, and it is assumed that the gain and offset are applicable to the rest of the image

(Karpouzli and Malthus 2003). In the current application, reference spectra were not available. Therefore, the reference spectra were determined by the surface reflectance of defined PIFs. The PIFs were selected by calculating the standard deviation of surface reflectance values in all the Formosat-2 imagery. Pixels with a standard deviation of less than 0.06 (a threshold determined by analyzing the histogram of the variance image) in surface reflectance throughout the time series were defined as PIFs. These pixels were masked, and an erode filter was applied. This supported the selection of homogenous areas, and decreased the influence of geolocation errors and adjacency effects. The surface reflectance of the resulting pixels on June 6th were used as input for the empirical line correction.

- ***Radiometric calibration -*** normalizes all the images in a time series to a reference image. This is done by selecting PIFs in the images, defining a linear regression between the spectral values of the reference image and each other image, and applying the gain and bias of the regression to the entire image. It is often helpful if the reference image is in absolute surface reflectance (Schroeder *et al.* 2006). In the current application, the empirical line correction (above) was used to normalize the surface reflectance of Formosat-2 for all images in the time series. Then, the radiometric calibration method was applied to calibrate the Formosat-2 reflectance to the UAV reflectance.

The first four methods were applied to all Formosat-2 imagery. The images of June 6th and July 18th were selected as reference images. The mean reflectance of the UAV spectral bands corresponding to the Formosat-2 spectral bands were calculated and compared to the Formosat-2 reflectance values obtained through the different atmospheric correction methods for the images on June 6th and July 18th. Spearman's correlation coefficient and the RMSE were utilized as quality indicators for determining the most adequate correction method.

The most adequate atmospheric correction method was determined, and a radiometric calibration between the Formosat-2 image corrected by the optimal method and the UAV image of June 6th was applied. Again, the results of the six atmospheric correction methods were compared using Spearman's correlation coefficient and RMSE. The atmospheric correction method with the highest correlation and lowest RMSE to the UAV imagery was selected for further processing.

Results

Firstly, the atmospheric correction methods ATCOR, DOS, FLAASH, and QUAC were applied to the Formosat-2 imagery and compared to the UAV data on the same day (June 6th). The correlation coefficient for the DOS and QUAC methods were the highest, whereas ATCOR and FLAASH obtained slightly lower correlation coefficients (Figure 25). The QUAC method also had lowest RMSE for the first, second and third spectral bands, although the FLAASH and ATCOR methods provided lower RMSE values for the fourth spectral band (Figure 26). It was concluded that although the accuracy of all methods was quite similar, the precision of the QUAC method is slightly better in the current study and therefore the preferable method of atmospheric correction. Therefore, the QUAC method was utilized as input for the empirical line calibration to normalize reflectance throughout the time series and a radiometric calibration to the UAV imagery.

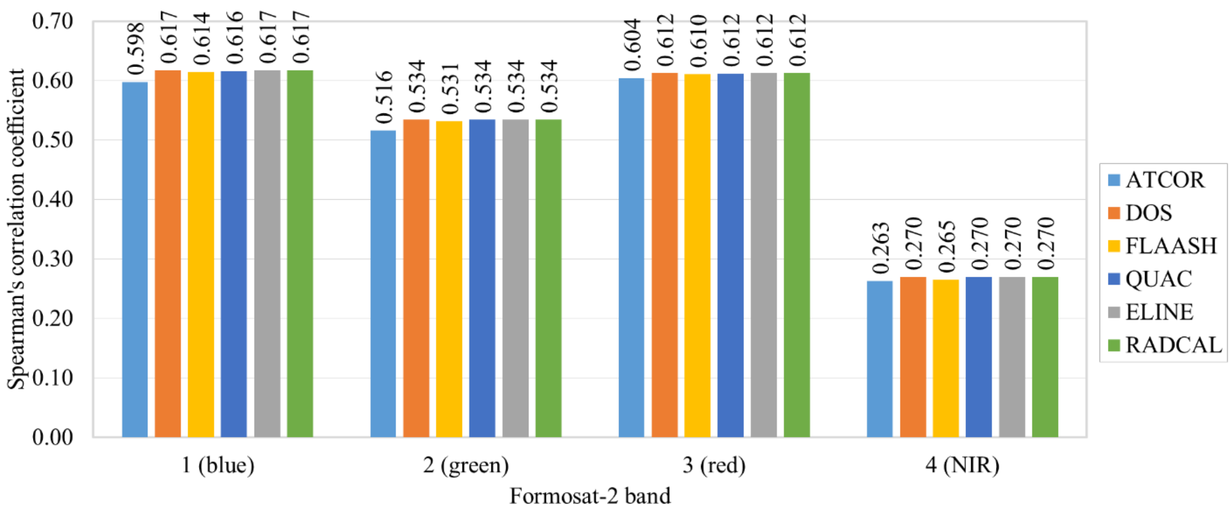

Figure 25: Spearman's correlation coefficient (r_s) between the Formosat-2 image after the application of various atmospheric correction methods and the UAV imagery on the same date.

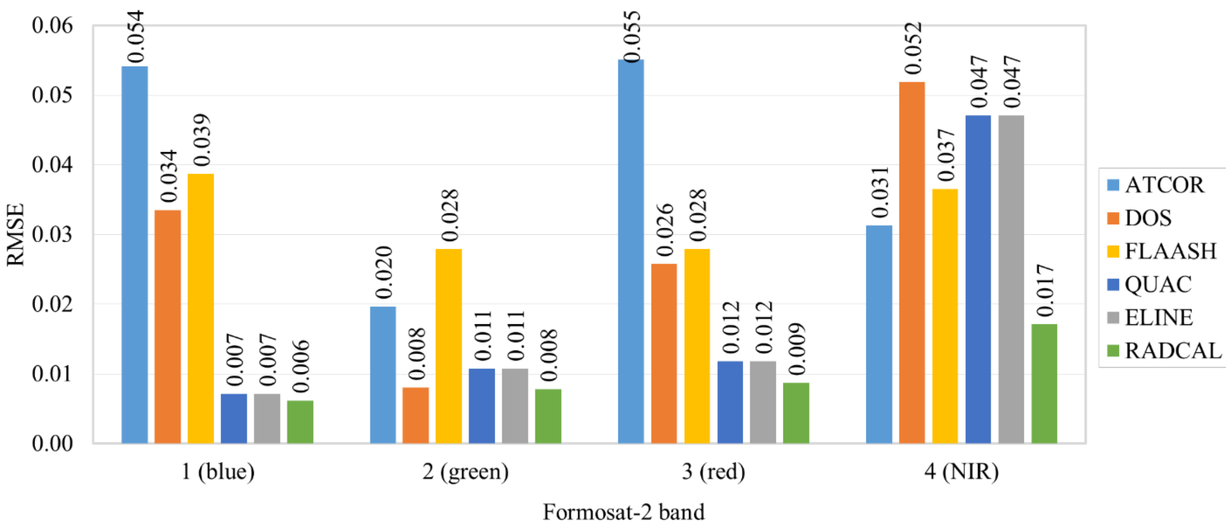

Figure 26: RMSE between the Formosat-2 image after the application of various atmospheric correction methods and the UAV imagery on the same date.

Appendix 2: Data fusion parameter optimization

Methodology

Before the application of data fusion to an image time series, a number of input parameters related to fusion processes were optimized (Gao et al. 2006; Zurita-Milla et al. 2011). In the optimization phase, two tests were used to obtain the optimal parameters. The first test used input Formosat-2 and UAV imagery to 'predict' the fused image of the same day (in this case, both input imagery and prediction date was June 6th). This gives an indication to the quality of the fused image in a situation where there is input imagery available close to the prediction date, simulating a situation of no temporal change. The second test used input Formosat-2 and UAV imagery from a base date (June 6th), and Formosat-2 imagery on a prediction date (July 18th) to predict the fused image on July 18th. This second test is important as it simulates a realistic situation in which the input imagery is not temporally close to the prediction date. This could happen in real-life applications in which, for example, cloudy periods limit the number of available satellite data. Using the results of both simulations to define the input parameters allows for the selection of robust parameters which function well the application of data fusion to situations of various degrees of temporal change.

For the application of unmixing-based data fusion, two input parameters must be optimized: the size of the moving window (ω) and the number of clusters (k) (Zurita-Milla *et al.* 2009). To do this, the unmixing code was run using various input values (Table 7). The moving-widow size parameter ranged from the minimum window size (3x3 pixels) to the entire image (29x29 pixels). Similarly, the number of clusters is always minimally 2, and ranged to a maximum of 16 clusters after which the clusters were observed to be too small to meet the minimum fraction requirement of unmixing-based fusion algorithm.

Table 7: The range of input parameter values used for the parameter optimization step.

Image fusion methods	Parameters	Tested range
Unmixing indicator	Moving-window size (ω)	3 – 29 Formosat-2 pixels (steps of 4)
	Number of clusters (k)	2 – 16 (steps of 2)
STARFM indicator	Search distance	5m – 30m (steps of 5) 15m – 105m (steps of 15)
	Number of spectral slices	24 – 80 (steps of 4) 10 – 40 (steps of 10)

For the STARFM method, the search distance and number of spectral slices must be optimized (Gao *et al.* 2006). The parameters were varied as indicated in Table 7, based on the same criteria as the moving-window and number of cluster intervals in the unmixing-based method. Furthermore, the STARFM method requires the images to have corresponding spectral bands (Gao *et al.* 2006). Formosat-2 imagery has four spectral bands, while the UAV hyperspectral imagery has 110 spectral bands. The STARFM method was tested using the UAV bands corresponding to the center of the Formosat-2 bands, and using the UAV band which was optimally correlated to each Formosat-2 band (Table 8). For the latter, Spearman's correlation coefficient was used to identify the optimal correlation. Scatterplots between Formosat-2 and optimally correlated UAV bands are given in Figure 27.

Table 8: The UAV bands selected for STARFM data fusion tests. Source for the Formosat-2 spectral band information: (Liu *et al.* 2010)**.**

Spectrum	Formosat-2 band			$UAV_{central}$			$UAV_{optimal}$		
	Band no	λ_{range} (nm)	λ_{center} (nm)	Band no	λ_{center} (nm)	r_s	Band no	λ_{center} (nm)	r_s
Blue	1	455-515	485	8	485	0.863	11	500	0.8702
Green	2	525-595	560	23	560	0.810	30	595	0.848
Red	3	630-690	660	43	660	0.845	42	635	0.854
NIR	4	765-895	830	77	830	0.646	87	880	0.658

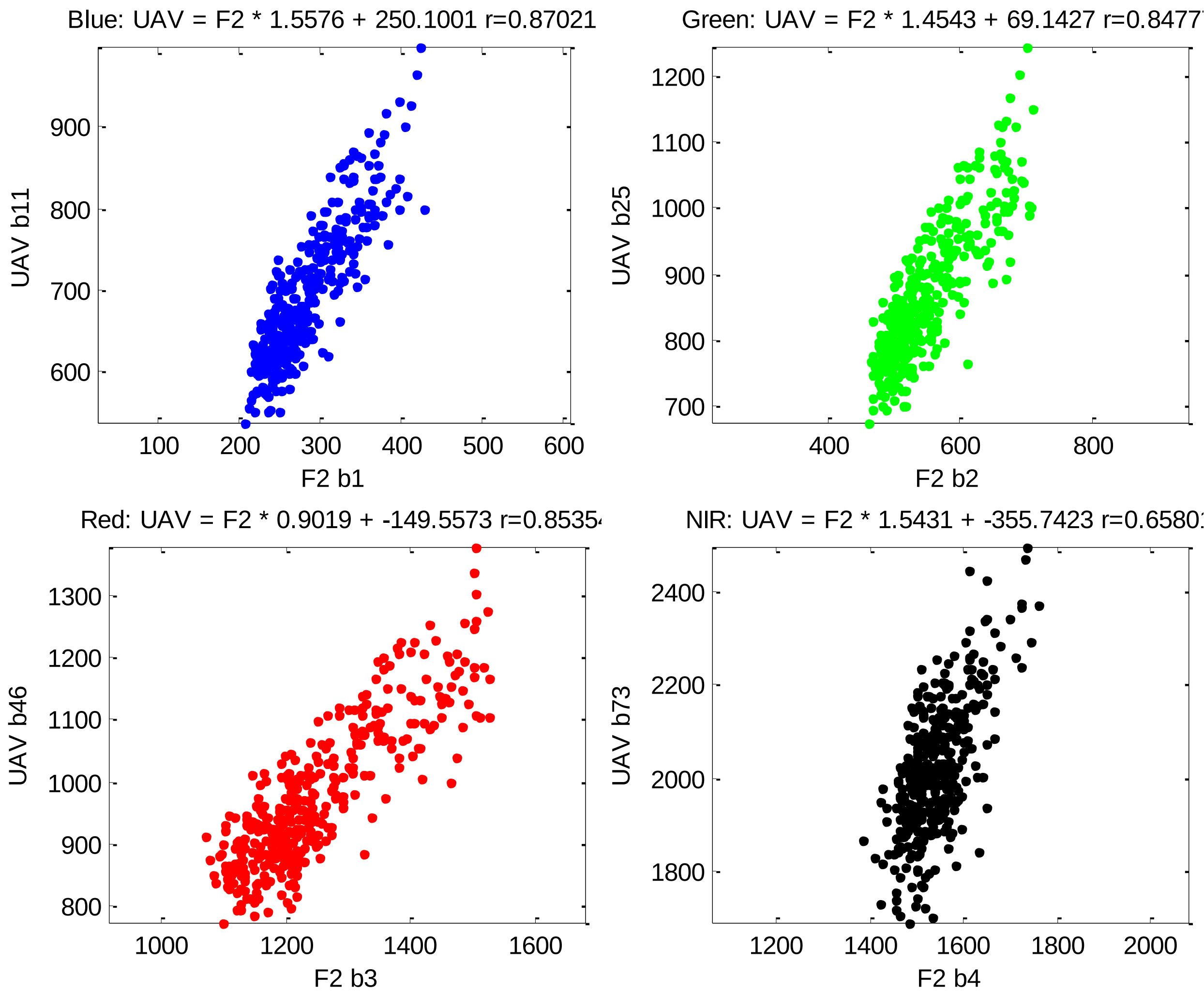

Figure 27: Scatterplots showing the relation between the Formosat-2 spectral bands and corresponding UAV bands with the highest correlations.

The optimal input parameters for each data fusion method were defined by using various quality indicators. For the unmixing-based fusion, the spectral (Wald 2002) and spatial (Lillo-Saavedra *et al.*

2005) Erreur Relative Globale Adimensionnelle de Synthèse (ERGAS) were used. For the STARFM method, the RMSE, bias and Spearman's correlation coefficient (r) were used.

Results

The unmixing process utilizes an automatic k-means clustering. Clusters will not be identical if the same test is run twice. Therefore, the unmixing-based tests in the parameter optimization stage were run twice, to give an indication of the variability of the fusion quality. As the ERGAS indicators for smaller numbers of clusters are closer together, it suggests that the unmixing-based fusion results using smaller numbers of clusters are more stable than those using more clusters. However, using smaller numbers of clusters also causes the results of unmixing-based data fusion to become more homogenous and less sensitive to variation within the scene.

The results indicate that for low moving window sizes (w) and high numbers of clusters (k), the fusion results have higher ERGAS values, indicating a lower quality. Furthermore, the spectral ERGAS is similar for both the same day tests, using the input images from June 6th to predict the same date (Figure 28) and the July 18th predictions, still using the June 6th input images (Figure 29). However, the spatial ERGAS is worse for the second test. This could be due to the significant changes in vegetation between June 6th (low crops and no visible differences between fertilization rates) and July 18th, where the different fertilization zones are obvious. The optimal input parameters were defined as a window size of 9x9 Formosat-2 pixels, and 10 clusters. This supports the guideline that the number of pixels within the moving window (ω^2) be much larger than the number of clusters to be unmixed (García - Haro et al. 2005). The 10 clusters obtains a higher quality fusion than larger numbers of clusters, whereas the use of fewer clusters compromises the heterogeneity of the unmixed image.

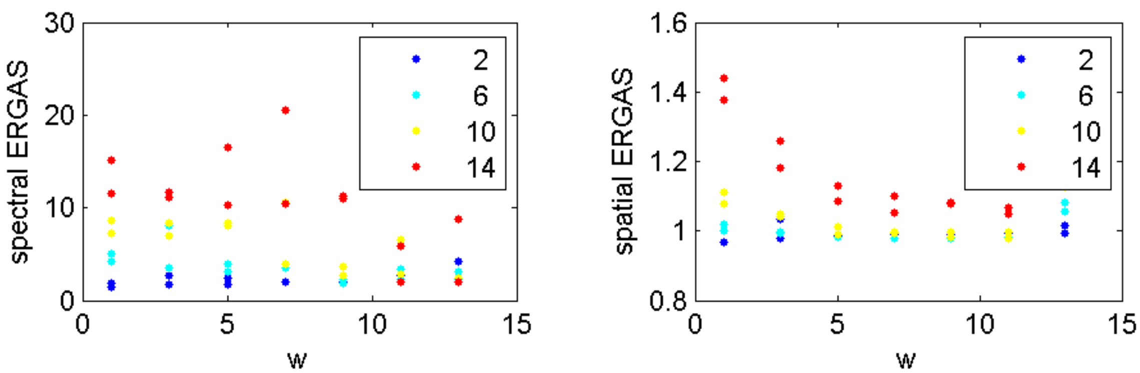

(a) (b)

Figure 28: The spectral (a) and spatial (b) ERGAS resulting from unmixing-based fusion with varying input parameters - same-day prediction. Window size (ω) is given along the x axis, while varying numbers of classes (k) is given in different colors.

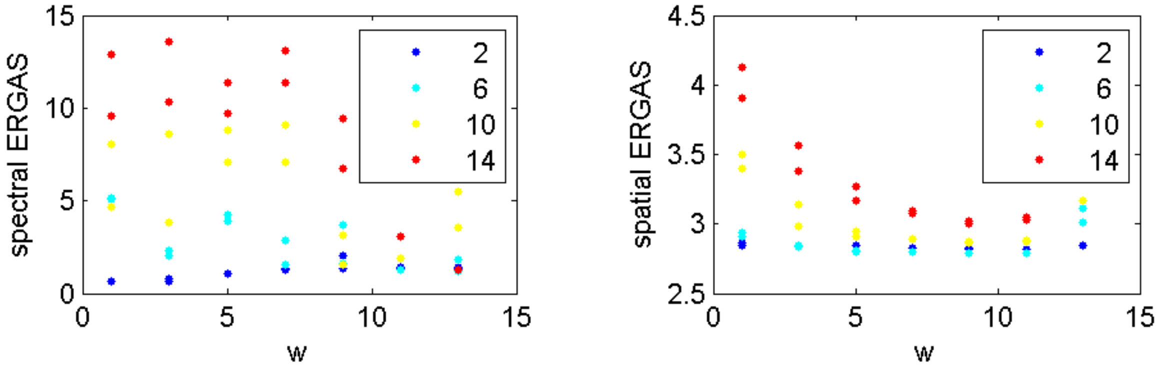

(a) (b)

Figure 29: The spectral (a) and spatial (b) ERGAS resulting from unmixing-based fusion with varying input parameters - different-day prediction. Window size (ω) is given along the x axis, while varying numbers of classes (k) is given in different colors.

Unlike the unmixing-based data fusion results, the STARFM method does show substantial differences between the quality of June 6th and July 18th predictions. This is due to the nature of the STARFM method; if there is no change between the spectral reflectance of the medium-resolution image between the base and prediction date, the predicted high-resolution pixel will be assigned the same value as the high-resolution pixel on the base image date. Therefore, Spearman's r_s is equal to 1.000 and the RMSE is equal to 0.000 for all input parameters of first June 6th predictions.

A second comparison in the STARFM optimization phase addressed the question of which UAV band should be used in the data fusion process – the band corresponding to the center of each Formosat-2 band or the optimally correlated band. The results (Figures 30 and 31) indicate that the usage of the UAV spectral band corresponding to the center of the Formosat-2 band produces a slightly lower RMSE and slightly higher correlation coefficient (r) and is therefore preferred.

The input number of spectral slices has very little influence on the predictions, barely changing the RMSE or r. The search distance slightly alters the RMSE (a range of 1.335-1.345 x 10^{-5}) and r (0.71-0.715) (Figure 31). Therefore, the quality of the STARFM fusion in the current scenario appears to be relatively robust to changes in the input parameters. For the current application, a search distance of 105 and 30 spectral slices were defined as the optimal input parameters.

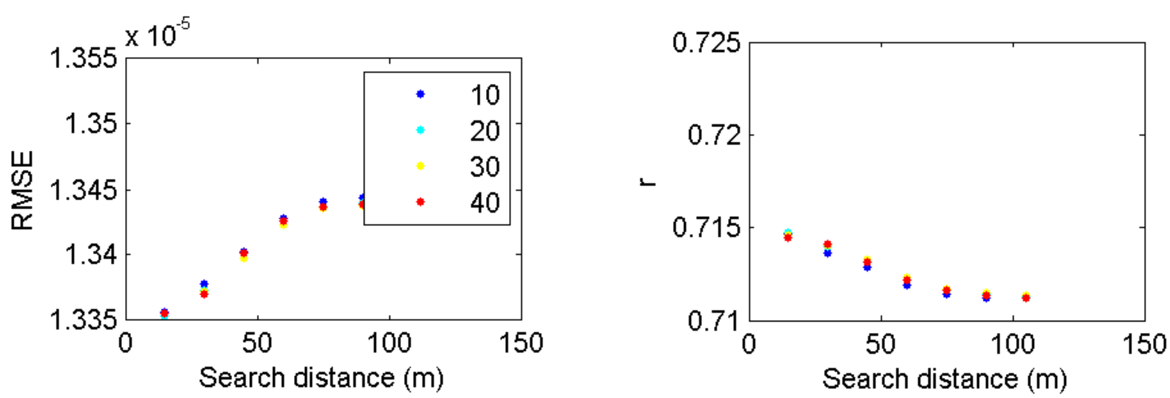

(a) (b)

Figure 30: The RMSE (a) and r (b) resulting from STARFM fusion with varying input parameters - different-day prediction and central band selection. Search distance is presented along the x-axis whereas number of slices is given in different colors.

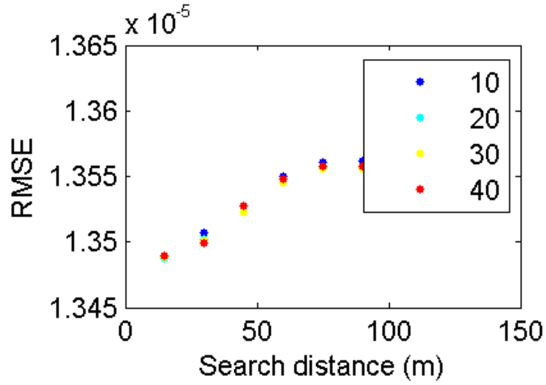

(a)

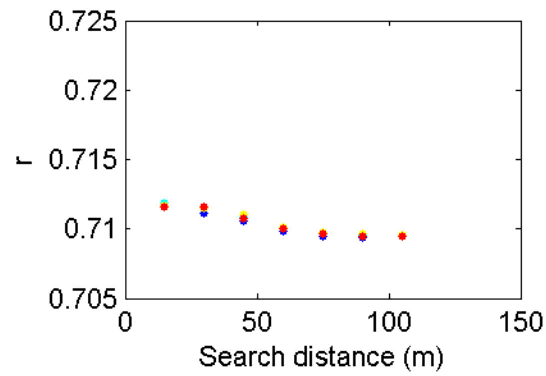

(b)

Figure 31: The RMSE (a) and r (b) resulting from STARFM fusion with varying input parameters - different-day prediction and highest correlated band selection. Search distance is presented along the x-axis whereas number of slices is given in different colors.

Appendix 3: Vegetation indices

Name	**Formula**	**Source**
Multispectral indices		
EVI	$EVI = 2.5 * \frac{NIR - R}{1 + NIR + 6R - 7.5xB}$	(Kerr and Ostrovsky 2003)
GNDVI	$GNDVI = \frac{NIR - G}{NIR + G}$	(Osborne *et al.* 2004)
GRVI	$GRVI = NIR/G$	(Sripada *et al.* 2008)
MCARI2	$MCARI2 = \frac{1.5*[2.5*(NIR-R)-1.3*(NIR-B)}{\sqrt{(2*NIR+1)^2-(6*NIR-5*\sqrt{R})-0.5}}]$	(Haboudane *et al.* 2004)
MTVI	$MTVI = \frac{1.2 * [1.2 * (NIR - G) - 2.5 * (R - G)]}{\sqrt{(2 * NIR + 1)^2 - (6 * NIR - 5 * \sqrt{R}) - 0.5}}$	(Haboudane *et al.* 2004)
NDVI	$NDVI = \frac{NIR - R}{NIR + R}$	(Tucker 1979)
WDVI[1]	$WDVI = NIR - C * R$	(Clevers 1989)
SAVI[2]	$SAVI = \frac{(1 + L) * (NIR - R)}{NIR + R + L}$	(Huete 1988)
TVI	$TVI = 100 * \sqrt{\frac{NIR - R}{NIR + R + 0.5}}$	(Broge and Leblanc 2001)
OSAVI	$OSAVI = \frac{1.16 * (NIR - R)}{NIR + R + 0.16}$	(Gamon *et al.* 1997)
Hyperspectral indices		
MCARI	$MCARI = [(\rho_{700} - \rho_{670}) - 0.2 * (\rho_{700} - \rho_{550})] * \left(\frac{\rho_{700}}{\rho_{670}}\right)$	(Daughtry et al. 2000)
$WDVI_{green}$	$WDVI_{green} = \rho_{780} - 1.6 * \rho_{570}$	(Clevers and Verhoef 1993)
TCARI	$TCARI = 3[(\rho_{700} - \rho_{670}) - 0.2(\rho_{700} - \rho_{550}) * (\rho_{700}/\rho_{670})]$	(Haboudane et al. 2002)
NDRE	$NDRE = (\rho_{790} - \rho_{720})/(\rho_{790} + \rho_{720})$	(Barnes et al. 2000)
MSAVI	$MSAVI = 0.5 * (2 * \rho_{780} + 1 - \sqrt{(2 * \rho_{780} + 1)^2 - 8(\rho_{780} - \rho_{670})}$	(Qi et al. 1994)
TCARI[705,750][3]	$TCARI_{705,750} = 3[(\rho_{750} - \rho_{750}) - 0.2(\rho_{750} - \rho_{550}) * (\rho_{750}/\rho_{750})]$	(Wu et al. 2008)
OSAVI[705,750][3]	$OSAVI_{705,750} = \frac{1.16 * (\rho_{750} - \rho_{705})}{\rho_{750} + \rho_{705} + 0.16}$	(Wu et al. 2008)
TCARI [705,750] / OSAVI [705,750][3]	$TC/OS[705,750] = \frac{TCARI_{705,750}}{OSAVI_{705,750}}$	(Wu et al. 2008)

[1]C = 2 for the current study area (Kooistra et al. 2013). [2]L = 0.5 [3][705,750] means the indices utilize the 705 nm and 750 nm wavelengths rather than 670 nm and 800 nm as in the original indices.

Appendix 4: WHISPERS 2014 Submission

COMBINING HYPERSPECTRAL UAV AND MULTISPECTRAL FORMOSAT-2 IMAGERY FOR PRECISION AGRICULTURE APPLICATIONS

C.M. Gevaert[1], J.Tang[1], F.J. García-Haro[2], J. Suomalainen[3] & L. Kooistra[3]

[1] Department of Physical Geography and Ecosystem Science, Lund University, Sölvegatan 12, S-223 62 Lund, Sweden

[2] Department of Earth Physics and Thermodynamics, University of Valencia, Dr. Moliner, 50. 46100 Burjassot, Valencia, Spain

[3] Laboratory of Geo-Information Science and Remote Sensing, Wageningen University, P.O. Box 47, 6700 AA Wageningen, the Netherlands

ABSTRACT

Remote sensing is a key tool for precision agriculture applications as it is capable of capturing spatial and temporal variations in crop status. However, satellites often have an inadequate spatial resolution for precision agriculture applications. High-resolution Unmanned Aerial Vehicles (UAV) imagery can be obtained at flexible dates, but operational costs may limit the collection frequency. The current study utilizes data fusion to create a dataset which benefits from the temporal resolution of Formosat-2 imagery and the spatial resolution of UAV imagery with the purpose of monitoring crop growth in a potato field. The correlation of the Weighted Difference Vegetation Index (WDVI) from fused imagery to measured crop indicators at field level and added value of the enhanced spatial and temporal resolution are discussed. The results of the STARFM method were restrained by the requirement of same-day base imagery. However, the unmixing-based method provided a high correlation to the field data and accurately captured the WDVI temporal variation at field level (r=0.969).

Index Terms— UAV, STARFM, unmixing-based data fusion, precision agriculture, WDVI

1. INTRODUCTION

Precision agriculture aims to maximize agricultural production in a sustainable manner by optimizing the use of input resources. This may provide economic and environmental benefits and play an important role in global food security. The key behind precision agriculture is quantifying spatial and temporal variation in crop conditions in order to apply variable management strategies within a field (Gebbers and Adamchuk 2010).

Remote sensing is capable of observing such variation in plant growth indicators such as canopy nitrogen content and plant biomass (Clevers and Kooistra 2012). A number of studies describe the use of multispectral satellite imagery for precision agriculture applications (Diacono et al. 2012). However, factors such as inadequate spatial or temporal resolution and cloud cover (Mulla 2013) have limited the effectiveness of utilizing satellite imagery. Alternatively, Unmanned Aerial Vehicles (UAV) have been proposed for precision agriculture applications (Kooistra et al. 2013) as they can provide hyperspectral imagery with a higher spatial resolution and more flexible acquisition times (Zhang and Kovacs 2012). However, operational requirements may inhibit monitoring of large areas and the frequency of flights.

Recently, much research has been done on the application of data fusion between medium-resolution imagery such as MODIS (Gao et al. 2006) and MERIS (Zurita-Milla et al. 2008) and high-resolution datasets such as Landsat to obtain a fused image dataset with a daily temporal resolution and a spatial resolution of 30 m. Two prevalent data fusion methods are the Spatial and Temporal Adaptive Reflectance Fusion Model (STARFM) (Gao et al. 2006) and unmixing-based data fusion (Zurita-Milla et al. 2008). These methods could be adapted to fuse multispectral satellite imagery such as Formosat-2 with hyperspectral imagery obtained from an UAV platform for precision agriculture applications.

The objective of the current study is to develop a method for data fusion between Formosat-2 imagery and hyperspectral UAV imagery of a potato field in the Netherlands to obtain a fused dataset for crop monitoring in precision agriculture applications. The resulting image time series benefits from an increased temporal resolution obtained from the multispectral satellite imagery, and an increased spatial resolution obtained from the UAV dataset.

2. METHODOLOGY

2.1. Study Area

The study area is a potato field at 51°19’ N and 5°10’14” E, near the village of Reusel in the Netherlands. At the beginning of the 2013 growing season, the field was divided into four zones and applied with differing initial nitrogen fertilization rates: 0, 90, 162 and 252 $kgN.ha^{-1}$. Six experimental plots of 13x30 m were delimited per zone, for which chlorophyll was measured using a Minolta SPAD-502, Leaf Area Index (LAI) was measured with a LAI-2000, and spectral reflectances were obtained using a Cropscan Multispectral Radiometer (MSR16R). Measurements were taken weekly between June 6th and August 23rd, 2013. More information regarding the experimental setup can be found in Kooistra et al. (Kooistra et al. 2013).

2.2. Imagery

A hyperspectral system on an UAV consisting of a Specim ImSpector V10 2/3” spectrograph mounted on an Aerialtronics Altura AT8 octocopter was developed by the Wageningen University (WU) Laboratory of Geo-information Science and Remote Sensing (GRS) under the Smart Inspectors project (Kooistra et al. 2013). This UAV was flown over the study area at four dates (June 6, June 14, July 5 and July 17, 2013) to obtain imagery with 101 spectral bands at a spatial resolution of 1 m. All images have been georeferenced, orthorectified and atmospherically corrected (Kooistra et al. 2013).

Formosat-2 imagery have a spatial resolution of 8 m, and consists of four multispectral bands (Liu 2006). During the 2013 growing season, eight cloud-free Formosat-2 images were available over the study area: April 24, June 6, June 8, July 2, July 8, July 18, July 22, and August 2, 2013. The images were georeferenced and radiometrically corrected using the coefficients provided in the metadata. A high-resolution aerial photograph was used to coregister the UAV and Formosat-2 imagery. The QUAC method was applied to atmospherically correct the Formosat-2 image of June 6th. An empirical line correction was then applied between all the other Formosat-2 images and the June 6th image, to calibrate the spectral signature throughout the time series. Finally, calibration coefficients were obtained from the UAV and Formosat-2 images of June 6th, and all Formosat-2 images were calibrated to the UAV imagery.

2.3. Data fusion

The current study made use of two data fusion algorithms: an unmixing-based algorithm and STARFM. The unmixing-based algorithm is based on previous works by (Zurita-Milla et al. 2008). It considers a linear mixing model in which the resolution of the medium-resolution imagery is assumed to be a summation of the spectra of each endmember within the pixel weighted by the abundance of the endmember within the pixel. The endmembers are obtained by performing a clustering algorithm, in this case a k-means clustering, on the high-resolution input data (i.e. the UAV imagery). The abundances of each endmember can be calculated by overlaying the medium-resolution imagery and the high-resolution unsupervised classification. The unmixing-based method is applied using a moving-window to allow for spectral heterogeneity of endmembers throughout the scene.

Spectral unmixing may produce unrealistic spectra if the process is not restricted. This is often done by limiting reflectance values to positive values and certain upper limits [9]. The current application utilized Bayesian theory to restrain the unmixing process by including a priori spectral information selected from a homogenous Formosat-2 pixel of each endmember (Gevaert and García-Haro 2014).

The STARFM method is based on the premise that both high- and medium-resolution imagery observe the same spectral reflectances, biased by a systematic error. This error is consistent over short spatial and temporal intervals. Using a reference pair of high- and medium-resolution images on a base date, the bias is calculated by selecting neighbors based on selection criteria (Gao et al. 2006) within a set search distance to form a linear system of equations. Once the bias has been obtained from the base image pair, it can then be applied to a medium-resolution image on a different day to obtain a synthetic high-resolution image. In the current application, Formosat-2 provided the medium-resolution imagery and the UAV provided the high-resolution imagery. To apply the STARFM method, both sources of imagery must have corresponding spectral bands. Therefore, the spectral bands of the hyperspectral UAV imagery corresponding to the wavelengths of each of the four Formosat-2 bands was averaged to create a UAV image with four spectral bands.

The input parameters of each algorithm were first optimized by applying data fusion to the UAV imagery on June 6th and the Formosat-2 imagery on July 17th, which allowed for the comparison of the fused image to the actual UAV image of July 17th. For the unmixing-based method, the moving window size was varied from 3x3 to 29x29 Formosat-2 pixels in steps of 4 and the number of spectral clusters was varied from 2 to 16 in steps of 2. The quality of the fusion was determined by calculating the spectral and spatial ERGAS. For the STARFM method, the maximum search distance was varied from 15 m to 105 m, and the number of spectral slices was varied from 10 to 40. The fusion quality was analyzed by calculating Spearman’s correlation and the RMSE to the ground-truth UAV image.

Next, data fusion was applied to each Formosat-2 image. For the unmixing-based method, each Formosat-2

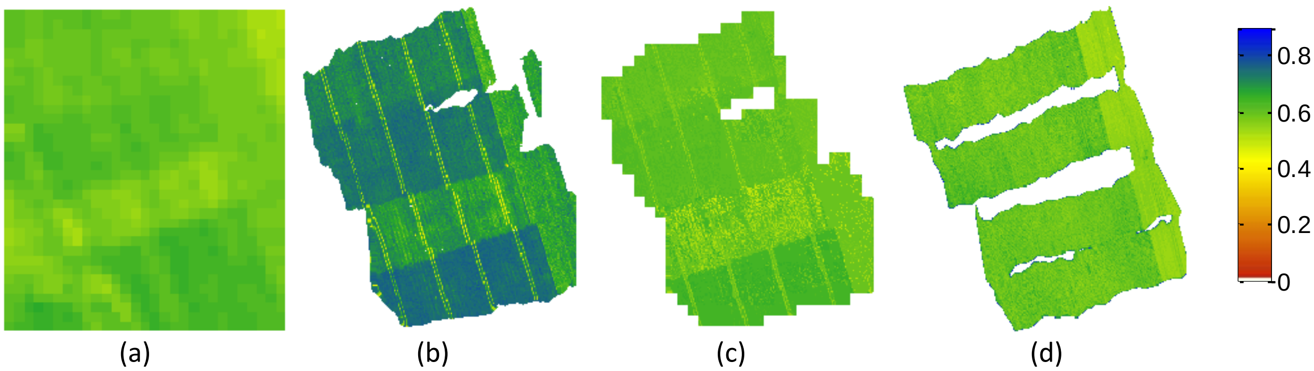

Fig. 1. WDVI obtained from the Formosat-2 satellite image on July 8th (a), the UAV image on July 5th (b), and the fused product of the unmixing-based algorithm (c), and STARFM (d) on July 8th.

Table 1. Spearman's correlation coefficient between the average WDVI per plot calculated from imagery and reference data. All correlations are significant at $p<0.001$.

Reference indicator	Unmixing	STARFM	UAV	F2
Field WDVI	0.802	0.463	0.847	0.808
LAI	0.866	0.477	0.872	0.861
Canopy chlorophyll (g/m^2)	0.884	0.431	0.882	0.869

image was fused with the closest preceding UAV image. As there was no UAV image preceding April 24th, this Formosat-2 image was fused with the UAV image on June 6th. The STARFM method requires an input base pair of Formosat-2 and UAV imagery on the same date. Therefore, only the UAV images on June 6th and July 17th could be used to create the data fusion time series.

2.4. Validation

The Weighted Difference Vegetation Index (WDVI) (Clevers 1989)
was used to calculate the correlation between the imagery and the field data. Canopy chlorophyll was calculated by multiplying the leaf chlorophyll measurements by the LAI.
The image WDVI, field WDVI, LAI and canopy chlorophyll were averaged to plot level. The imagery on the dates June 6, July 2, July 18 and August 2 were compared to the field data on June 6, July 5, July 17, and July 31, assuming that a 3-day interval presented no significant changes to the WDVI. Furthermore, temporal WDVI profiles were made for an experimental plot receiving no initial fertilization.

3. RESULTS AND DISCUSSION

In the parameter optimization stage for unmixing, a window size of 9x9 Formos-2 pixels and 10 clusters obtained the best quality indicators (spatial ERGAS = 2.76; spectral ERGAS = 0.98). STARFM produced the best results with a search distance of 105 m and 30 spectral slices ($r=0.715$; RMSE = 0.133×10^{-5}). However, through all the variations in input parameters, the STARFM correlation coefficient only varied between 0.710 and 0.715 and the RMSE varied from 1.335 – 1.345 $\times 10^{-5}$. This suggests that STARFM is relatively insensitive to variations in the input parameters in the current application, and future applications could dedicate less time to the parameter optimization phase.

The WDVI calculated from the Formosat-2 imagery has a high correlation to crop status indicators (Table 1), which indicates that it contains relevant information regarding crop status and is a valuable input for data fusion methods. The unmixing-based method provides similar correlation coefficients to the Formosat-2 imagery. This is expected as the spectral information in the unmixing-based data is derived from the Formosat-2 imagery, and the correlation coefficients presented in Table 1 are averaged at a plot level of 15x30 m. The added spatial resolution is thus not taken into account in these correlation coefficients, although Figure 1 clearly illustrates the added value of the improved spatial resolution.

The STARFM method presented the lowest correlation to the field observations, which is likely due to the use of only two of the UAV images as high-resolution input for the fused time series. As the unmixing-based method can utilize all four UAV images as input, spatial variation is captured at an earlier stage in the growing season. For the image on July 8th, for example, unmixing-based fusion could utilize the input UAV image on July 5th and thus correctly differentiates the vegetation status of the different nitrogen application rate zones (Figure 1). As there is no corresponding Formosat-2 image on July 5th, the STARFM method must use the imagery of June 6th as a base date and cannot differentiate crop growth variation between fertilizer application-rate zones.

From each image source, temporal profiles can be constructed to analyze the crop status during the growing season. Figure 2 presents the normalized temporal WDVI profiles of one of the experimental plots receiving no initial fertilization. The UAV WDVI closely follows the

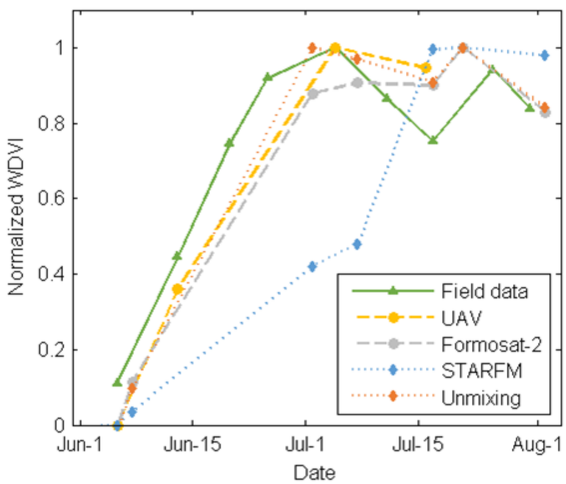

Fig. 2. Temporal Normalized WDVI profiles of an experimental plot receiving no initial fertilization. Normalized values are obtained by dividing by the maximum seasonal WDVI per field observations, but no UAV imagery is available after July 17th. The STARFM method once again clearly shows the influence of the input base image pair, and does not provide consistent results in the current study. However, the relative temporal variation of the Formosat-2 and unmixing-based imagery follows the temporal pattern of the field data – although the WDVI is systematically lower. During the growing season, the farmer applied additional fertilization in mid-July which causes the increase in WDVI at this time. There was no UAV imagery available after this date to capture the changes, but the increase in WDVI is correctly captured in the unmixing-based WDVI profile. This is an example of the added value of the enhanced temporal resolution provided by data fusion.

4. CONCLUSIONS

The current study demonstrates the utility of applying data fusion methods to combine satellite imagery with UAV imagery for precision agriculture applications. The STARFM method is limited in the current situation by the requirement of base imagery from both sources on the same date and therefore presents temporally unstable results. This could be mitigated by coinciding UAV operations with satellite collection dates in future studies. The unmixing-based method presented a high correlation to the WDVI (r=0.969), LAI (r=0.896) and canopy chlorophyll (r=0.788) measured at field level. The WDVI obtained from unmixing-based data fusion presented a bias to the UAV WDVI, which is likely due to differing processing chains of the UAV and Formosat-2 data. However, the relative phenological variations were more accurately captured by the time series created by the unmixing-based method. This study indicates how the fused dataset can combine the temporal resolution of the Formosat-2 imagery and the spatial resolution of the UAV imagery for precision agriculture applications.

4. ACKNOWLEDGEMENTS

This research is part of the Smart Inspectors project funded by the INTERREG IV A program Deutschland-Nederland.

5. REFERENCES

[1] R. Gebbers and V. I. Adamchuk, “Precision agriculture and food security.,” Science, vol. 327, no. 5967, pp. 828–31, Feb. 2010.

[2] J. G. P. W. Clevers and L. Kooistra, “Using Hyperspectral Remote Sensing Data for Retrieving Canopy Chlorophyll and Nitrogen Content,” IEEE J. Sel. Top. Appl. Earth Obs. Remote Sens., vol. 5, no. 2, pp. 574–583, Apr. 2012.

[3] M. Diacono, P. Rubino, and F. Montemurro, “Precision nitrogen management of wheat. A review,” Agron. Sustain. Dev., vol. 33, no. 1, pp. 219–241, Sep. 2012.

[4] D. J. Mulla, “Twenty five years of remote sensing in precision agriculture: Key advances and remaining knowledge gaps,” Biosyst. Eng., vol. 114, no. 4, pp. 358–371, Apr. 2013.

[5] L. Kooistra, J. Suomalainen, S. Iqbal, J. Franke, P. Wenting, and H. Bartholomeus, “Crop monitoring using a light-weight hyperspectral mapping system for unmanned aerial vehicles : first results for the 2013 season,” in Workshop on UAV-based Remote Sensing Methods for Monitoring Vegetation, 2013, no. September, pp. 1–7.

[6] C. Zhang and J. Kovacs, “The application of small unmanned aerial systems for precision agriculture: a review,” Precis. Agric., vol. 13, no. 6, pp. 693–712, Jul. 2012.

[7] F. Gao, J. Masek, M. Schwaller, and F. Hall, “On the blending of the Landsat and MODIS surface reflectance: predicting daily Landsat surface reflectance,” IEEE Trans. Geosci. Remote Sens., vol. 44, no. 8, pp. 2207–2218, Aug. 2006.

[8] R. Zurita-Milla, J. G. P. W. Clevers, and M. E. Schaepman, “Unmixing-Based Landsat TM and MERIS FR Data Fusion,” IEEE Geosci. Remote Sens. Lett., vol. 5, no. 3, pp. 453–457, 2008.

[9] C.-C. Liu, “Processing of FORMOSAT-2 Daily Revisit Imagery for Site Surveillance,” IEEE Trans. Geosci. Remote Sens., vol. 44, no. 11, pp. 3206–3214, Nov. 2006.

[10] C. M. Gevaert and F. J. García-Haro, “A Comparison of STARFM and an Unmixing-based Algorithm for Landsat and MODIS Data Fusion,” 2014.

[11] J. G. P. W. Clevers, “Application of a weighted infrared-red vegetation index for estimating leaf Area Index by Correcting for Soil Moisture,” Remote Sens. Environ., vol. 29, no. 1, pp. 25–37, Jul. 1989.